MULTISPECTRAL SUPERCONDUCTING QUANTUM DETECTORS

FINAL REPORT

PERIOD OF PERFORMANCE: SEP.-95 TO DEC.-98

CONTRACT No. F49620-95-C-0074

JANUARY 1999

AUTHORS

NATHAN BLUZER and MARTIN G. FORRESTER

PRESENTED TO
UNITED STATES AIR FORCE OFFICE OF SCIENTIFIC RESARCH
110 DUNCAN AVE. SUITE B115
BOLLING AFB, WASHINGTON DC 20332-0001

BY

NORTHROP GRUMMAN ELECTRONIC SENSORS AND SYSTEMS SECTOR
ADVANCED TECHNOLOGY CENTER
WINTERSON and NURSERY ROADS
LINTHICUM, MARYLAND 21090

AFRL-SR-BL-TR-99-

0103

REPORT DOCUMENTATION PAGE

1. AGENCY USE ONLY (Leave blank)	2. REPORT DATE	3. REPORT TYPE AND DATES COVERED
	March 24, 1999	Final Report September 1995-December 1998

4. TITLE AND SUBTITLE

Multispectral Superconducting Quantum Detectors

5. FUNDING NUMBERS

F49620-95-0074

6. AUTHOR(S)

Nathan Bluzer and Martin G. Forrester

7. PERFORMING ORGANIZATION NAME(S) AND ADDRESS(ES)

Northrop Grumman Electronic Sensors and System Sector
Advanced Technology Center
Winterson and Nursery Roads
Linthicum, Maryland 21090

8. PERFORMING ORGANIZATION REPORT NUMBER

9. SPONSORING / MONITORING AGENCY NAME(S) AND ADDRESS(ES)

United States Air Force Office of Scientific Research
110 Duncan Ave. Suite B115
Bolling Air Force Base
Washington, DD 20332-001

10. SPONSORING / MONITORING AGENCY REPORT NUMBER

11. SUPPLEMENTARY NOTES

12a. DISTRIBUTION / AVAILABILITY STATEMENT

12b. DISTRIBUTION CODE

13. ABSTRACT ***(Maximum 200 Words)***. Superconducting quantum detector structures were formulated, designed, fabricated and tested. As designed, the expected photoresponse depends on the superconducting current's kinetic inductance. The kinetic inductance, inversely proportional to the Cooper pair density, changes with photoabsorption. Photons with sufficient energy to breaks Cooper pairs, modulate the superconducting current's kinetic inductance. The modulation depends on the photoabsorbed photon flux density and the quasiparticle excitation lifetime. Such a photoresponse is consistent with a quantum detector. For maximum response, we have fabricated photodetector structures with significantly reduced geometrical inductance and maximum kinetic inductance. These quantum detectors were monolithic with Josephson-junction readout circuits. A multi-level $YBa_2Cu_3O_{7-\delta}$ processes was used for fabrication. These devices were tested at cryogenic temperatures in a specially designed and fabricated facility.

Electrically, the SQUID read out performed well. Modulation of the SQUID critical current was successful, revealing that we successfully fabricated these detector structures. This modulation was achieved by injecting a dc current into one half of the quantum photodetector, thereby changing the average phase across Josephson junctions from $\pi/2$. This phase change reduced the SQUID's critical current. The quasiparticle lifetime was too short to measure a quantum response at low frequencies. The experimentally observed short quasiparticle lifetime may be due to intrinsic or extrinsic effects. Given the relative immaturity of high temperature superconducting fabrication technology, it is not unreasonable to expect material defects to severely reduce the quasiparticle lifetime and hence mask any low frequency quantum responses. A second possibility, intrinsic in nature, is that unlike the BCS superconductors, the quasiparticle lifetimes in high temperature superconductors do not exponentially increase with lower temperatures.

14. SUBJECT TERMS

Superconducting, Quantum, Photodetectors, Kinetic Inductance

15. NUMBER OF PAGES

16. PRICE CODE

17. SECURITY CLASSIFICATION OF REPORT	18. SECURITY CLASSIFICATION OF THIS PAGE	19. SECURITY CLASSIFICATION OF ABSTRACT	20. LIMITATION OF ABSTRACT
Unclassified	Unclassified	Unclassified	

MULTISPECTRAL SUPERCONDUCTING QUANTUM PHOTODETECTORS

1.0 EXECUTIVE SUMMARY

Infrared sensors detect targets by their black body radiation. This feature makes IR sensors particularly useful for passively detecting targets, under ambient conditions, on earth, or in space, against a cold background. Ambient conditions include day time or night time. The 24 hours passive detection feature, based on IR radiation, has motivated DoD to sponsor development of MWIR and LWIR sensors. Theoretically, above 1K, quantum sensors provide superior performance over thermal sensors (bolometers). Accordingly, DoD sponsored development programs for quantum detectors, made from semiconductor materials, including, PV and PC HgCdTe, InSb, Extrinsic Silicon, Platinum Silicide, and III-V quantum well superlattice structures. The difficulty in achieving low cost semiconductor based quantum IR sensors fostered a multiplicity of detector approaches. Accordingly, with the discovery of high temperature superconductivity (HTS), programs were started to test the viability of the new HTS materials for making more sensitive MWIR and LWIR detectors. One of the driving forces for using HTS for IR detectors is a belief that the energy gap in HTS is smaller than the bandgap in semiconductor materials, and hence it is anticipated that HTS based photodetectors should provide a much longer cut-off wavelength.

This program's objective was to demonstrate high performance multispectral quantum detectors made in superconducting $YBa_2Cu_3O_{7-\delta}$. It was anticipated that the HTS based detectors will be sensitive between one and thirty μm. The operation of the HTS based quantum depends on photoinduced changes in the superconducting condensate's kinetic inductance.

This program's approach included four main tasks. First, a quantum detector structure was formulated in $YBa_2Cu_3O_{7-\delta}$ that was monolithic with a readout circuit. Second, the multispectral quantum detector was designed for maximum photoresponse by minimizing the geometrical inductance and maximizing the condensate's kinetic inductance. Third, a multi-level $YBa_2Cu_3O_{7-\delta}$ process was developed and used for

fabricating superconducting quantum detectors. And finally, using previously developed theoretical analysis, an experiment was formulated and test equipment were constructed to evaluate the performance of multispectral superconducting quantum detectors.

The anticipated payoffs from the multispectral superconducting quantum detector program were broader spectral response, and higher sensitivity. Such performance goals are desirable for facilitating DOD platforms with avionics that provide 24 hour all weather imaging performance and improved survivability. It is hoped that HTS based multispectral quantum sensors will provide superior target identification at longer ranges and with better resolution than conventional IR sensors.

Several things were accomplished on this program. Specifically, we formulated and designed a quantum detector structure with significantly reduced geometrical inductance and maximized kinetic inductance. This is necessary to maximize the quantum photoresponse. Secondly, we fabricated the formulated superconducting quantum detectors monolithic with Josephson-junction readout. The fabrication used a multi-level $YBa_2Cu_3O_{7-\delta}$ process. Finally, these devices were tested at cryogenic temperatures.

Electrically, the SQUID read out performed well. Modulation of the SQUID critical current was successful. This modulation was achieved by injecting a dc current into one half of the quantum photodetector, thereby changing the average phase across Josephson junctions from $\pi/2$. This phase change reduced the SQUID's critical current. Such a modulation of the SQUID's critical current demonstrates that the two level YBCO photodetector and read out structure were successfully fabricated: a superconducting path existed around the loop.

Optical response measurements, down to 10K, did not indicate a photoresponse. The devices were cooled to a very low reduced temperature to maximize the quasiparticle lifetime, as expected for a BCS superconductor. With maximum quasiparticle lifetime the photoresponse is maximized. The lack of a measured quantum photoresponse may be attributed to extrinsic and/or intrinsic effects.

From an extrinsic point of view, the YBCO material may have too many scattering defects, which reduce the quasiparticle lifetime. A reduced quasiparticle

lifetime severely reduces the photoresponse and makes it difficult to measure. With improved signal to noise ratio, achievable with a larger percentage SQUID critical current modulation, any quantum photoresponse should be more readily detected. For larger modulation, the geometrical inductance needs to be further reduced.

Finally, from the intrinsic point of view, the intrinsic nature of the energy gap in High Temperature Superconductors may not lead to exponential increases in the quasiparticle lifetime with reduced temperature. An exponential increase in quasiparticle lifetime with reduced temperature is expected for BCS superconductors, based on Cooper pairs with s-wave symmetry. Thus, the quasiparticle lifetime is only adequate to provide fast quantum detectors, operating at GHz rates. The present measurement set up was aimed at realizing quantum detectors operating at much slower frequency, compatible with television frame rates, 60 Hz.

2.0 MULTISPECTRAL SUPERCONDUCTING QUANTUM DETECTORS

This program was started with the goal of demonstrating multispectral quantum photodetectors with very long cut-off wavelength using the newly discovered HTS materials[1]. Given the relative immaturity of the HTS field, we formulate a very simple detector structure. The formulated multispectral quantum photodetector (up to 100x100μm) is based on the kinetic inductance of a superconductor and thus is named a Quantum Superconducting Kinetic Inductance Photodetector (QSKIP). The performance of this QSKIP is analyzed in section 2.2. The analysis reveals that the QSKIP photoresponse will be limited by the Cooper pair binding energy 2Δ, for YBCO it is believed to correspond to about 32μm. The geometry for maximizing the QSKIP's photoresponse is introduced in section 2.3. The QSKIP readout is a simple SQUID circuit. The QSKIP in intended to operate in the Meissner State and below 50% of I_C. This restriction will limit flux flow noise and the noise will be primarily due to fluctuations in the condensate population.

For a YBCO QSKIP, theoretical Noise Equivalent Power[2] calculation reveals a dependence on: quasiparticle generation, quasiparticle recombination, anharmonic

phonon decay, and phonon trapping lifetimes. The Noise Equivalent Power estimate for a YBCO QSKIP is about $2.5x10^{-15}$ Watts/$\sqrt{Hz}$ at 9K for a 10μsec quasiparticle lifetime. With longer quasiparticle lifetimes and/or lower noise SQUID readout circuits, the projected NEP should directly improve.

The QSKIP fabrication is described in section 4.0. The experimental approach and measurements on the QSKIP are presented in section 3.0. The results from these QSKIP measurements are given in section 5.0.

2.1 BACKGOUND AND THEORY OF OPERATION

The viability of superconductor materials for use in quantum detectors depends on the quasiparticle's photoexcitation lifetime. Different detector structures may be employed to manifest photoinduced changes, but their performance will ultimately be directly proportional to the quasiparticle photoexcitation lifetime: the longer the lifetime is the larger is the photoresponse. Such performance dependence is common to quantum detectors made in semiconductors or superconductors. However, the lifetime issue can be sometimes mitigated by using structures wherein the collection speed is fast relative to the photoexcitation lifetime: hence all photoexcited carriers are collected before they decay to thermal equilibrium. Never the less, photoexcitation lifetime remains important for maximizing detector performance.

Predicting the photogenerated quasiparticles' lifetime for HTS materials is difficult and subject to much uncertainty. First, the mechanism for HTS is not understood, hence making calculations uncertain. Second, beyond the theoretical difficulties, we expect the HTS material quality to impact the experimental quasiparticle lifetime, similar to semiconductors where the photoexcitation lifetimes depend on material quality. With these limitations in mind, we proceed to briefly look at the quasiparticle lifetime.

We[2] estimate the quasiparticle lifetime assuming a BCS[3] type superconductor, based on "s" wave pairing. This is appropriate for low temperature superconductors but is presently unresolved for high temperature materials where the nature of the

superconducting gap is still in question. Calculations using "d" and "s" wave pairing were made by Sergeev and Reizer[4] with results similar to these calculations. Since the QSKIP is intended to operate near thermal equilibrium, the thermal equilibrium quasiparticle lifetimes are appropriate. Operating significantly away from thermal equilibrium is expected to decrease the effective quasiparticle lifetime and the photoresponse, leading to a nonlinear and compressive photoresponse. With these two caveats, we proceed to estimate the quasiparticle lifetime using a BCS model.

The intrinsic quasiparticle lifetime at thermal equilibrium τ_R^{EQ} is very sensitive to temperature, and for a BCS superconductor at $T< 0.5T_C$ the intrinsic quasiparticle lifetime is given by Kaplan[5] as:

$$\tau_R^{EQ}(T)=\frac{\tau_0}{\sqrt{\pi}}\left[\frac{k_B T_C}{2\Delta_0}\right]^{5/2}\left[\frac{T_C}{T}\right]^{1/2}\exp\left[\frac{\Delta_0}{k_B T}\right] \qquad (2,1)$$

$$\approx 0.1\tau_0 \exp\left[\frac{\Delta_0}{k_B T}\right],$$

where, for low temperature superconductors, a representative value for τ_0 calculated by Kaplan[5] et. al is approximately 10^{-11} seconds. Near thermal equilibrium we *estimate* that $\tau_R^{EQ} \approx \tau_R$. At a low temperatures of $T\approx 0.1T_C$, for a BCS superconductor ($\Delta_0 \approx 1.72\ k_B T_C$), the computed intrinsic recombination lifetime (with Eq. (2,1)) is very large ($\tau_R \approx 30\mu$sec) and is much larger than τ_0. If high temperature superconductors have a larger "s" type energy gap, even longer quasiparticle lifetimes can be expected. For example, in YBCO the energy gap inferred from specific heat measurements[6] is $\Delta_o \approx 2.5 k_B T_C$ (instead of $\Delta_0 \approx 1.72\ k_B T_C$ for a BCS gap), so at $T\approx 0.1T_C$ the calculated intrinsic quasiparticle lifetime is even longer, or $\tau_R \approx$ 70msec.

In low temperature BCS type superconductors, experimental measurements confirm the exponential dependence of the quasiparticle lifetime, expressed by Equation (2,1), on the superconductor's energy gap and the operating temperature. Effective quasiparticle lifetime measurements in aluminum,[7,8,9] lead,[10,11] and tin[12] show an exponential dependence represented by Equation (2,1). At low temperatures very long

effective quasiparticle lifetimes are measured for aluminum[8] ($\approx$100μsec at $\Delta/kT > 6$) tin[13] ($\approx$0.1μsec at $\Delta/kT > 5$), and lead[14] ($\approx$10μsec at $\Delta/kT > 5$). Even longer effective quasiparticle lifetimes are expected in BCS superconductors at lower operating temperatures ($\Delta/kT > 10$ or $T/T_C < 0.172$) and because of phonon trapping, discussed next.

The effective quasiparticle lifetime depends on several components: the intrinsic quasiparticle lifetime, τ_R; the phonon escape lifetime into the substrate, τ_{ES}; the anharmonic phonon decay lifetime, τ_{AH}; and the pair breaking lifetime, τ_B. The increase in the effective quasiparticle lifetime is evident from the solution to the Rothwarf-Taylor Equations[15] where the combination of lifetimes τ_R, τ_B, τ_{ES}, and τ_{AH} results in an effective quasiparticle lifetime τ_{EFF} given by:

$$\frac{1}{\tau_{EFF}} = \frac{1}{\frac{\tau_R}{\tau_B}\tau_{ES}} + \frac{1}{\frac{\tau_R}{\tau_B}\tau_{AH}} \qquad \textbf{(2,2)}$$

The effective quasiparticle lifetime is limited by the depletion rate of nonequilibrium pair breaking phonons through: (1) escape into the substrate with an *effective* rate, $\tau_{EES}=(\tau_R/\tau_B)\tau_{ES}$ and (2) anharmonic phonon decay with *effective* rate, $\tau_{EAH} = (\tau_R/\tau_B)\tau_{AH}$ (provided $\tau_{AH} > \tau_B$). At lower temperatures and near thermal equilibrium, these effective rates are much slower since $(\tau_R/\tau_B) >> 1$.

The effective anharmonic decay τ_{EAH} and effective phonon escape τ_{EES} lifetimes are greater than the corresponding intrinsic values for τ_{AH} and τ_{ES}.[16,17,18] At low temperatures, τ_B is very small[5], $\leq 10^{-10}$ sec, and τ_R is much longer, $\approx 10^{-5}$ sec, (or $\tau_R/\tau_B \geq 10^5$) leading to a condition wherein the nonequilibrium photodeposited energy resides most of the time in the form of excited quasiparticles. However, any photodeposited energy escapes by one of two processes: (1) anharmonic decay or (2) escape into the substrate when it exists in the form of nonequilibrium phonons and not excited quasiparticles. Since the photodeposited energy exists for the largest fraction of time, $\tau_R/(\tau_R+\tau_B)$, in the form of excited quasiparticles, there is proportionally very little time during which the nonequilibrium pair breaking phonons can escape into the substrate or undergo anharmonic decay. Therefore at low temperatures, the effective lifetimes $\tau_{EAH} >> \tau_{AH}$ and $\tau_{EES} >> \tau_{ES}$ become much larger, leading to corresponding increases in τ_{EFF}. With a longer

τ_{EFF}, the QSKIP expected performance is significantly improved responsivity. The responsivity can be further increased with optimized detector geometry, and such approaches are considered next.

2.2 PHOTORESPONSE MAXIMIZATION

The QSKIP approach is based on the Cooper pairs' kinetic inductance and hence the label: Quantum Superconducting Kinetic Inductance Photodetector[19] (QSKIP). *This detector's photoresponse is sensitive to photoinduced changes in the total Cooper pair population.* The QSKIP was designed not to depend only on changes in the condensate population within a coherence distance ξ from the Josephson junction. The area efficiency of these Josephson junction, based on changes in normal gap current, is small and not practical for large arrays.

The QSKIP's intended operating conditions are: (1) low temperatures, (2) low background radiation, (3) below H_{C1} or in the Meissner state, (4) below 50% of the superconducting critical current I_C, (5) under static nonequilibrium conditions (achieved with constant photoillumination), and (6) not under pulsed laser radiation, as reported in many experiments[20,21,22]. These operating conditions are consistent with maximum effective quasiparticle lifetime, expected low temperature and near thermal equilibrium. The lowest detector noise is anticipated for operation below H_{C1} and at low temperatures ($T/T_C<0.1$), because noise from fluxons formations and movement is severely inhibited.

Two different QSKIP geometries were considered in this program: (1) a superconducting ring, read out by a SQUID, and (2) SQUID with a collapsed loop. Both devices are described in detail below. The choice of QSKIP geometry not only depends on anticipated performance but also on fabrication issues. These are considered in conjunction with each QSKIP device.

2.2.1 A superconducting ring photodetector

In the first QSKIP geometry selected, the photodetector is made from a simple superconducting film patterned into a closed loop with input and output current leads. To facilitate photoresponse calculation, the QSKIP is represented by a circular loop,[23,24] and is illustrated in Figure 2.1. For maximum coupling efficiency, the readout SQUID is

directly coupled[23] with the QSKIP, see Figure 2.2. In operation, the QSKIP is biased by a constant dc current I_0, $I_0 < 0.5\ I_C$. The QSKIP circuit divides I_0 into currents I_1 and I_2. With photoabsorption, the division of I_0 into I_1 and I_2 changes and this change represents the QSKIP response.

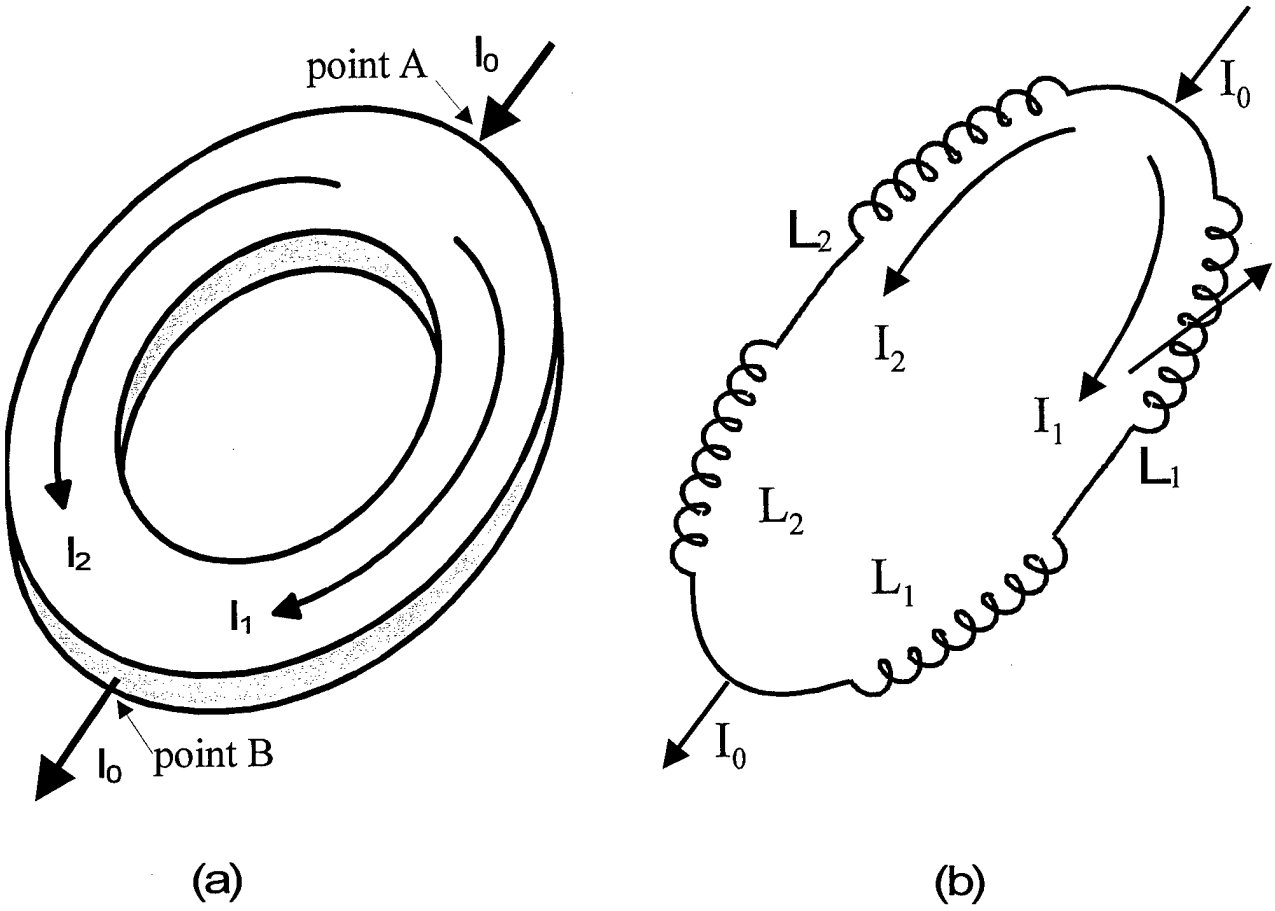

Figure 2.1. A superconducting loop (a), thinner than the London penetration depth, is subjected to a bias current I_0 injected at point "A" and removed at point "B". The bias current I_0 is divided into currents I_1 and I_2 flowing in branches 1 and 2, respectively. The equivalent circuit (b) contains the magnetic ($L_1 = L_{11} - M_{12}$, $L_2 = L_{22} - M_{12}$) and kinetic ($\mathcal{L}_1, \mathcal{L}_2$) inductance terms for branches 1 and 2, respectively. The self and mutual magnetic inductances are, respectively, represented by (L_{11}, L_{22}) and ($M_{12} = M_{21}$). $\mathcal{L}_1$ is represented as a variable inductor to indicate changes caused by photoabsorption in branch 1.

The current division in the QSKIP is calculated from the minimum of the superconductor energy functional — the Hamiltonian. The condensate's Hamiltonian is expressed in terms of the operating currents, I_1 and I_2, and the Cooper pair densities $_{CP}(X)$,

approximated to be constant and equal to $_{CP1}$ and $_{CP2}$ in branches 1 and 2, respectively. After incorporating the vector potential A(X) into the Hamiltonian, we calculate the energy extrema in terms of currents I_1 and I_2 and under thermal equilibrium or static nonequilibrium conditions (achieved with constant photoillumination). Photoabsorption of a constant photon flux in only one branch reduces the number of Cooper pairs in that branch from the thermal equilibrium level, and this represents a new static nonequilibrium state for the number of quasiparticles in that branch. With each new level of photoillumination, the current division changes in response to the new static nonequilibrium conditions (or number of quasiparticles in the illuminated branch). The QSKIP's performance is computed in terms of the changes in the quasiparticle density.

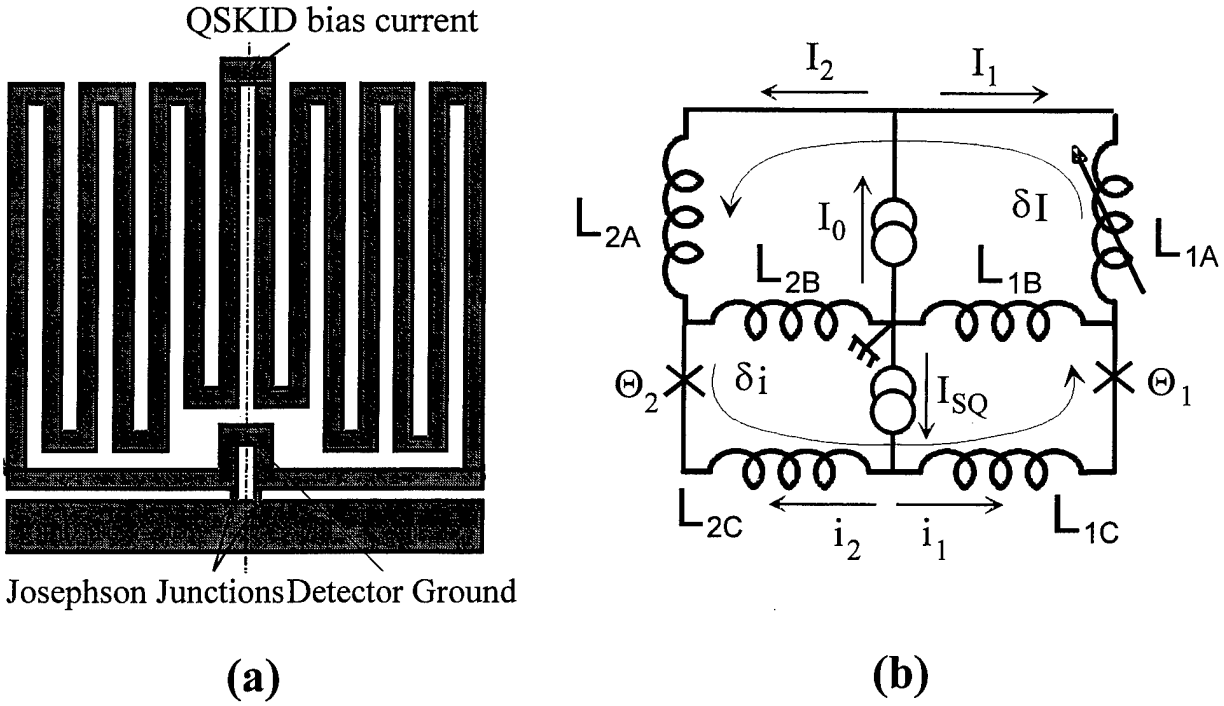

Figure 2.2. The YBCO QSKIP[23] (a) is shaped into a serpentine pattern to increase its kinetic inductance and improve isolation against quasiparticle diffusion between the two branches. The readout SQUID is directly coupled to the QSKIP at the bottom. The photon flux only illuminates the right half of the QSKIP. The equivalent circuit (b) for the symmetrical QSKIP and readout SQUID represents the kinetic and magnetic inductances for branches 1 and 2. The QSKIP is biased with a dc current I_o and the SQUID is biased with a dc current i_{SQ}.

The QSKIP ring's energy minimum is calculated in terms of the current flowing in the circuit shown in Fig. 2.1. A dc bias current I_0, injected at point A, is divided into currents I_1 and I_2, in branches one and two, respectively, and I_0 exits at point B. The total energy of the condensate, E_{QSKIP}, is computed by integrating the energy of each pair over the pair density $\rho_{CP}(X)$ and the QSKIP volume 2V. The value of currents I_1 and I_2 satisfy the energy extrema of the superconductor's Hamiltonian, $\mathcal{H}$, operating on the condensate, represented by a wave function Ψ. The Hamiltonian written in terms of canonical momentum[25] (the squared term in Equation (2,3), and the Cooper pair's interacting potential (last term) is:

$$\mathcal{H}=\frac{1}{2m_{CP}}\left[\mathbf{p}(X)+q_{CP}\mathbf{A}(X)\right]^2+q_{CP}\Phi(X)+q_{CP}V_{CP}(X) \qquad (2,3)$$

Where $p(X)=m_{CP}v$ is the kinetic momentum, A(X) is the vector potential generated by the current flow, $V_{CP}(X)$ is the attractive potential for a Cooper pair at X, $\Phi(X)$ is the electrostatic potential energy, q_{CP} is the electric charge for a pair and m_{CP} is the mass of a pair. We simplify equation 1 by making use of the Coulomb[26] gauge $\nabla\bullet A(X)=0$, and the so called London gauge[27] $\Lambda J(X)=-A(X)$, where $\Lambda=m_{CP}/[\rho_{CP}(X)q_{CP}^2]$ and J(X) is the current density in the superconductor.

The Hamiltonian in Eq. (2,3) is simplified to a form similar to the BCS Hamiltonian[3,28] i.e.,

$$\mathcal{H}=\frac{1}{2m_{CP}}\left[\mathbf{p}(X)\right]^2+\frac{1}{2\rho_{CP}(X)}\mathbf{A}(X)\cdot\mathbf{J}(X)+q_{CP}\Phi(X)+q_{CP}V_{CP}(X) \qquad (2,4)$$

We have used the expression $J(X)=q_{CP}\rho_{CP}(X)p(X)/m_{CP}$ to simplify equation 1 and obtain an expression for the Hamiltonian with two terms in addition to the BCS terms: the second term accounts for the energy present in a flowing superconducting current, while the last term with $\Phi(X)$ was eliminated by BCS[3] by solving the problem relative to the Fermi Energy, E_F. Unlike the first two terms, the last two terms in Eq. (2,4) are not a function of currents I_1 or I_2 and they will drop out when the energy minimum of the QSKIP is calculated relative to I_1 and I_2.

The QSKIP energy, E_{QSKIP}, is obtained by integrating $\mathcal{H}$ over the Cooper pair density $\rho_{CP}(X)=\Psi^*\Psi$ where this density spans the domain of the Hermitian operator $\mathcal{H}$. Incorporating $\rho_{CP}(X)=\Psi^*\Psi$ and substituting $J(X)=q_{CP}\rho_{CP}(X)p(X)/m_{CP}$, into the Hamiltonian given by Eq. 2, the expression for the QSKIP energy E_{QSKIP} becomes:

$$E_{QSKID}=\int_{2V}\Psi^*\mathcal{H}\Psi d^3x=\frac{1}{2}\int_{2V}\Lambda\mathbf{J}(X)\cdot\mathbf{J}(X)d^3x+\frac{1}{2}\int_{2V}\mathbf{A}(X)\cdot\mathbf{J}(X)d^3x+ \int_{2V}\rho_{CP}(X)\left[\Phi(X)+V_{CP}(X)\right]d^3x \tag{2,5}$$

The energy in Equation (2,5) has three terms: (1) the first term represents the condensate's kinetic energy, (2) the second term represents the energy stored in the field[29] produced by a flowing supercurrent, and (3) the third term represents the potential energy terms.

Since the E_{QSKIP} energy minimum is calculated in terms of currents I_1 and I_2 [or the corresponding current densities $J_1(X)$ and $J_2(X)$] we need to express Equation (2,5) in terms of these. This is obtained after integrating over the volumes of branches 1 and 2. The first and last terms in Equation (2,5) will each yield an additional term while the middle term will yield three additional terms. The vector potential term expressed in terms of volume integral over branches 1 and 2 is:

$$\mathbf{A}(X)=\left(\frac{\mu_0}{4\pi}\right)\int_{V1}\frac{\mathbf{J}_1(Y)}{|\mathbf{X}-\mathbf{Y}|}d^3y+\left(\frac{\mu_0}{4\pi}\right)\int_{V2}\frac{\mathbf{J}_2(Y)}{|\mathbf{X}-\mathbf{Y}|}d^3y \tag{2,6}$$

Incorporating these substitutions into Equation (2,5), we obtain an equation for the QSKIP energy in terms of I_1 and I_2 and: the kinetic inductances (λ_i), the self magnetic inductances (L_{ij}), and the mutual magnetic inductances (M_{ij} for $i\neq j$), where the subscripts "i" and "j" refer to branches one or two, i.e.,

$$E_{QSKID}=\frac{1}{2}\lambda_1 I_1^2+\frac{1}{2}\lambda_2 I_1^2+\frac{1}{2}L_{11}I_1^2+\frac{1}{2}L_{22}I_2^2+M_{12}I_1I_2 + \int_{2V}\rho_{CP}(X)\left[\Phi(X)+V_{CP}(X)\right]d^3x \tag{2,7}$$

Where $\lambda_1 = (m_{CP}/q^2_{CP})(l_1/(S_1\rho_{CP1}))$ $[\lambda_2=(m_{CP}/q^2_{CP})(l_2/S_2\rho_{CP2}))]$ is the kinetic inductance of branch number one (two) with a Cooper pair density ρ_{CP1} $[\rho_{CP2}]$, a cross sectional area S_1 (S_2) and a length l_1 (l_2). The self inductance of branch one (two) is labeled by L_{11} (L_{22}) and the mutual inductance between the branches is labeled as $M_{12}= M_{21}$, by symmetry.

The minimum of E_{QSKIP} is calculated by taking the differential of equation (2,7) with respect to I_1 and I_2 to yield,

$$\frac{\partial E_{QSKID}}{\partial I_i}=[L_1+\lambda_1]I_1-[L_2+\lambda_2]I_2=0 \qquad (2,8)$$

We make use of the fact that the currents flowing in the QSKIP branches divide $I_0=I_1+I_2$ hence $\partial/\partial I_1=(\partial I_2/\partial I_1)(1/\partial I_2)= -\partial/\partial I_2$ and the magnetic inductance terms are combined into effective inductance terms: $L_1=L_{11}-M_{12}$ and $L_2=L_{22}-M_{12}$. It should be noted that for a symmetrical QSKIP $L_{11}=L_{22}$ and $M_{21}=M_{12}$. Equation (2,8) holds for any arbitrary value of Cooper pair density occurring for each level of constant photodepairing.

The photoresponse of the superconducting ring geometry is calculated in terms of the change in kinetic inductance $\Delta\lambda_1$, which is a function of the quasiparticle density ΔN_Q, and this depends on the effective quasiparticle lifetime. The photoresponse signal, $I_S=I_1-I_2$, is produced as the division of I_0 changes from $I_1 = I_2$ to $I_1 \neq I_2$ as one of the QSKIP branches is exposed to a constant level of illumination, and the currents change to satisfy the required *minimum energy* conditions. Without loss of generality, and for the sake of simplicity, we assume a totally symmetric QSKIP geometry, where, under no illumination and under thermal equilibrium, the Cooper pair density $\rho_{CP}(X)$ is the same in branches 1 and 2 producing a symmetric current division i.e. $I_1=I_2=I_0/2$. Hence, the thermal equilibrium signal current I_S^0, and the associated magnetic flux Φ_B^0 inside the ring are zero. Photoabsorption in branch number 1 only breaks the QSKIP's symmetry in $\rho_{CP}(X)$ and produces a photosignal $I_S= I_1-I_2$ and a corresponding net magnetic flux Φ_B inside the QSKIP's ring, where $\Phi_B= I_S(L_1+L_2)$. Read-out of the photoinduced signal current I_S (for directly coupled) or Φ_B (for magnetically coupled) is by a SQUID.

The signal current I_S is produced by kinetic inductance changes $\Delta\lambda_1$ caused by photoabsorption, in branch 1 only, of N_Φ photons with an average value of N_Φ^0. The signal current consists of a circulating current I_S, causing a corresponding magnetic flux Φ_B. The signal photocurrent directly depends on $\Delta\lambda_1$ and is computed by taking the differential of Equation (2,8) to obtain:

$$I_S = \frac{\partial I_1}{\partial L_1}\Delta\lambda_1 = \frac{-I_1}{[\lambda_1 + \lambda_2 + L_2 + L_2]}\Delta\lambda_1 \qquad (2,9)$$

Equation (2,9) is valid under static nonequilibrium conditions and when the quasiparticle density N_Q is much less than $\rho_{CP}(X)$. Using partial derivatives, the change in the kinetic inductance $\Delta\lambda_1$ is expressed as:

$$\Delta\lambda_1 = \frac{\partial L_1}{\partial \rho_{CP}(X)} \frac{\partial \rho_{CP}(X)}{\partial N_Q}\Delta N_Q \qquad (2,10)$$

Explicit expressions for the partial derivative factors in Equation (2,10) are obtained using Equation (2,8), the definition of kinetic inductance given below Equation (2,7), and the fact that each Cooper pair forms two quasiparticles ($\partial\rho_{CP}(X)/\partial N_Q = -1/2$). To complete the calculation for I_S, an explicit expression for ΔN_Q is needed that represents the photoinduced increase in the quasiparticle population in branch 1.

The total static nonequilibrium quasiparticle density N_Q is expressed as a sum of the thermal equilibrium quasiparticle density N_Q^{EQ} and the photoinduced increase in the quasiparticle density, $N_Q = \Delta N_Q + N_Q^{EQ}$. The thermal equilibrium quasiparticle density in each branch, based on a BCS superconductor at $T < 0.5\ T_C$, is given by:[14]

$$N_Q^{EQ} = 2N(0)\sqrt{\frac{\pi}{2}\Delta(T)\,k_B\,T}\exp\left(-\frac{\Delta(T)}{k_B\,T}\right) \qquad (2,11)$$

where N(0) is the density of states in volume and energy at the Fermi surface, k_B is Boltzmann's constant, T is the operating temperature in degrees Kelvin, and $\Delta(T)$ is the temperature dependent superconducting energy gap. An expression for the change in the

quasiparticle density ΔN_Q from the thermal equilibrium value N_Q^{EQ} is obtained with a *modified* form of the Rothwarf-Taylor[15] equations.

It should be noted that from equation (2,9) it is evident that the best photoresponse occurs when the geometrical inductance is minimized relative to the kinetic inductance. Such conditions require folding the ring onto itself, to minimize the magnetic flux inside. However, the fabrication of such a ring would require triple lever YBCO. This is very difficult to achieve, and instead we decided to change the design to a large SQUID with minimum geometrical inductance. The minimum geometrical inductance is achieved by collapsing the loop area to minimize magnetic flux. Such a detector is described below.

2,2,2 Large SQUID geometry photodetector.

The QSKIP's photoresponse is based on changes in the superconductor's kinetic inductance, caused by photodepairing of Cooper pairs. The kinetic inductance λ_{KI} of the condensate inside a superconductor, with a thickness $\mathbf{t_S}$, width $\mathbf{W_D}$, and length $\mathbf{L_D}$, is given as:

$$\lambda_{KI} = \frac{m^*}{n_S e^{*2}} \frac{L_D}{t_S W_D} \tag{2,12}$$

Where $\mathbf{m^*}$, $\mathbf{n_S}$ and $\mathbf{e^*}$ are the mass, density, and charge, respectively, of a Cooper pairs. We have neglected contributions from quasiparticles to the total kinetic inductance because the QSKIP is intended to operate at the low frequencies where scattering erases quasiparticle contributions.

The kinetic inductance is inversely dependent on the Cooper pair volume density $\mathbf{n_S}$ and this is modulated by the absorbed photons, providing they have sufficient energy to break Cooper pairs. A photon flux density φ, incident on a QSKIP detector, and absorbed along the thickness $\mathbf{t_S}$, changes the Cooper pair population density by:

$$\delta n_S = \frac{\varphi \tau_{QP}}{t_S} \tag{2,13}$$

Where, τ_{QP} is the photogenerated quasiparticles' lifetime. In response to the photogenerated changes in the condensate density δn_S, the kinetic inductance changes by:

$$\delta\lambda_{KI} = -\lambda_{KI}\frac{\delta n_S}{n_S} \tag{2,14}$$

The change in kinetic inductance is inversely proportional to the Cooper pair density and directly proportional to the quasiparticle lifetime. Thus, for a given photon flux, the maximum change in the kinetic inductance is realized with a small Cooper pair density, $\mathbf{n_S}$, and a long quasiparticle lifetime. Changes in the kinetic inductance are detected by monitoring changes in the superconducting condensate's phase $\theta(\mathbf{r})$, and this approach is described next.

The superconducting condensate is represented by a wave function $\Psi(\mathbf{r})$ which is given in terms of the Cooper pair density $\mathbf{n_S}$ and the condensate phase $\theta(\mathbf{r})$ as:

$$\Psi(r) = \sqrt{n_S}\exp[i\theta(r)] \tag{2,15}$$

For a constant value of n_S, the condensate momentum is computed by evaluating the expected value of the momentum operator $-i\hbar\nabla$, operating on the wave function $\Psi(\mathbf{r})$; and setting it equal to the conjugate momentum, we obtain:

$$\overline{\nabla}\theta(r) = \frac{2\pi}{\Phi_O}\left[\frac{\lambda_{KI}\underline{I_S}}{L_D} + \underline{A}\right] \tag{2,16}$$

Where $\Phi_O = \mathbf{h/e^*}$, the condensate current is $\underline{\mathbf{I_S}} = \mathbf{ae^*n_S}v_S$ (where $\mathbf{v_s}$ is the condensate's velocity), and $\underline{\mathbf{A}}$ is the vector potential.

The QSKIP photoresponse is based on the change in phase θ, given by Equation (2,16). The superconducting condensate's wave function, $\Psi(\mathbf{r})$, phase, θ, changes with: kinetic inductance λ_{KI}, the current $\underline{I_S}$, and the vector potential, $\underline{\mathbf{A}}$. For any given length of superconductor, if we make $\mathbf{I_S}$ constant, then the $\nabla\theta(\mathbf{r})$ will depend only on $\lambda_{\underline{KI}}$ and $\underline{\mathbf{A}}$. Exposing the superconducting element to a photon flux density φ, changes $\mathbf{n_S}$ and this manifests itself as a change in $\lambda_{\underline{KI}}$. The value of the vector potential $\underline{\mathbf{A}}$ remains constant with photoabsorption since $\mathbf{I_S}$ is held constant. As $\lambda_{\underline{KI}}$ changes the value of $\nabla\theta(\mathbf{r})$ changes

and this constitutes the QSKIP photoresponse. Measuring the photoinduced changes in $\nabla\theta(\mathbf{r})$ is facilitated if the contributions from the vector potential $\underline{\mathbf{A}}$ are small relative to the kinetic inductance term $\lambda_{\underline{KI}}$. Means for satisfying this requirement are revealed by integrating the wave function $\Psi(r)$ around a closed loop.

To satisfy the requirements that the wave function $\Psi(\mathbf{r})$ is single valued, the integral over a closed path demands that the phase shift is an integer multiply of 2π, and this is given in terms of the loops magnetic inductance ℓ_{MG}, kinetic inductance λ_{KI}, the superconducting current $\mathbf{I_S}$, and $\Phi_O=\mathbf{h/e^*}$ as:

$$\oint \overline{\nabla}\theta(r)\cdot\overline{d\ell} = 2\pi N = \frac{2\pi}{\Phi_O}\left[\lambda_{KI} + \ell_{MG}\right]I_S \qquad (2,17)$$

This equation represents flux quantization and corresponds to the Bohr-Sommerfeld quantization of conjugate angular momentum.

Since photoabsorption changes the condensate phase $\delta\theta(\mathbf{r})$, the QSKIP responsivity is calculated from Equation (2,17) in terms of the fractional phase change produced by photoabsorption. The fractional change in phase $\delta\theta/\theta$ is related to changes in the kinetic inductance, induced by photoabsorption, and is given by:

$$\frac{\delta\theta}{\theta} = \frac{-\lambda_{KI}}{\ell_{MG}+\lambda_{KI}}\frac{\varphi\tau_{QP}}{n_S t_S} \qquad (2,18)$$

It is evident that the maximum photoresponse is obtained when the fractional change in the condensate phase is maximum, and this requires making λ_{KI} **as** large as possible relative to ℓ_{MG}. Since ℓ_{MG} is the magnetic inductance, this requirement is equivalent to minimizing the value $\underline{\mathbf{A}}$ in Equation (2,16). Additionally, examining Equation (2,18), the thickness $\mathbf{t_S}$ should be minimized and the quasiparticle lifetime τ_{QP} should be maximized. The QSKIP geometry suitable for making the value of λ_{KI} larger than ℓ_{MG} is considered next.

The folded closed loop shown in Figure 2.3 is configured to minimize the magnetic inductance ℓ_{MG} and maximize the kinetic inductance $\lambda_{\underline{KI}}$. The geometry selected minimizes the magnetic flux passing through the loop accomplished with the folded geometry. Folding the loop decreases the magnetic inductance without effecting the

kinetic inductance value. This effect is evident from the expressions for the magnetic inductance of a folded loop, calculated below.

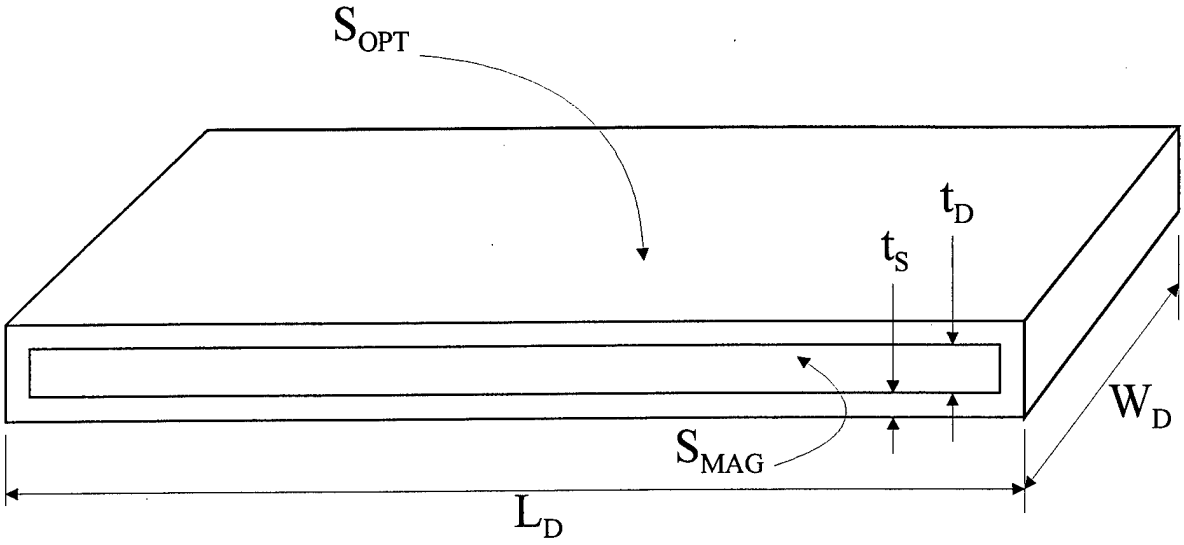

Figure 2.3. A loop, consisting of a superconducting material with a thickness $\mathbf{t_S}$, is folded to minimize the magnetic flux passing through the area enclosed by the loop, $\mathbf{S_{MAG}}$, in response to a current $\mathbf{I_S}$ flowing inside the loop. The superconducting loop is folded against an insulator with a thickness $\mathbf{t_D}$. Photons are incident onto the top layer with an optical area $\mathbf{S_{OPT}}$, corresponding to length $\mathbf{L_D}$ and width $\mathbf{W_D}$.

The reduction in ℓ_{MG} achieved through the folded geometry is evident by comparing the expressions for the magnetic inductance with and without the folded geometry. For an isolated strip, without a folded geometry, with length $\mathbf{L_D}$, width $\mathbf{W_D}$, and thickness $\mathbf{t_S}$, the magnetic field inductance is:

$$\ell_{MGI} = 0.2\,L_D\left[\mathrm{Ln}\left(\frac{2L_D}{W_D}\right) - \frac{t_S}{W_D} + 0.5\right] \quad \mu H \tag{2,19}$$

with all the variables in SI units. The corresponding magnetic field inductance for the folded loop geometry, shown in Figure 2.3, is given by:

$$\ell_{MG} = 0.4\,\pi\left[\frac{L_D}{W_D}\left(t_S + t_D\right)\right] \quad \mu H \tag{2,20}$$

Where t_D is the dielectric thickness, illustrated in Figure 2.3, and all the variables are in meters.

The reduction in the magnetic inductance with folding is evident from the ratio of Equation (2,20) divided by Equation (2,19), specifically:

$$\frac{\ell_{MG}}{\ell_{MGI}} = \frac{\frac{\pi(t_S + t_D)}{2L_D}}{\frac{W_D}{2L_D}\mathrm{Ln}\left(\frac{2L_D}{W_D}\right) - \frac{t_D}{2L_D} + \frac{W_D}{4L_D}} \qquad (2,21)$$

Typically, $\mathbf{t_D} << \mathbf{L_D}$ and $\mathbf{W_D} << \mathbf{L_D}$, leading to a condition where out of the three terms in the denominator the leading term dominates.

The reduction in ℓ_{MGI} can be readily estimated by substituting typical values into Equation (2,21): for example, let $\mathbf{L_D}$=300μm, $\mathbf{W_D}$=6μm, $\mathbf{t_D}$=0.2μm, and $\mathbf{t_S}$=0.1μm, than the ration given by Equation (2,21) becomes 0.03386. This represents about a thirty fold reduction in the magnetic inductance. For these values, the calculated inductance ℓ_{MG}, per Equation (2,20), is 18.85pH. The kinetic inductance $\mathbf{L_{KI}}$ value, given by Equation (2,12), is not reduced by the folded geometry shown in Figure 2.3. Substituting the previously mentioned values and $\mathbf{n_S} \approx 10^{27}$ pairs/m^3, we obtain $\lambda_{KI} \approx$19pH. With the folded loop geometry, the value of ℓ_{MG} is reduced thirty fold thereby making the value of λ_{KI} about equal to ℓ_{MG}.

Examining Equations (2,12) and (2,20), it becomes evident what is needed for maximizing the ratio λ_{KI}/ℓ_{MG}. An expression for the ratio λ_{KI}/ℓ_{MG}, obtained by combining Equations (2,12) and (2,20), becomes:

$$\frac{\lambda_{KI}}{\ell_{MG}} = \frac{2.5\mathrm{x}10^6}{\pi}\frac{m^*}{n_S e^{*2}}\frac{1}{t_S(t_S + t_D)} \qquad (2,22)$$

Maximum photoresponse requires maximization of this ratio λ_{KI}/ℓ_{MG} which is achieved by minimizing $\mathbf{t_S}$ and $\mathbf{t_D}$, with reductions in $\mathbf{t_S}$ producing the larger impact. The optimized values for $\mathbf{L_D}$ and $\mathbf{W_D}$ are not dictated by Equation (2,22) and hence can be selected to satisfy other criteria. It is advantageous to maximize $\mathbf{L_D}$ since this minimizes the inter-diffusion of quasiparticles between the illuminated and non-illuminated portions of the QSKIP, thereby maximizing the phase change. These design criteria have been

incorporated into a QSKIP with simple fabrication characteristics, as the added requirement.

2.3 PHOTODETECTOR GEOMETRY AND READOUT

Incorporating the maximum photoresponse requirements into a simple geometry results in a QSKIP amenable to fabrication. Consider the QSKIP shown in Figure 2.4, which consists of biasing circuits attached to a large, folded-geometry SQUID loop (acting as the readout circuit) with a photodetector incorporated within. Since the SQUID utilizes a folded loop geometry, it has low inductance and facilitates readout; provided that $\mathbf{I_C L_{TOT}} < \Phi_O$, where $\mathbf{I_C}$ is the SQUID critical current and $\mathbf{L_{TOT}} = \ell_{MG} + \lambda_{KI}$. With this low total inductance per unit length, the size of each SQUID can be made comparable to an IR detector, about 40 to 100μm square. Taking a single linear SQUID, shown in Figure 2.4, and shaping it into a serpentine path a square detector area, about 40 to 100μm on edge, can be filled. With this geometry only two Josephson Junctions are required per each detector, thereby facilitating the achievement of higher yield when building large arrays.

The folded loop geometry requires conventional fabrication technology similar to that required to fabricate SQUIDs with edge SNS or SS'S Josephson Junctions. This represents a reasonable technology for high temperature superconductors. Dual layer YBCO structures with an insulator, e.g. $SrTiO_3$, in between have been fabricated. Also, edge SS'S Josephson Junctions using 7% Cobalt doped YBCO, as the S' layer, have been made and exhibit good electrical characteristics. Similarly, PrBCO has been used for making SNS Josephson Junctions with good electrical characteristics. Thus, from a fabrication point of view, this QSKIP geometry shown in Figure 2.4 is attractive. Next, we proceed to examine the photoresponse obtained with this QSKIP geometry, with it's equivalent circuit shown in Figure 2.5.

The currents circulating in the QSKIP equivalent circuit, shown in Figure 2.5, pass through two Josephson junctions and several elements represented by inductors. Each Josephson junction is labeled by the average phase change, Φ_1 and Φ_2, the wave function $\Psi(\mathbf{r})$ undergoes across junctions 1 and 2 respectively. The inductors include the

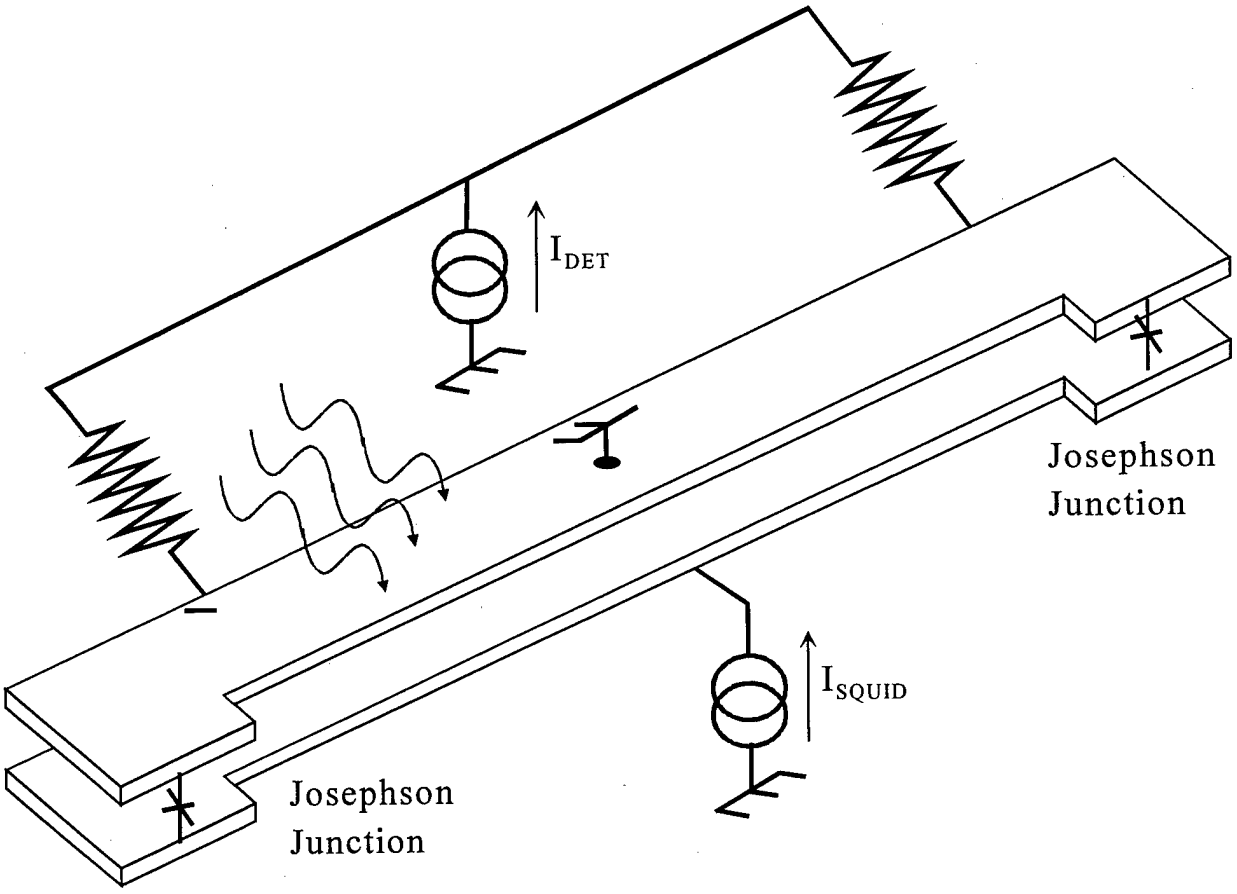

Figure 2.4. Folded geometry loop forms a SQUID, which acts as the readout circuit, and incorporates the SQKIP detector in the top half of the folded loop. Also shown are the sensor's biasing circuits. The SQUID reads the imbalance produced by the photoinduced phase change in the illuminated segment, on the left side. The right side is shielded with a metal light shield.

kinetic and magnetic inductances, for example, $\mathbf{L}_{LM}=\lambda_{LM}+\ell_{LM}$, where λ_{LM} represents the kinetic inductance portion and ℓ_{LM} represents the magnetic inductance portion of $\mathbf{L}_{LM}$. Using this notation, we proceed to derive the QSKIP photoresponse by satisfying several boundary conditions. In particular, the condensate's phase changes by $\mathbf{2N\pi}$ as we integrate the condensate's wave function $\Psi(\mathbf{r})$ around the SQUID, see Equation (2,17). Integrating Equation (2,17) around the closed loop and performing some simplifications, we obtain the equilibrium conditions for the QSKIP shown in Figure 2.5, and these are:

$$\Phi_2 = \Phi_1 + 2N\pi + \frac{2\pi}{\Phi_0}\left[I_2 L_{TR} - I_1 L_{TL} + (I_2 + I_{D2}) L_{RM} - (I_1 + I_{D1}) L_{LM} + I_2 L_{BR} - I_1 L_{BL} - \Phi_{EXT} \right] \quad (2,23)$$

where Φ_{ETX} represents contributions from external magnetic flux, and all the other variables are shown in Figure 2.5. The direction of the current in the QSKIP has been arranged to minimize the total change in the condensate's phase, and this is evident from the value of the terms in the square bracket in Equation (2,23). For Φ_{ETX}=0, it is evident that the terms in the square bracket occur in pairs which approximately cancel each other to minimize the total change, around the loop, in the condensate's phase. It should be noted that the total magnetic The SQUID's equilibrium bias current $\mathbf{I_{SQ}}$ is the sum of $\mathbf{I_1}$ and $\mathbf{I_2}$ and is expressed as:

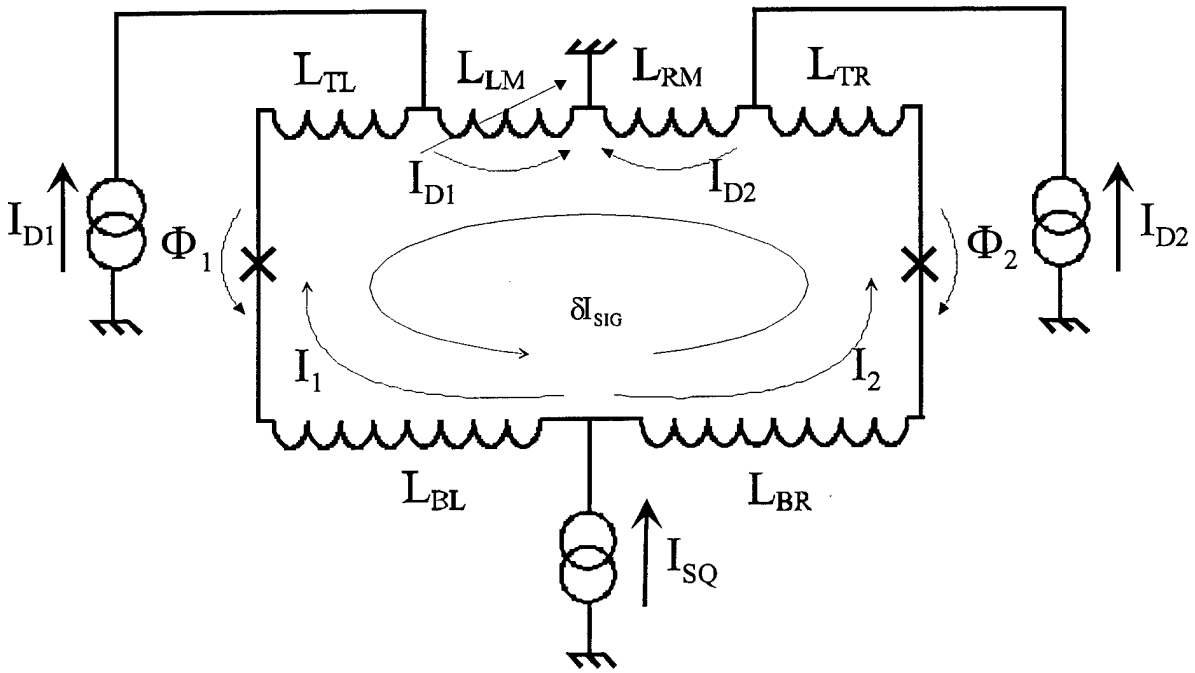

Figure 2.5. The equivalent circuit of the QSKIP structure shown in Figure 2.4. Six inductors represent the folded SQUID geometry, where each inductor includes the kinetic and magnetic inductance. The SQUID is biased with current $\mathbf{I_{SQ}}$, and the detector with currents $\mathbf{I_D}$ which are shunted to ground. Only inductor $\mathbf{L_{LM}}$ is exposed to photons and is represented by a variable inductance symbol. The photoinduced signal current is represented by $\delta\mathbf{I_{SIG}}$.

$$I_1 + I_2 = 0.5\, I_{SQ}\left[\sin(\Phi_1) + \sin(\Phi_2)\right] \tag{2,24}$$

We have assumed the critical currents of the two junction are identical. Since the SQUID is operated at maximum bias current, on average, the value of Φ_1 and Φ_2 are $\pi/2$.

The QSKIP photoresponse is calculated by taking the differential of Equation (2,23). In so doing we recognize that: $\delta\mathbf{I}_{D1} = \delta\mathbf{I}_{D2} = \delta\mathbf{L}_{RM} = \delta\mathbf{L}_T = \delta\mathbf{L}_B$, and that $\delta\mathbf{L}_{LM} = \delta\lambda_{LM}$, since photoabsorption will only change the kinetic portion of the kinetic inductance and not the magnetic inductance. The differential is simplified by taking the average value and thereby obtaining $\langle\delta\Phi_1\rangle = \langle\delta\Phi_2\rangle$, since on average $\Phi_1 = \Phi_2 = \pi/2$. We thus obtain:

$$\frac{\delta I_{SIG}}{I_1} = \left[1 + \frac{I_{D1}}{I_1}\right]\left[\frac{\delta\lambda_{LM}}{L_T + L_B + L_{RM} + L_{LM}}\right] \tag{2,25}$$

where the value of $\delta\lambda_{LM}$ is given by Equations (2,13) and (2,14). It is evident that the photoresponsivity, represented by the first term in the brackets in Equation (2,25), has a gain term consisting of the current ratio $\mathbf{I}_{D1}/\mathbf{I}_1$. Large gain is achieved by making the detector bias current at least 100 times larger that the SQUID bias current. The designed SQUID bias current is $\mathbf{I}_1 \approx 10\mu A$ and the maximum (equipment limited) detector bias current $\mathbf{I}_{D1} \approx 15mA$; offering a maximum possible gain ≈ 1500. Such large gain maximizes the photoresponse and offers the potential of improved signal to noise ratio by easing the requirements on the SQUID's read out electronics. This gain feature has been built into the mask with the QSKIP devices, detailed next.

The device mask embodies the QSKIP geometry illustrated in Figures 2.4 and 2.5. Since detectors are approximately square, the QSKIP, with a folded geometry loop, is shaped into a serpentine pattern to achieve approximately a square aspect ratio. The serpentine shaping maintains all the advantages of the folded loop geometry. A drawing of the two layer, serpentine patterned, folded QSKIP is shown in Figure 2.6 and a microphotograph of a fabricated device is shown in Figure 2.7.

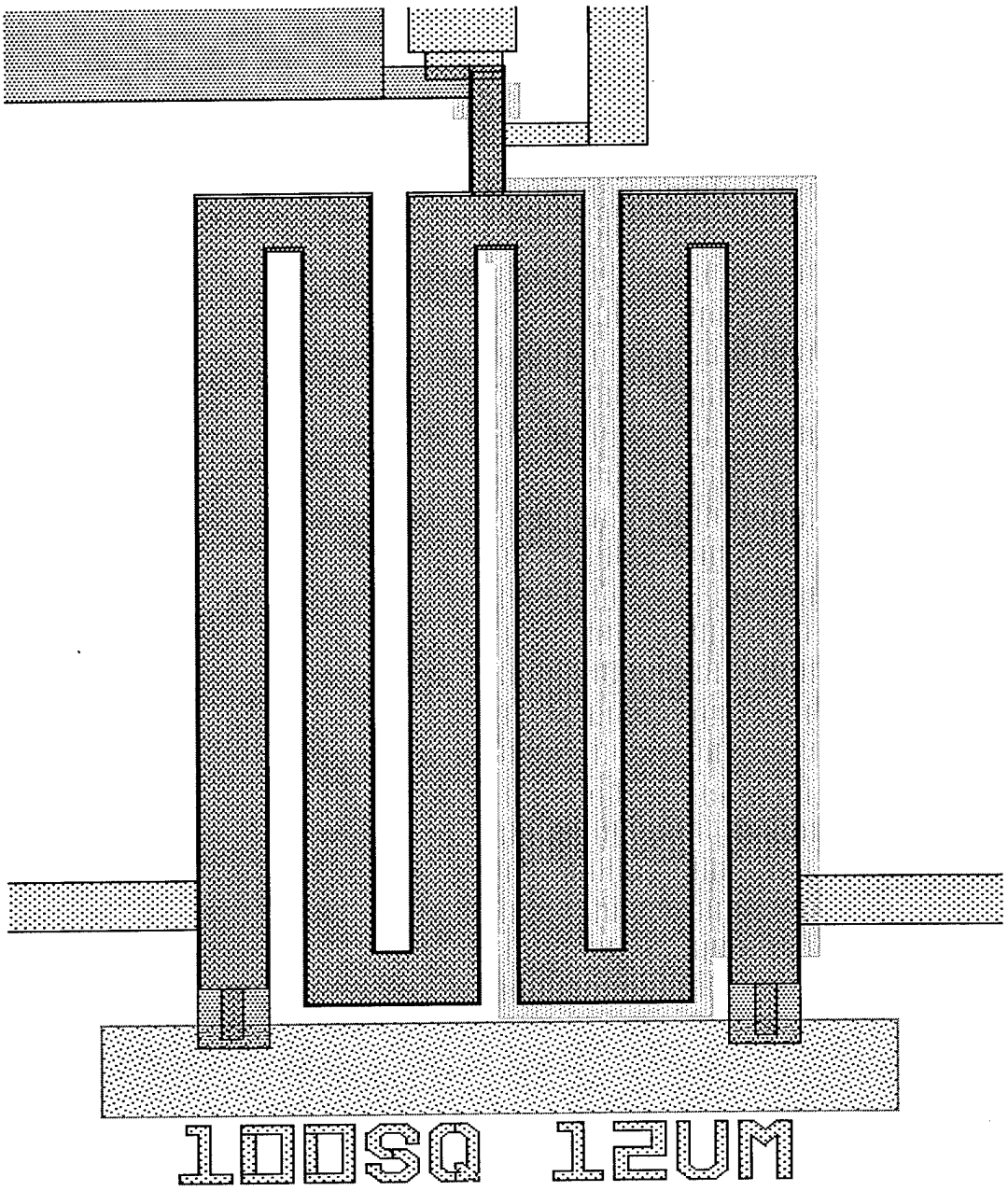

Figure 2.6. Schematic drawing of a folded serpentine patterned QSKIP with 100 squares length and 12μm width YBCO. The Josephson junctions are located at the bottom left and right corners.

The biasing of the QSKIP is as indicated in the circuit diagram shown in Figure 2.5. The ground connection (located on the bottom layer) and the SQUID current bias input $\mathbf{I}_{SQ}$ (located on the top layer) are attached at the top of Figure 2.6. Two detector bias currents ($\mathbf{I}_1$ and $\mathbf{I}_2$), as illustrated in Figure 2.5, are injected with the metal line tabs

extending from the left and right side, near the bottom. The QSKIP geometry is symmetric about the y-axis, and a light shield, made from gold, covers the left side of the QSKIP. Thus, photons incident on the QSKIP will produce depairing only on the left side. With photoabsorbtion, the kinetic inductance will change only on the left side and produce the photocurrent signal $\delta \mathbf{I}_{SIG}$, schematically illustrated in Figure 2.5.

A photomicrograph of a QSKIP device, fabricated with the mask of Figure 2.6, is shown in Figure 2.7. The electrical contacts/inputs are two on top (ground and SQUID bias current $\mathbf{I}_{SQ}$) and two near the bottom left ($\mathbf{I}_{D1}$ current) and right sides ($\mathbf{I}_{D2}$ current). The electrical contacts/inputs to the QSKIP device are fanned out into current and voltage leads to facilitate removal of contact and IR voltage potentials.

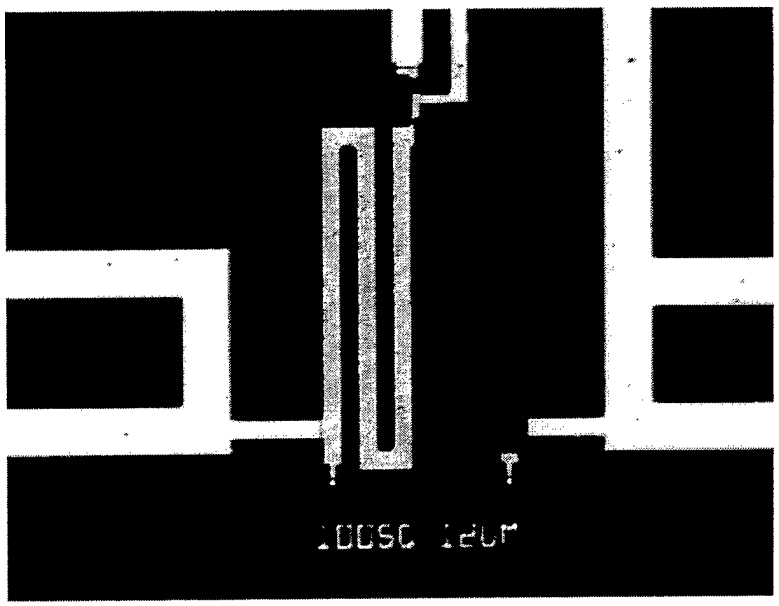

Figure 2.7. Photomicrograph of a QSKIP with 100 squares and 12 μm wide YBCO. The left half of the QSKIP is covered by a light shield leaving only the rightside exposed.

The QSKIP mask is shown in Section 4, and includes nine devices of various size. The QSKIP is designed with a YBCO line width of 6 and 12 μm. For each width, different number of squares are incorporated: 10 squares, 30 squares, 40 squares, and/or 100 squares. The six QSKIP device types included on the mask are tabulated in Section 4, with the corresponding SQUID inductance and desired SQUID critical current I_{SQ}. These

devices are fabricated with a two level YBCO process outlined below. All the leads from the QSKIP device to bonding pads are made from YBCO and reinforced with gold metal, which also acts as the light shield for covering the right side of the device. A Description of the QSKIP fabrication process is given in section 4.0

3.0 EXPERIMENTAL APPROACH

The experimental approach and measurement results are described in this section. The Optical/Electrical test station used on this program was designed, developed and purchased on company funds. The preamplifiers for interfacing with, and reading out, the QSKIP were customized on program funds. The Optical/Electrical test station, shown in Figure 3.1, is generic in capability, and is intended to measure photoresponse in semiconducting and superconducting photodetectors. Data recording and control of the Optical/Electrical test station is computer controlled with LabView for Windows software. The optics were designed to operate over a very wide spectral band (3μm-100μm) and are described in section 3.1. The cryogenics incorporated into the test station allow for operating photodetectors between 5-300K, and these are described in section 3.3. The wide spectra response and cryogenic temperature range make this Optical/Electrical test station very suitable for testing superconducting quantum photodetectors under development on this program. The portion of the Optical/Electrical test stations specifically designed for operating and readout of the QSKIP are desribed in section 3.2. A special packaging approach for handling the QSKIP was developed on previous programs and is described in section 3.4. Finally, in sections 4 and 5, we describe the detector's fabrication and present experimental results, respectively.

3.1 OPTICAL SETUP

The optical setup, assembled on an aluminum breadboard table, includes: (1) a monochrometer, (2) reflecting optics, (3) cooled long pass filters, (4) optical windows, (5) thermopile reference sources, (6) black body source, and (7) chopper. A diagram of the optical setup, including the black body source, focusing optics, and monochrometer is shown in Figure 3.2. Also included in this diagram are the location of the optical elements in the dewar. The optical elements in the dewar include: (1) a window, (2)

cooled (≈80K) filters and attenuators, (3) gold coated mirrors for sampling the incident and reflected optical beam onto thermopiles (not shown) cooled to ≈80K, and (5) the sample location. The sample is located on a cold stage whose temperature can be varied from 5-300K. A description of the optical components in the Optical/Electrical test station and their operation follows.

The **black body source** is made up of a tungsten filament, operated at 2400K. The filament selected is from an OSRAM Halogen projector lamp part number HLX 64655 EHJ. This lamp is rated to operate at 3400K and puts out 10^4 lumens for an average life of 50 Hours. The filament is enclosed in a quartz envelope and operates from a 24 DC power supply. The lamp's hot filament is used as a black body source, accordingly, the quartz envelope was removed because it does not transmit much beyond 4μm. The tungsten filament was isolation from oxygen by enclosing it a specially fabricated vacuum box that had replaceable optical windows and electrical feed-through for powering of the tungsten filament. The replaceable optical windows included KRS-5 (0.6μm- 40μm), clear ZnSe (0.3μm- 18μm), and single crystal silicon (1.1μm- 300μm, with a blocking band between 12 μm- 40μm). These windows span the 3μm- 100μm spectral band and transmit the black body radiation from the tungsten filament within this band.

Several steps were taken to maintain the tungsten filament's lifetime. The operating voltage was reduced from 24 volts to about 12 volts. Additionally, the tungsten filament was enclosed in the vacuum box and evacuated. Next, the vacuum box was filled with an inert gas to a pressure of about 30 psi. Filling with an inert gas provided two advantages: (1) a reduction in the window coating rate from the evaporation of the hot tungsten filament, and (2) the filament could be operated hotter. Out of Argon, Krypton and Xenon we selected Krypton because Xenon was too expensive. This design for the black body source using the tungsten filament enclosed in a box, with different the optical windows, yielded a broad spectral source.

Black Body emission from the optics is minimized by using only **reflective optics** and coating these with **gold**. The Black Body radiation from the tungsten filament is focused on the monochrometer entrance slit. Two gold coated 90^0 off-axis paraboloidal

mirrors (part # 02 POA 013), from Melles Griot, collimate and refocus the black body radiation onto the monochrometer's entrance slit. A metal chopper blade, located less than 3mm in front of the monochrometer entrance slit, modulates the black body radiation. Different gratings, in the monochrometer, filter the Black Body radiation entering the monochrometer is direct it to the monochrometer's exit slit.

Six-gold coated gratings are used to spectrally filter the Black Body radiation and cover the 3μm- 100μm spectral band of interest. The six gratings are assembled on two turrets, with each turret holding three gratings. The monochrometer, model SpectraPro-275, from Acton Research Corporation, holds one three-grating turret at a time. Each turret is easily installed in the monochrometer and no realignment is required. The six grating set span the 3μm- 100μm spectral band according to the list given in Table 3.1. One turret (number 1) contains three gratings, (labeled 1 through 3), and spectrally it span between 3 and 30μm. The second turret (number 2) also contains three gratings (labeled 4 through 6) and spectrally it spans between 30 and 100μm. The monochrometer selects a narrow wavelength band (including higher order harmonics) from the spectrally broad black body radiation. Four Melles Griot gold coated 90^0 off-axis paraboloidal mirror (part # 02 POA 013) collimate the radiation at the monochrometer's entrance and exit slits. The collimated optical radiation reaches the photodetector through the dewar's optical window, and Filters, shown in Fig.-3.3.

#	Grooves /mm	Blaze wavelength	Acton part #	Operating Band	Δλ (for 3mm slit)
1	150 g/mm	4μm	1-015-4	3-6μm	72nm
2	75 g/mm	10μm	1-075-10	6-16μm	144nm
3	20 g/mm	22.5μm	1-02-22.5	16-30μm	540nm
4	20 g/mm	45μm	1-02-45	30-55μm	540nm
5	13.3 g/mm	67μm	1-013.3-67	55-85μm	810nm
6	7.9 g/mm	112μm	1-07.9-112	85-168μm	1365nm

Table 3.1. Operating characteristics of gratings used in this program. The first three gratings were mounted on turret number 1 and the last three are mounted on turret 2.

Inside the dewar (see Figure 3.3) the collimated optical beam is filtered to remove the higher order harmonics. Seven cooled long pass filters are needed to cover the 3μm-

100μm spectral band, and these are listed in Table 3.2. The filters, each 1" in diameter, are mounted in an eight-position wheel and cooled to ≈80K. A knobs, located outside the vacuum wall and mounted on the dewar, rotate the filter wheels to position one of the seven filters (or no filter) in the optical beam path. Cooling these filters to ≈80K greatly reduces filter's black body radiation. A second wheel, (also cooled to ≈80K and located in front of the filter wheel inside the dewar) contains neutral density attenuators that pass 10% and 1% of the incident optical radiation. The second wheel is independently controlled with a second knob mounted outside the dewar. The arrangement with two wheels allows us to filter out the higher order harmonics and attenuate the filtered (narrow-band) optical signal. The filter and grating combinations arranged for spanning the 3μm-100μm spectral band are listed in Table 3.3. The last column indicates the location of the filters in the wheel so the knob mounted outside the dewar can be used to set the dial at the appropriate number (or filter). In Table 3.4, the knob settings for the wheel with the attenuators are listed in the last column.

Filter #	Part Number	Cut-on λ	Transmission @ λ Cut-on
1	PN LP-3000-F	3μm	5%
2	PN LP-6000-F	6μm	5%
3	4-8μm P-12	12μm	20%
4	5-10μm P-16	16μm	35%
5	8-16μm P-22	25μm	20%
6	15-25μm P-40	40μm	20%
7	30-40μm P-62	62μm	20%

Table 3.2. Long pass filters use in set-up. Filters # 1 and # 2 are from the Infrared Optical Products, Inc. Filter # 3, #4, #5,and #6 are from Infrared Laboratories, Inc.

The filtered optical beam inside the dewar is divided into three parts, with cold and gold coated mirrors. One part is reflected by a gold mirror and is used as a reference. A second part is reflected from a thin YBCO film, held at the same temperature as the photodetector. The thin YBCO film and the photodetector are made from the same material. The third part of the filtered optical signal reaches the photodetector located on a temperature controlled cold stage.

Operating Band	# Grating & Part	Filter	Knob Setting
Open	n/a	None	240
3-6μm	(1) 1-015-4	PN LP-3000-F	340
6-12μm	(2) 1-075-10	PN LP-6000-F	440
12-16μm	(2) 1-075-10	4-8μm P-12	540
16-26μm	(3) 1-02-22.5	5-10μm P-16	640
26-30μm	(3) 1-02-22.5	8-16μm P-22	740
30-45μm	(4) 1-02-45	8-16μm P-22	740
45-55μm	(4) 1-02-45	15-25μm P-40	840
55-70μm	(5) 1-013.3-67	15-25μm P-40	840
70-85μm	(5) 1-013.3-67	30-40μm P-62	940
85-100μm	(6) 1-07.9-112	30-40μm P-62	940

Table 3.3. Arrangement of Filters and Gratings for operating in 3-100μm spectral band. Once the operating band is selected, the corresponding grating is rotated into place in the monochrometer and the appropriate filter in the dewar is rotated into the beam path with the knob on the dewar.

Operating Band	Function	Characteristics	Knob Setting
3-100μm	Open	Open	910
3-100μm	Attenuator	1% Pass	810
3-100μm	Attenuator	10% Pass	710
3-100μm	Open	Open	610
3-100μm	Open	Open	510
3-100μm	Open	Open	410
3-100μm	Open	Open	310
3-100μm	Open	Open	210

Table 3.4. Attenuator arrangement in the second wheel, where out of the eight positions, only two are used, for the 1% and 10% neutral density attenuators. Using this two wheel arrangement, these attenuators can be placed in series with any filter in the filter wheel to vary the intensity and spectra of the optical beam.

Two thermopiles (operated at ≈80K and mounted on a cross member located inside the dewar's radiation shield, shown in Figure 3.3), are used to measure the intensity of the incident and reflected optical beams. With these measurements the detector's photoresponse is normalized. Both thermopiles are model 2M, manufactured by Dexter Research Center. These thermopiles have significantly improved responsivity because they are operated in a vacuum and at ≈80K. The responsivities of both

thermopiles have been calibrated with a HeNe laser, at a wavelength of 632.8nm. The thermopile used to measure the incident filtered optical signal has a responsivity of 1425.5 Volts/Watt. The thermopile used to measure the reflected optical signal has a responsivity of 1104.19 Volts/Watt. The thermopile output signals are amplified and recorded on a PC. The electrical setup is described in the next section.

Figure 3.1. Photograph of experimental Optical/Electrical test station used for measuring photodetector photoresponse. Two dewars shown in the background reveal that one is used to cool the radiation shield to ≈80K and the second is used to cool the cold finger as low as 5K. Also visible are the electronics, dewar, optics and computerized data taking and control.

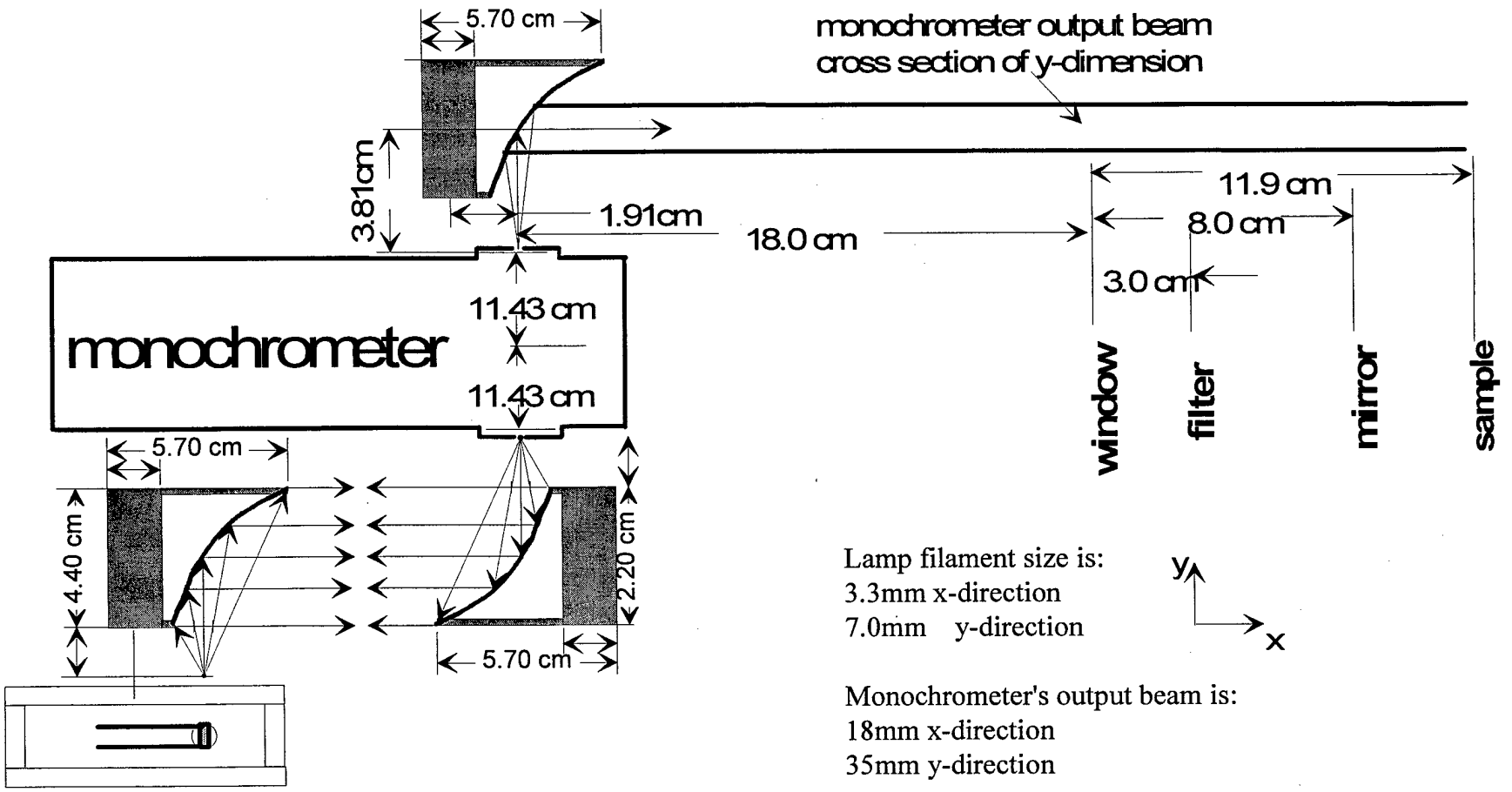

Figure 3.2. The layout of the optical system shown includes: the monochrometer, four paraboloidal mirrors, and the location of the dewar components.

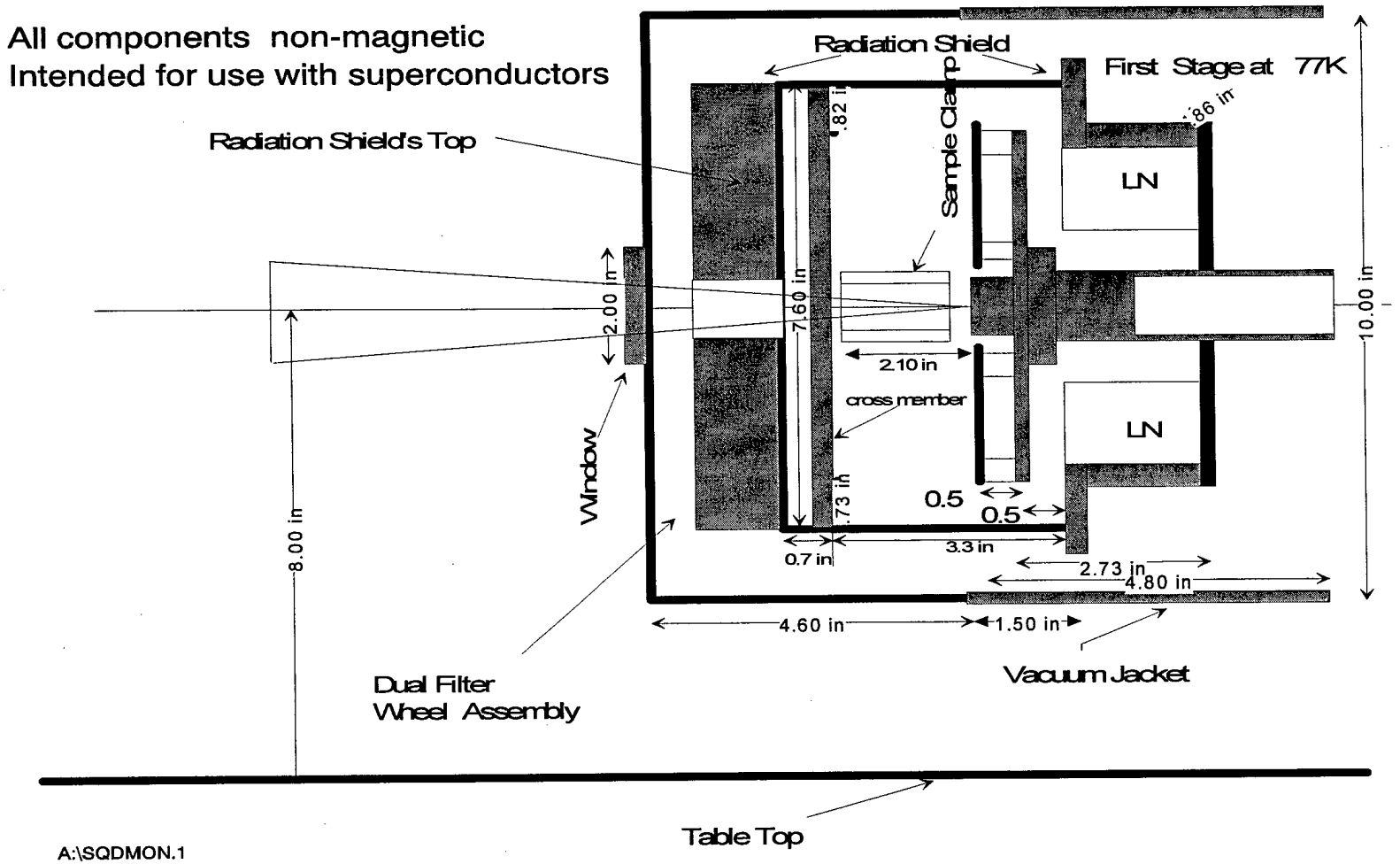

Figure 3.3. Dewar design details reveal an extra liquid nitrogen tank for cooling the radiation shield to ≈80K. The cold finger is cooled by helium to as low as 5K. The dual filter wheel assembly is attached to the top of the radiation shield. A cross member below the dual filter wheel assembly supports two thermopiles used to measure the incident and reflected optical beams.

3.2 ELECTRICAL SETUP

The electrical portion of the Optical/Electrical test stand included: (1) PC data acquisition, (2) signal processing electronics, (3) photodetector bias and readout circuits, (4) electrical interface to, and control of, the optical elements, and (5) temperature control and monitors for the dewar. These elements are described next.

PC data acquisition is used to control the entire experimental setup. A PC with a 486 microprocessor is used to operate the equipment through the GPIB. Incorporated into the PC are two cards made by National Instruments: (1) an AT-GPIB/TNT (PN) interface for IBM PC/AT EISA Bus PC including NI-488.2M, and (2) a multifunction Analog and Digital I/O Bus for IBM PC, model AT-MIO-16E-10. The computerized data acquisition software is based on National Instruments LabView for Windows. All the electronics are initialized through the PC interface, with provisions for a manual override. The initial settings have been programmed into the Virtual Instruments (VI) formed with the LabView software. The VI represents all the electronic instruments on the PC CRT screen and provides controls for operating these through the GPIB. There are three different programs for taking data with the Lab-View software.

One program is used to monitor the resistance of the QSKIP YBCO lines, during cool down, to see if they indeed become superconducting and at what temperature this occurs. This is called the **R-vs-T** program is utilized during QSKIP cool down, and serves as a rough check that the QSKIP is made from a film that becomes superconducting. Clearly, this is a minimum requirement and serves as a check on the operation of the QSKIP and the Optical/Electrical test set up.

Once the QSKIP sample is cooled, it is biased and the second program is executed. The second program, called **I-V squid,** measures the characteristics of the QSKIP readout SQUID. With the characteristics of the readout SQUID measured, the correct operating conditions for the QSKIP are obtained. With these conditions, the QSKIP is tested again by the next program called **Vsquid-vs-Phi.** The purpose of this program is to measure the behavior of the readout SQUID vs magnetic field modulation and establish the conditions wherein the SQUID bias current is minimum. This provides

operating conditions wherein the quiescent voltage, on average, is zero. An photoinduced changes will disturb this equilibrium and result in an output. This output signal is recorded with a program called **Photo-R.** During these tests many different parameters are measured and controls for properly biasing the QSKIP are provided. The parameters measured with the Lab-View for Windows PC software are listed in Table 3.5. The purpose for each of these measurements is also included in the right column, in Table 3.5.

The first three rows, in Table 3.5, are used to establish the AC incident photon flux. The AC incident flux is calculated from two measurements with a thermopile operating at ≈80K. One reading is taken with the chopper blade open and a second reading is taken with the chopper blade closed, the difference between the two readings yield the change in photon flux or the AC incident flux. This is used to compute the AC QSKIP response. The AC measurement is needed to remove the background photon flux, which is very significant in the 3-100μm spectral band.

Rows 4 through 6, in Table 3.5, are used to establish the AC reflected photon flux, by suing two measurements are required. First, with the chopper blade open and closed, the reflected photon flux is measured with a thermopile, at 80K. This measurement is repeated with the chopper blade closed. The difference between these two readings, divided by the normalized incident photon flux, is the normalized reflected photon flux. Using the normalized AC reflected and incident photon flux levels, we compute the how much photon flux is absorbed by the photodetector. From the absorbed photon flux value and the observed photocurrent signal, the QSKIP responsivity is calculated.

During data recording, we monitor the QSKIP voltage, to insure that it remains in the zero resistance state. Rows 7 through 9, in Table 3.5, are used to monitor the voltage across the superconducting photodetector. Two readings are recorded, one with the chopper blade open and a second one with the chopper blade closed. If the superconducting photodetector remains in the zero resistance state (or current state) the difference between these two readings is zero. Taking a difference between two reading circumvents the issue of removing DC offsets present in the voltage reading. If the difference between the two readings is not zero it indicates that the photodetector is not operating in the zero resistance state.

#	Label	Purpose
1	High Incident Photon Reading	Incident flux recording with chopper blade open
2	Low Incident Photon Reading	Incident flux recording with chopper blade closed
3	Delta 1-2 **COMPUTATION**	Incident flux AC amplitude computation
4	High Reflected Photon Reading	Reflected flux recording with chopper blade open
5	Low Reflected Photon Reading	Reflected flux recording with chopper blade closed
6	Delta 4-5 **COMPUTATION**	Reflected flux AC amplitude computation
7	QSKIP High Voltage Reading	Voltage across detector with chopper blade open
8	QSKIP Low Voltage Reading	Voltage across detector with chopper blade closed
9	Delta 7-8 **COMPUTATION**	Voltage change across SC should remain **ZERO**
10	QSKIP High Bias Current	Measures bias current with chopper blade open
11	QSKIP Low Bias Current	Measures bias current with chopper blade closed
12	Delta 10-11 **COMPUTATION**	Insures bias current remains the same
13	Cold Finger Temperature	Reads the cold finger's temperature
14	QSKIP Temperature	Reads the detector's temperature
15	Cold Shield Temperature	Reads the radiation shield's temperature
16	Thermopile Temperature	Reads the thermopile's temperature
17	SQUID Null Current Flux on	SQUID null current with light on
18	SQUID Null Current Flux off	SQUID null current with light off
19	Delta 18-19 **COMPUTATION**	AC photocurrent amplitude
20	Ic SQUID Bias Current	SQUID Bias Current
21	Photon Wavelength	Provides spectral band of incident photon flux
22	DC Lock-in Null Signal	Error signal, zero if 18 &19 are adjusted OK
23	SQUID Flux Bias	Not Used
24	Lamp Voltage	DC Bias voltage on Black Body lamp source
25	V(SQUID)	Voltage across SQUID

Table 3.5. The readings and computations recorded with the PC data acquisition system, used to measure the QSKIP photoresponse, are listed in 25 rows.

The bias current applied to the QSKIP is much larger than the anticipated photocurrent. Thus, we monitor the QSKIP bias current to insure that the measured photocurrent is not corrupted by any changes in the QSKIP bias current. Rows 10 through 12 are used to monitor the current bias of the QSKIP photodetector. One measurement is recorded with the chopper blade open and a second reading is recorded with the chopper blade closed. If the detector bias current remains constant, zero is be the difference between these two readings. Monitoring the voltage and current conditions on the QSKIP is a check to ensure that during different levels of photo-illumination the detector remains in the zero resistance superconducting state and the bias current is constant.

Operating temperature of the QSKIP and dewar are recorded in rows 13 through 16. The cold finger temperature, listed in row 13 of Table 3.5, is measured with a silicon diode sensor, thermally attached to the cold stage. Row 14 represents the temperature inside a leadless chip carrier package containing the photodetector. The temperature is also measured with a silicon diode mounted inside the package. The radiation shield temperature is recorded on line 15 and it represents the temperature of the thermopiles, which are bolted to the radiation shield with a cross member. Provisions are included, by row 16, for adding a second temperature sensor. The second sensor may be used to measure thermal drops across the aluminum cross member bolted the radiation shield.

Rows 17 through 19 monitor the needed offset current for balancing the photodetector signal and placing the SQUID in a predetermined operating mode. The SQUID predetermined operating mode is set by magnetic flux quantum Φo contained inside the loop. The magnetic flux quantum contained inside the loop is adjusted to be $N\Phi o$ or $(N+1/4)\Phi o$ (where N is an integer). With an AC magnetic flux modulation, a SQUID biased at $N\Phi o$ will show an AC output signal at twice the modulation frequency. A SQUID biased at $(N+1/4)\Phi o$ will show an AC output signal will be at the same the frequency as the modulation field. First, with the copper blade closed, the SQUID null current is adjusted to a predetermined SQUID operating condition [$(N+1/4)\Phi o$, or $N\Phi o$], and this null current value is recorded in Row 17. Next, the chopper blade is opened, and the new null current value is obtained by adjusting the null current to return the SQUID to the predetermined operating conditions. This new null current value is recorded in Row 18. The difference between these null measurements is entered in Row 20, and it is the QSKIP AC photoresponse current. This QSKIP responsivity, in units of Amps/Watt, is computed by dividing Row 20 by the absorbed photon flux, obtained from computations and measurements performed in association with the first six Rows in Table 3.5. The number of photons incident are calculated from the wavelength (Row 21) and the spectrophotometer spectral bandwidth $\Delta\lambda$ given in Table 3.1.

The value of the SQUID bias current is recorded in row 20. The dc bias current is manually adjusted to set the SQUID ever so slightly into the voltage state, and thereby achieve maximum sensitivity.

Determination of the SQUID null current is facilitated with a Lock-in that permits accurate monitoring of the first [if (N+1/4)Φo] or second harmonic [if NΦo] of the voltage signal across the SQUID. The Lock-in output voltage is recorded in Row 22. The SQUID null current is manually adjusted with the chopper blade opened and closed, to provide a measure of the AC current responsivity.

Row 23 is not used. Row 24 monitors the voltage applied to the Tungsten filament used as a Black Body source. The voltage across the SQUID is also recorded in Row 25. This is use when the DC characteristics of the QSKIP and SQUID are recorded in a spreadsheet, and later plotted.

All these entries are recorded with the Lab-view for Windows data acquisition system. This approach facilitates data acquisition/analysis and proper operation of the superconducting photodetectors.

The **Signal Processing Electronics** consist of IC preamplifiers and off-the-shelf electronics. The IC preamplifiers, housed inside a breakout aluminum box attached to the dewar, provide gain to improve noise immunity and reduce outside interference. The output from the preamplifiers is channeled to the computer data acquisition system through off-the-shelf electronics.

The signal processing electronics include: (1) a Keithley 182 nanovoltmeter with an IEEE 488 interface, (2) a Keithley 705 scanner with a 7160 nanovolt scanner card and IEEE 488 interface, and (3) an Ithaco 3970 electro-optical lock-in measuring system. These instruments receive the outputs from the preamplifiers connected to the superconducting photodetector as shown in Figure 3.4. The photodetector is located inside the dashed lines drawn in Figure 3.4.

The **photodetector bias circuits** are illustrated in Figure 3.4, where we include the circuits for operating the SQUID readout and QSKIP bias circuits. These circuits built into a custom made PC board. The printed circuit board also included readout amplifiers for the thermopiles and voltage regulators to operate the PC board. All these circuits have been successfully fabricated and used to test the QSKIP devices. Detail on these circuits follow.

Positive and Negative voltage regulators were included on the PC board to minimize circuit noise. The voltage regulators, included on the PC board, are operated from ±15 volts and output ±10 volts. The circuit diagrams for the ±10 volts regulators are shown in Figure 3.5, the top is the plus 10 volts regulator and the bottom is the negative 10 volts regulator. Three volts Lithium batteries are used as a reference for the positive and negative voltage regulators. The combination of the feedback networks around a low noise operational amplifiers step up the three volt battery reference to ten volts. Lithium batteries were used for voltage reference to minimize electrical noise.

The voltage signal from each thermopile is amplified and readout by the circuit shown in Figure 3.6. The same circuit is used to readout the thermopile used for measuring the reflected and incident photon radiation. The thermopile is attached to the readout circuit in a differential manner so as to maximize common mode rejection.

The QSKIP requires separate circuits for operating the detector and SQUID readout circuits. These circuits were designed and integrated into the same PC board with the regulators and the thermopile readout circuits. The circuit for biasing and reading out the SQUID is shown in Figure 3.7.

For best sensitivity, the QSKIP detector requires biasing with a large current, while for maximum readout sensitivity the SQUID critical current should be minimized. The contradictory requirements are satisfied with two loops: one for the QSKIP and a second loop for the SQUID. The diagram in Figure 3.4, enclosed by the dashed lines, reveals a separate loop for the SQUID readout circuit and a second loop for the QSKIP. Part of the SQUID loop coincides with a portion of the QSKIP loop The QSKIP is biased by a single current generator whose current is divided into two halves, with each half flowing to ground through a different portion of the QSKIP loop. The two current halves flow in opposite directions to cancel their phase shift within the SQUID loop. Thus the net phase shift produced by the QSKIP currents within the SQUID loop should be small relative to the QSKIP current amplitude. AC changes in the condensate's phase occur with photoinduced changes in superconducting link's kinetic inductance. These are monitored with a Lock-in amplifier.

Since the QSKIP detector and readout SQUID are symmetrically constructed, the AC signal is generated in a differential manner. Additionally, the noise from the current used to bias the QSKIP undergoes the same cancellations by having these currents flow in opposite directions inside the SQUID loop.

The **electrical interface to optical elements** includes: the monochrometer, the chopper, the black body tungsten filament, and two thermopiles. The Acton Research monochrometer has an electronic control module that interfaces through an IEEE 488 bus with the PC computer to record the operating wavelength. The HMS light beam chopper model 220 interfaces to the computer through the National Instruments AT-GPIB interface for IBM PC/AT EISA Bus PC including NI-488.2M. The Black body tungsten filament is powered by a remote controlled Sorensen SRL 20-12 power supply (0-25VDC, 0-15 Amp). The Sorensen power supply has manual and automatic control options. The output of the supply is adjusted to a maintain a fixed photon flux level as determined by the two thermopiles inside the dewar. Each thermopile is connected to special preamplifier circuit with a gain of 11 (see Figure 3.6) and are calibrated to read the incident photon flux power.

The **temperature control and monitoring** is centered around two Lake Shore 93CA temperature controllers connected via an IEEE 488 bus to a PC. Each controller accepts inputs from two temperature sensors and can power one heater. The heater output in combination with either temperature sensor provides for temperature control. The heater output is a proportional analog signal (not digital) to minimize heater induced electrical interference. The temperature sensors are calibrated silicon diodes with a temperature range between 2K and 300K. The sensor's calibration curves are entered inside the 93CA to provide, at low temperatures, a resolution better than 0.1K.

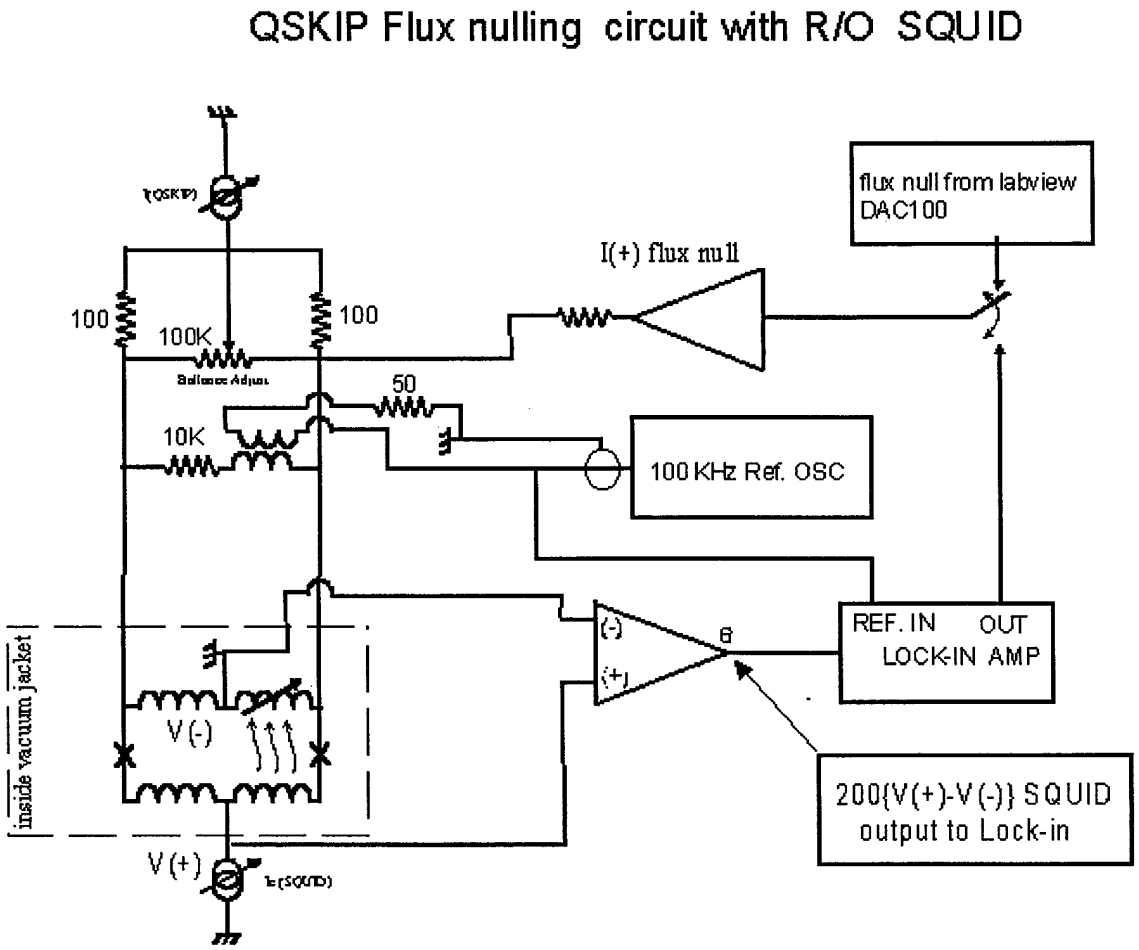

Figure 3.4. Diagram of preamplifier, Lock-in and photodetector bias circuits used for making photoresponse measurements.

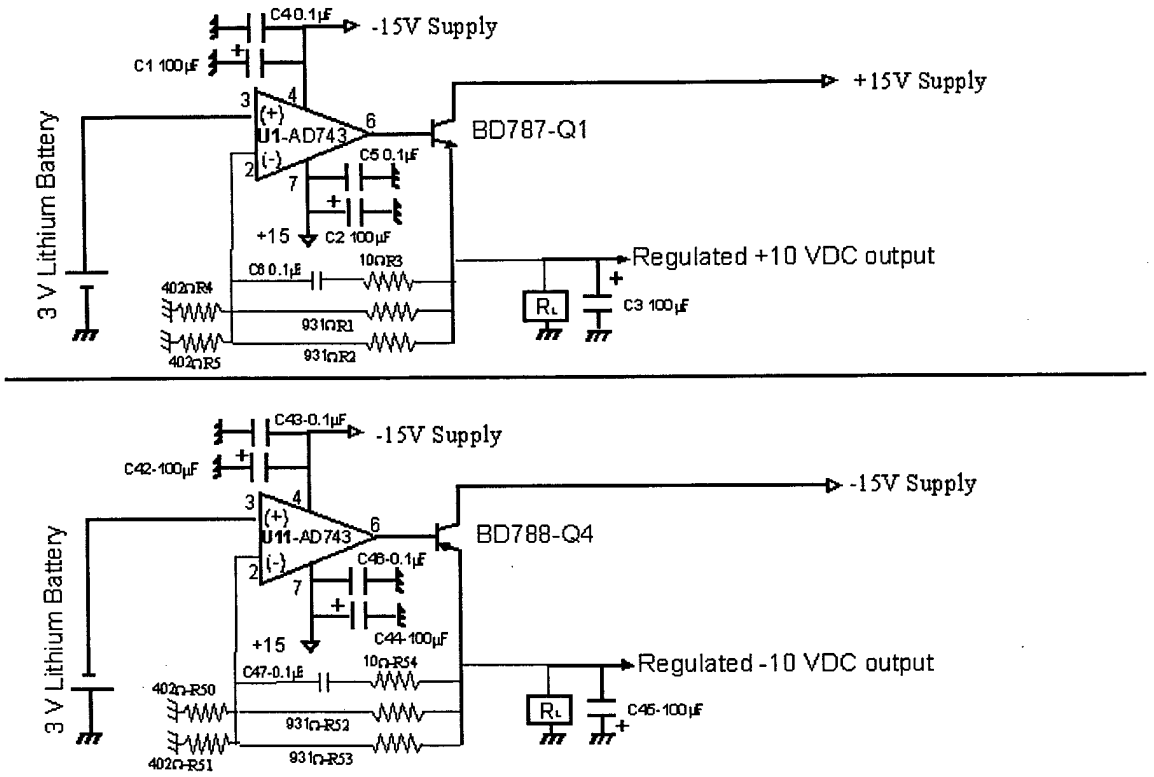

Figure 3.5. Diagram of positive and negative voltage regulator included on PC board.

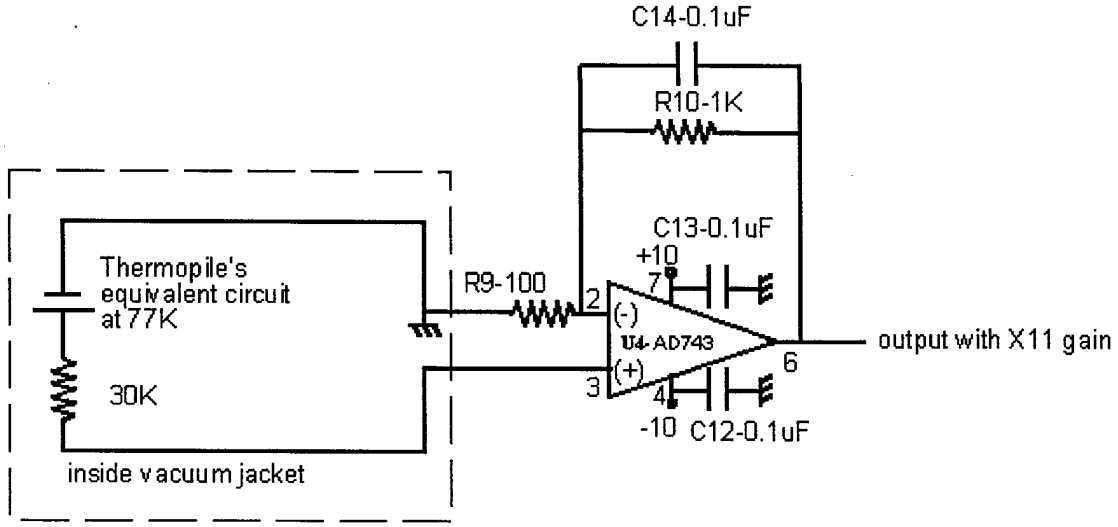

Figure 3.6. Thermopile readout circuit with a voltage gain of eleven. The thermopiles are inside the dewar operating at 80K and are differentially connected to the readout circuit to maximize common mode rejection.

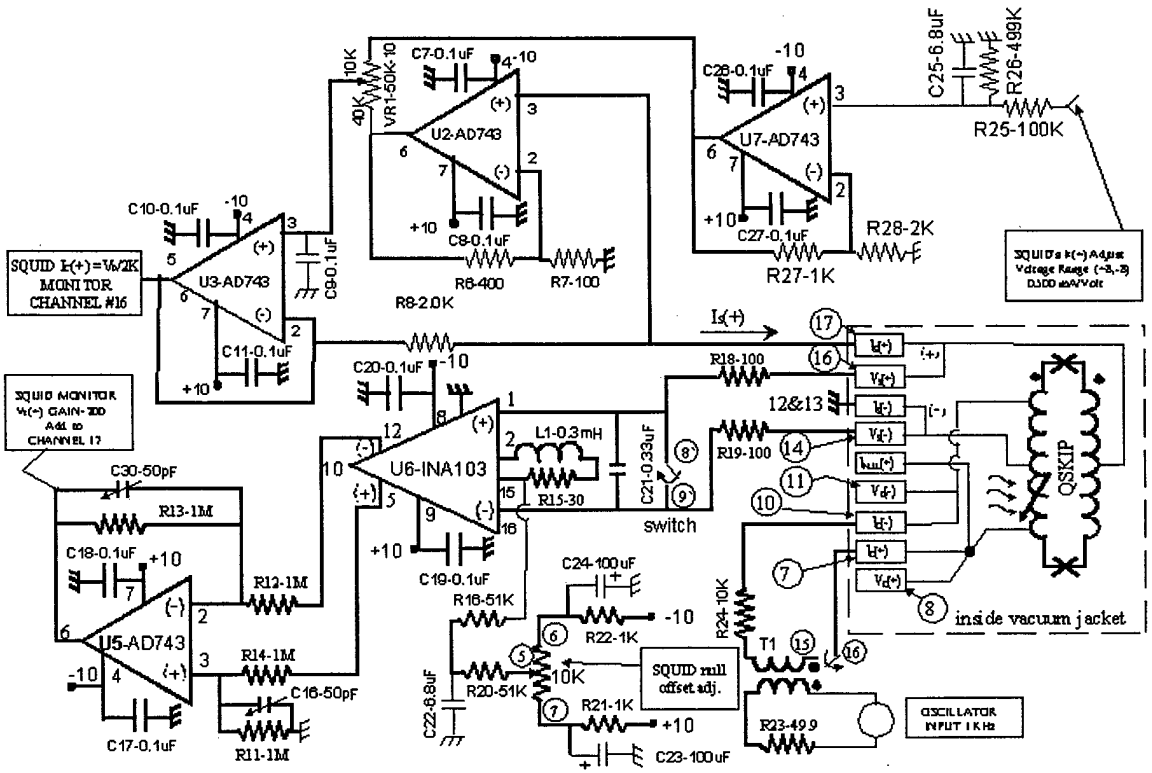

Figure 3.7 Circuit diagrams for the bias and readout amplifiers used to operate the readout SQUID.

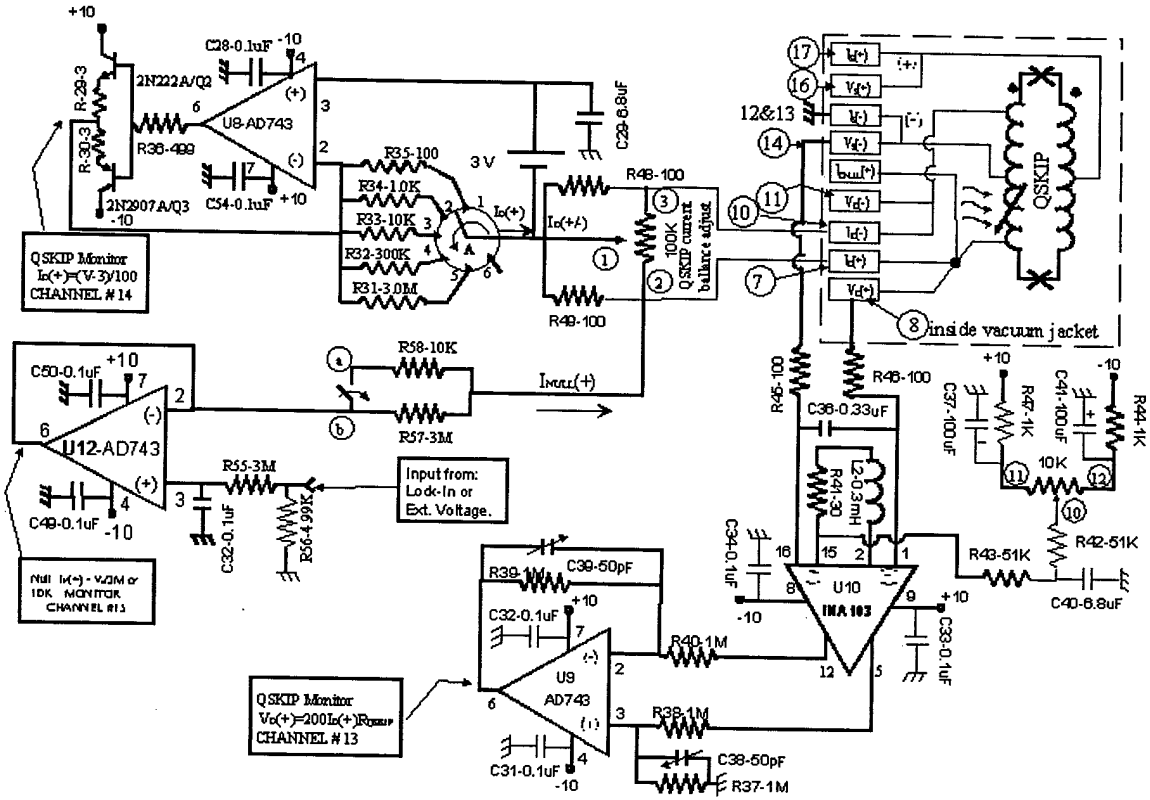

Figure 3.8 Diagrams for the current bias circuits used for operating the QSKIP detector portion. The QSKIP detector is included in the circuit diagram.

3.3 CRYOGENIC SETUP

The dewar is a modified Lake Shore Cryotronics (see Figure 3.3), model MTD 150. The dewar is wired with phosphorous bronze #36 twisted pairs wires, purchased from Lake Shore as part #DT36. Twisted pair wires are used to reduce electrical pickup, and this is especially important when operating a SQUID, which has extremely wide band. The wires are insulated with polyimide insulation and are about 12 inches long. To minimize thermal loading, we have wired only 38 pins to an 84 pin LCC package. The QSKIP is thermally and electrically attached inside a specially modified leadless chip carrier (LCC) 84-pin package. A square hole is machined inside the socket to accommodate an aluminum pedestal that is attached to the cold finger. Several change were made to improve thermal and electrical connections in the MTD 150 dewar and these are described below.

The original dewar arrangement made use of a single clamp to make electrical and thermal contact between the LCC package and the dewar's socket and aluminum pedestal. This arrangement was changed to provide two independent pressure clamps: one to make electrical contact to the LCC package, and a second to make thermal contact to the aluminum pedestal, bolted to the cold finger. This modification required splitting the circular fan-out board inside the dewar into two board. The two boards, were concentric and attached to each other by flexible wires. The smaller printed circuit board included the LCC socket and provisions for clamp the 84 pin LCC package inside the socket. This clamp established electrical contact to the QSKIP and is independent of a second clamp which is used to press the package/socket assembly onto the aluminum pedestal and makes good thermal contact. With the two independent clamp arrangement, good electrical and thermal contact are independently established. This is important given the fact that the packaged devices are loaded into the dewar at room temperature and cycled between 5-300K. Cycling devices over such a wide temperature range requires provisions for accommodating mechanical mismatches in the thermal expansion coefficients. The two clamps provide the additional degree of freedom to accomplish this feature.

The modified dewar included two separate cryogenic inputs. The radiation shield, the two filter wheels, and the thermopiles were cooled by liquid nitrogen through separate

cryogenic lines. This permitted us to cool most of the dewar mass with liquid nitrogen and saved both cool down time and liquid helium consumption. The second cryogenic input was from liquid helium that allowed us to cool the sample to about 5K. In operation, liquid nitrogen and liquid helium were transferred at the same time to speed up cool down. After cool down, the liquid nitrogen valve was turned off and the radiation shield remained close to 77K. The cold finger temperature was varied between 5-77K.

To reduce electrical interference, a Mu-metal magnetic shield was incorporated in the dewar. The shield, purchased from Advance Magnetics, was custom designed and made from RMA 1084 material. The shield was assembled from several pieces so it could be incorporated into the dewar. As designed the shield was easily added to the dewar after all the electrical, cryogenic, vacuum, and optical elements were incorporated.

3.4. DETECTOR PACKAGING

Testing of the QSKIP requires provisions for dealing with large thermal expansion mismatch between the photodetector and package material. Additionally, operation at liquid helium temperatures requires excellent thermal contact between the package and the cold finger. We developed a method, on Westinghouse funds, for packaging superconducting IC's in modified ceramic packages, which resolves the thermal expansion mismatch and reduces thermal drops across the package.

The packaging approach is compatible with conventional bonding of integrated circuits into packages that fit in conventional sockets. The socket used is for an 84 pin LCC package, Kyocera part number PB-0289, and is integrated into the Lake Shore Cryotronics MTD-150 open cycle dewar.

The thermal mismatch is resolved by using a metallic base material (for good thermal conductivity) that has an thermal expansion coefficient close to the substrate the superconductor material is grown on, typically $LaAlO_3$ or $NdGaO_3$. Table 3.6 lists thermal expansion coefficient for several materials. For a $LaAlO_3$ substrate, beryllium, niobium and tantalum offer very good thermal matches (1300 vs 1300, 1290, and 1279). Niobium and tantalum are potentially good choices. However, as niobium becomes

superconducting at 9.2K (vs 4.43K for tantalum) its thermal conductivity also begins to decrease drastically at 9.2K. Therefore, for operating down to about 4.5K we chose to use tantalum.

MATERIAL	$\Delta L/L \times 10^6$	MATERIAL	$\Delta L/L \times 10^6$
$LaAlO_3$	1300	SS Monel	2450
Niobium	1290	SS 301	2300
Tantalum	1270	SS 321	2600
Molybdenum	894	SS 316	2770
Iron Fe	1890	SS 304	2790
Beryllium	1300	Titanium	1700
Aluminum	3910	Poly-Alumina	791

Table 3.6. Total thermal contraction difference $\Delta L/L$ between 300K to 77K for different candidate substrate.

Incorporating a tantalum base into the 84 pin LCC alumina package requires package modification. A 1 cm diameter hole was drilled in the 84 pin LCC package to remove the alumina that the IC in normally mounted on (see Figure 3.9). The hole was sufficiently small to be confined within the package well and thus not damage the electrical lines inside the package. The hole removes the bottom of the IC well which is replaced by the tantalum base(see Figure 3.9).

The base is made from approximately 0.05cm thick tantalum sheet cut into a 2.4 cm square. The 2.4 cm square size is sufficiently small to fit within the electrical contact frame located on the back of the ceramic package, about 2.86 cm square. The processing and assembly needed to incorporate this tantalum base are described next.

A tantalum sheet is first plated with about 10μm of copper on both sides and then cut into 2.4 cm squares. The plated tantalum squares receive about 120μm of Indium on the front side, for a total base thickness of about 620μm. The QSKIP devices are soldering to the indium-coated tantalum base. The soldering is performed by placing the device (with a gold coated back) on a SnInCd solder preform in the center of the indium-coated

tantalum base. This assembly is placed into an oven and heated to 130°C and cooled to room temperature. This thermal cycle solders the Multispectral QSKIP device to the indium-coated tantalum base with the SnInCd solder whose melting temperature is 95°C. The tantalum base with the Multispectral QSKIP device is glued to the back of the ceramic package as shown in Figure 3.10.

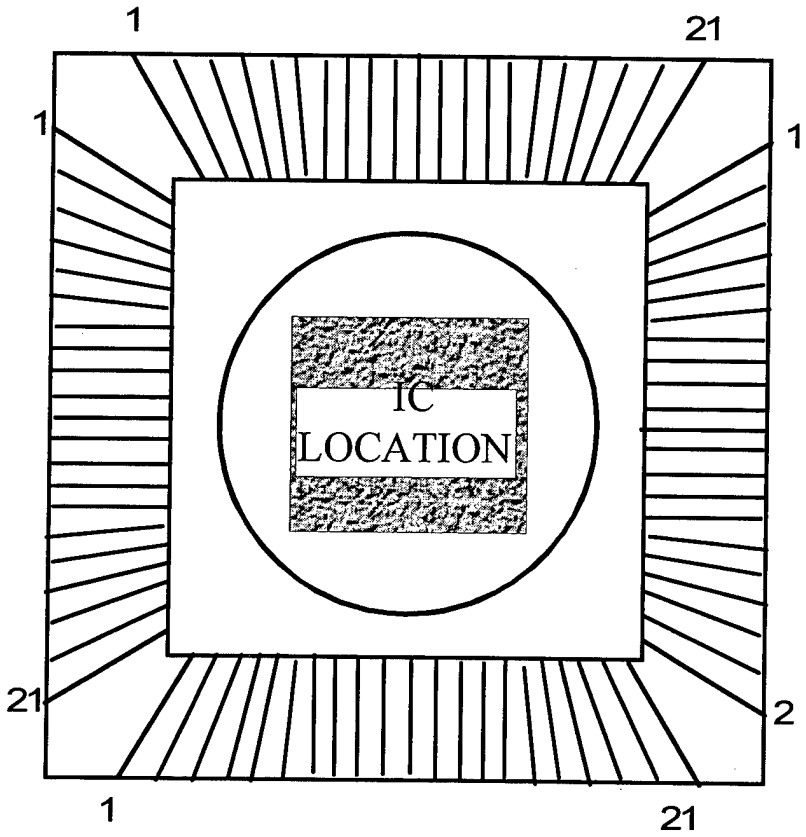

Figure 3.9. Schematic of 84 pin leadless chip carrier package with hole drilled in IC cavity. The hole, indicated by the circle, is 1 cm in diameter, which is sufficiently large for the IC to fit inside.

With this assembly, the soft indium, located between the tantalum base and the alumina LCC package, provides mechanical compliance to accommodate thermal expansion mismatch. The fast setting glue, (Super Bonder 495 made by Loctite) is used for ease of assembly. When the QSKIP device, the tantalum base, and package are assembled, ultrasonic bonding is used to bond the Multispectral QSKIP to the LCC package frame. The completed assembly is shown in Figure 3.11, with the electrical

contact pads exposed on the back. With this arrangement, the electrical contact between the socket and LCC package is through the original contact pads, located on the package's back side.

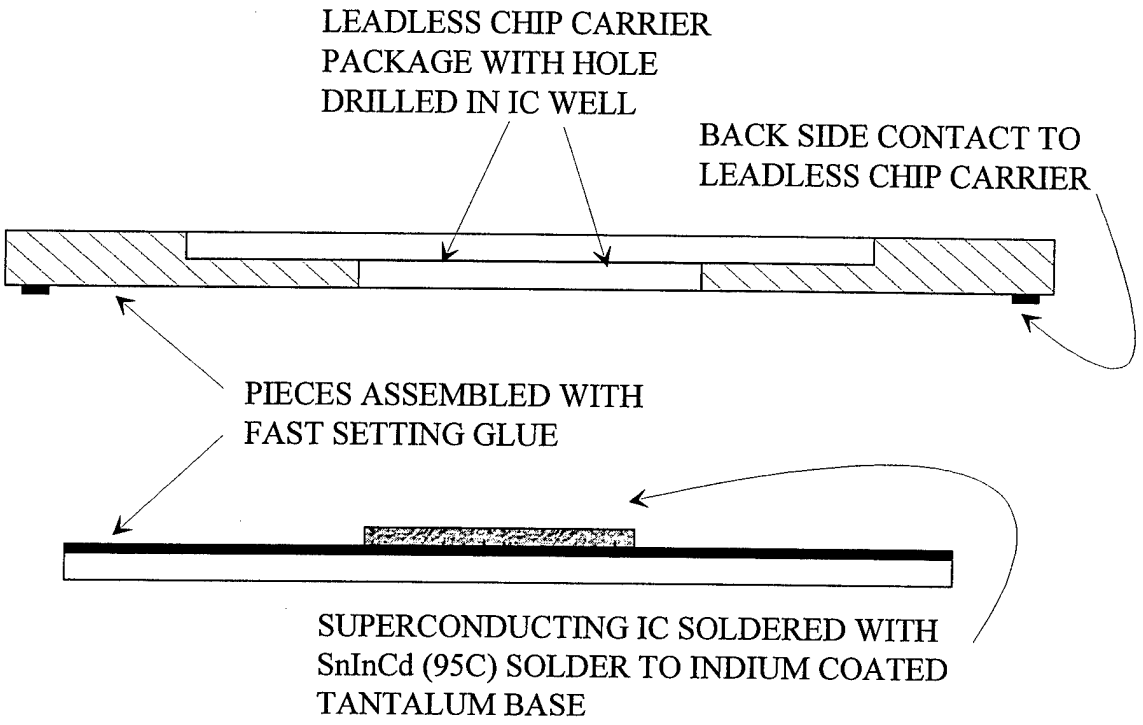

Figure 3.10. Illustration of assembly of indium-coated tantalum base, with IC attached, before being glued to back of ceramic package.

The packaging scheme has been implemented and QSKIP devices have been placed in a dewar and cooled down to about 5K. Unlike previous approaches, the QSKIP device did not sheer off the tantalum base after several cycles between 300K and 5K. This is a significant improvement over previous attempts where the QSKIP was placed directly inside a 84 pin ceramic package. This technique is appropriate for packaging different IC made with high and/or low temperature superconductors.

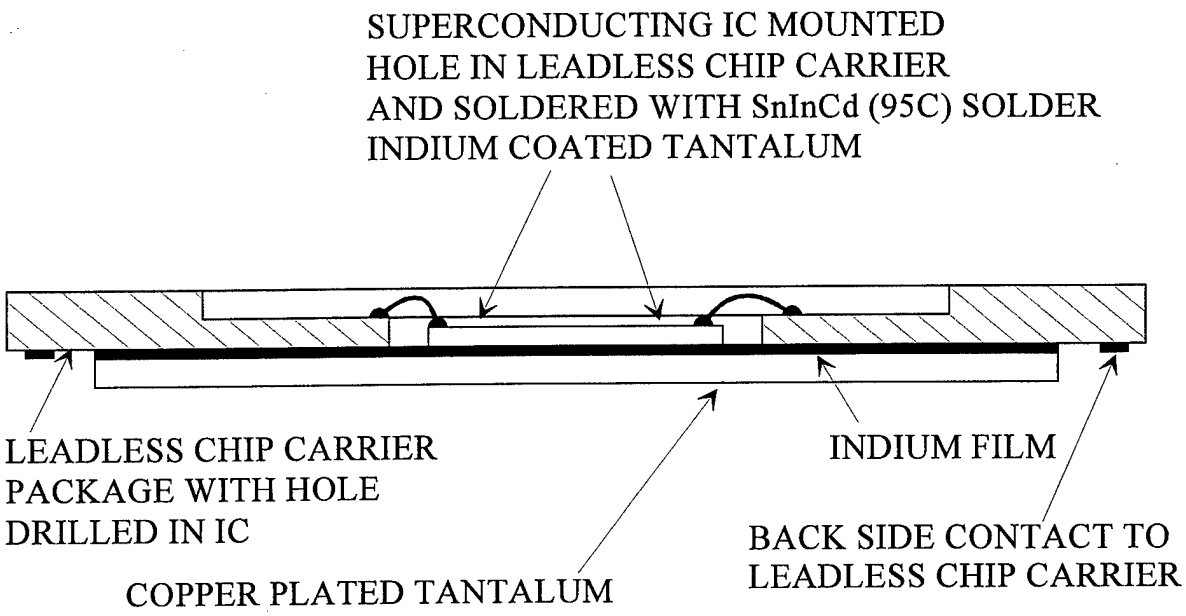

Figure 3.11. Assembly of tantalum base, with IC soldered to it, glued to the back of a ceramic package pre-drilled with a hole in the IC well.

4.0 DETECTOR FABRICATION

Detector fabrication was based on a two-YBCO-layer process, incorporating edge SNS junctions with Co-doped YBCO interlayers. Initial devices were fabricated using a $SrTiO_3$ insulator ($\varepsilon \sim 1000$), but this led to excessive detector capacitance, resulting in highly hysteretic current-voltage operation of the two-junction SQUID, and thus more complex operation. Subsequent devices were made with lower-ε insulators such as LSAT.

There are four mask levels with several processing steps used for fabricating the QSKIP detectors with SQUID readout circuits. These are outlined briefly below. The detailed process steps are as follows:

1. Deposit 100-150 nm YBCO base electrode by Pulsed Laser Deposition (PLD) on a single-crytstal $NdGaO_3$ substrate.
2. Pattern YBCO base electrode by ion milling (Mask 1), using a process designed to produce an edge taper of 30 degrees with respect to the substrate.

3. Perform standard clean-up: 10-minute O_2 plasma followed by 3-minute ion mill (150 V, 20% O_2 in Ar, 45 degree angle) followed by 10 sec etch in 0.3% Br in methanol.
4. Deposit 200 nm epitaxial insulator (such as Sr_2AlTaO_6 or $LaAlO_3$–Sr_2AlTaO_6 [LSAT]) by PLD.
5. Pattern epitaxial insulator by ion milling (Mask 2), milling through both the insulator and selected portions of the underlying YBCO, in order to form a fresh base electrode edge on which to form the edge SNS junction.
6. Perform standard clean-up (See step 3).
7. Deposit typically 10-30 nm of a non-superconducting layer, such as $YBa_2Cu_{2.79}Co_{0.21}O_x$ or $Y_{1-x}Pr_xBa_2Cu_3O_y$, followed by nominally 100-200nm YBCO counterelectrode, and 200 nm in-situ Au.
8. Pattern YBCO/Au counterelectrode and normal layer using ion milling, to define top layer of detector and junctions.
9. Remove Au from one half of detector by ion milling, in order to let light in.

A completed detector is shown in Fig. 2.6. Each chip contained nine detector devices, with various lengths and widths of inductors, as summarized in the following table.

YBCO Width(μm)	Num. Of Squares	Inductance(pH)	I_{SQ}(μA)
6	10	10	100
6	30	30	30
6	100	100	10
12	10	10	100
12	40	40	25
12	100	100	10

5.0 QSKIP Testing and Results

In this program, two candidate multispectral superconducting detectors were fabricated: (1) Superconducting ring geometry photodetector, and (2) Large geometry

SQUID photodetector. The superconducting ring geometry photodetectors (see Figures 2.1 and 2.2) were fabricated first, and results on this device are presented next.

A photomicrograph of such a detector is shown in Figure 5.1, with details of the SQUID readout circuit (located at the bottom in Figure 5.1) are shown in Figure 5.2. The right side of the photodetector is symmetric with the left side. The right and left photodetector sides are configured into a serpentine pattern to increase the kinetic inductance. A gold light shield covers the SQUID readout and one side of the photodetector. The SQUID readout consists of two Josephson junctions formed from a bicrystal boundary. Such devices were packaged and examined electrically and optically.

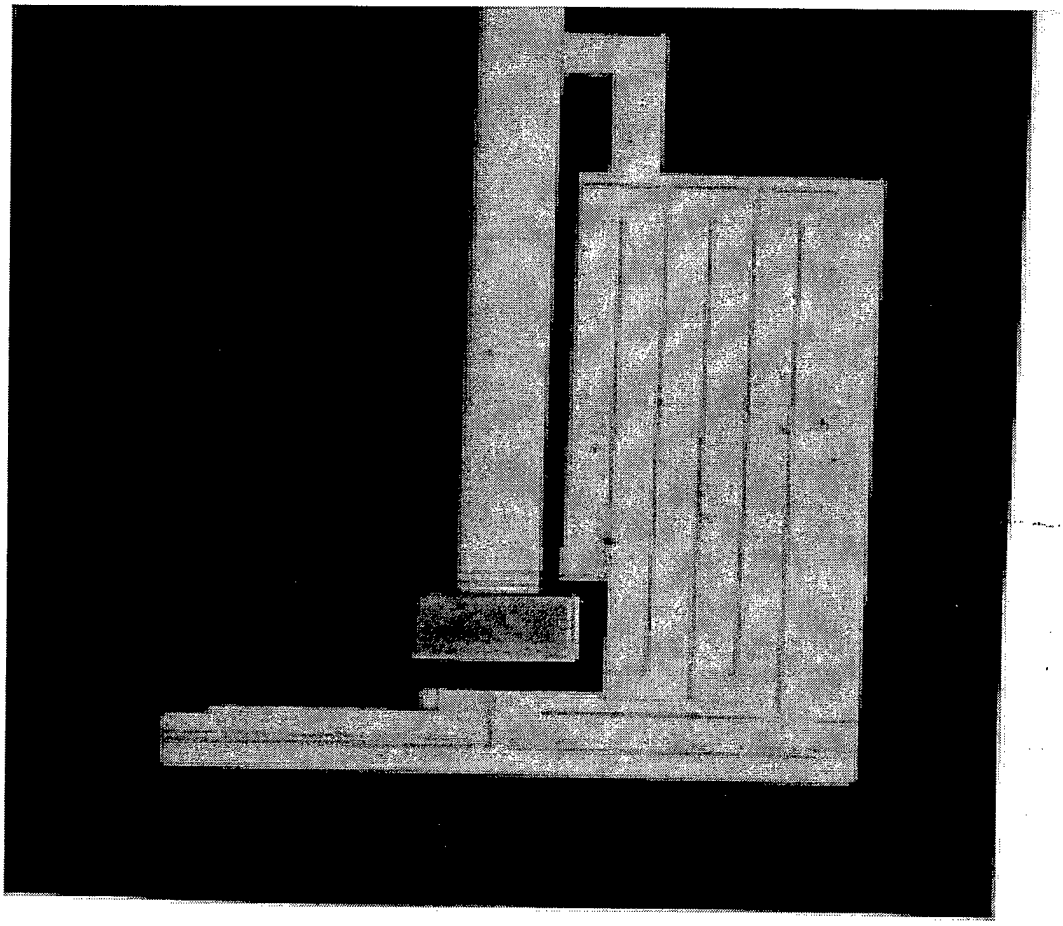

Figure 5.1. A photomicrograph of the Multispectral 100x100μm QSKIP designed and fabricated in this program. The photodetector is made of symmetric YBCO serpentine left and right portions with a YBCO SQUID readout located at the bottom.

A DC current is used to bias the photodetector, with a serpentine geometry. The 0.1μm thick YBCO photodetector occupies a 100μm x 100μm square. Each serpentine branch is about 700μm long and 11μm wide. For this geometry, the resistivity of as deposited YBCO film should be about 300μΩ-cm at 300K. The R vs T curve, taken at 10μA bias current, reveals that the detector's resistance is about 8.125KΩ, at 300K. This reveals an increase in resistivity from about 300μΩ-cm to 2,553 μΩ-cm, at 300K. The almost nine fold increase in the YBCO's room temperature resistivity represents process induced degradation which also effected the transition temperature.

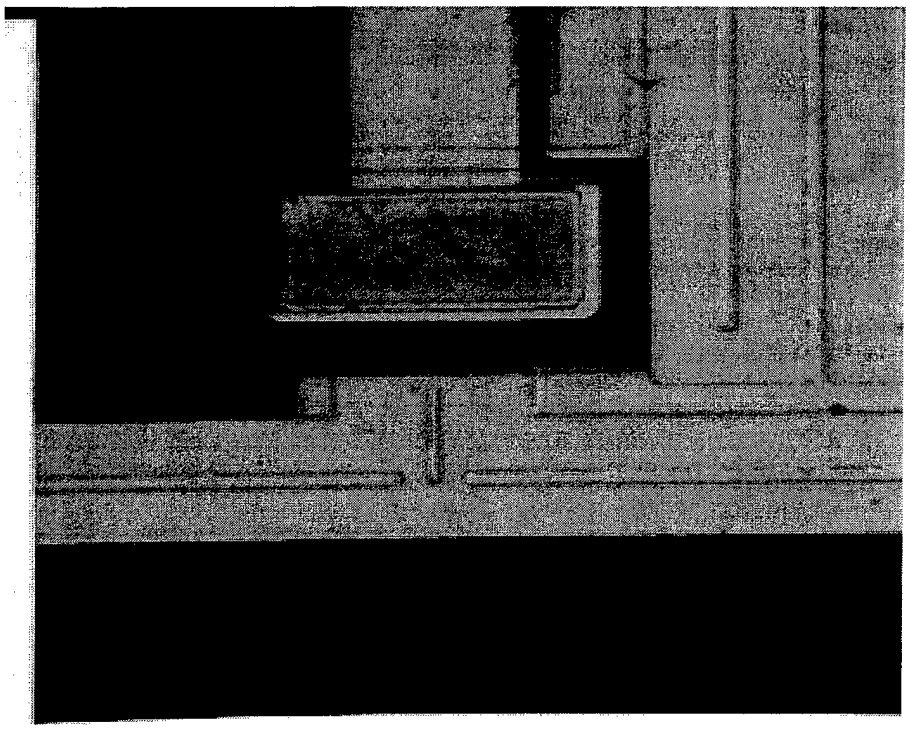

Figure 5.2. Photomicrograph details of the YBCO SQUID made on a bicrystal boundary and covered with gold. The YBCO SQUID reads the photoinduced changes in the currents flowing in the right and left sides of the QSKIP.
pumped down and ready for cryogenic testing.

The YBCO photodetector transition temperature is about 65K. Figure 5.3 shows a plot of the superconducting transition temperature of the YBCO detector. Thus, processing had degraded the YBCO's transition temperature from 89K to 65K. The damage was attributed to silicon poisoning by the silicon dioxide layer, covering the YBCO. This

sputtered silicon dioxide is used to provide electrical isolation between the gold interconnect lines and the YBCO film.

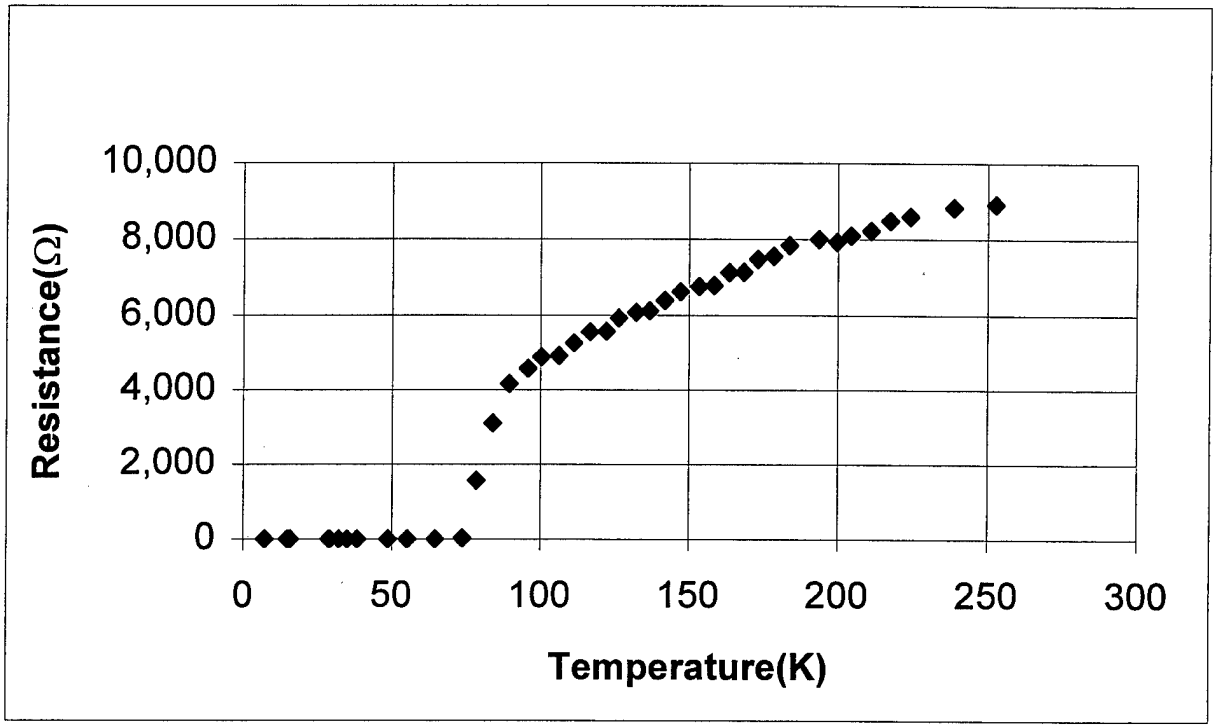

Figure 5.3. R vs T plot of YBCO in a multispectral QSKIP structure. The resistivity has increased almost nine fold over the resistivity of as deposited YBCO films.

The silicon poisoning conclusion was verified experimentally. The oxide covering the YBCO film was stripped and the films were reoxygenated. Thermal cycles in oxygen ambient at 400C did not increase the transition temperature to 85K. The reduced transition temperature did not increase, leading us to conclude that some silicon has diffused into the YBCO sample to produce irreversible reductions in T_C. Careful tuning of the silicon dioxide deposition process improved the YBCO film quality, without reducing the transition temperature.

It is expected that a reduced transition temperature and an increased resistivity is consistent with a significant reduction in the intrinsic quasiparticle's lifetime. The absence of a photoresponse in these devices is attributed to a significant degradation in the quasiparticles lifetime.

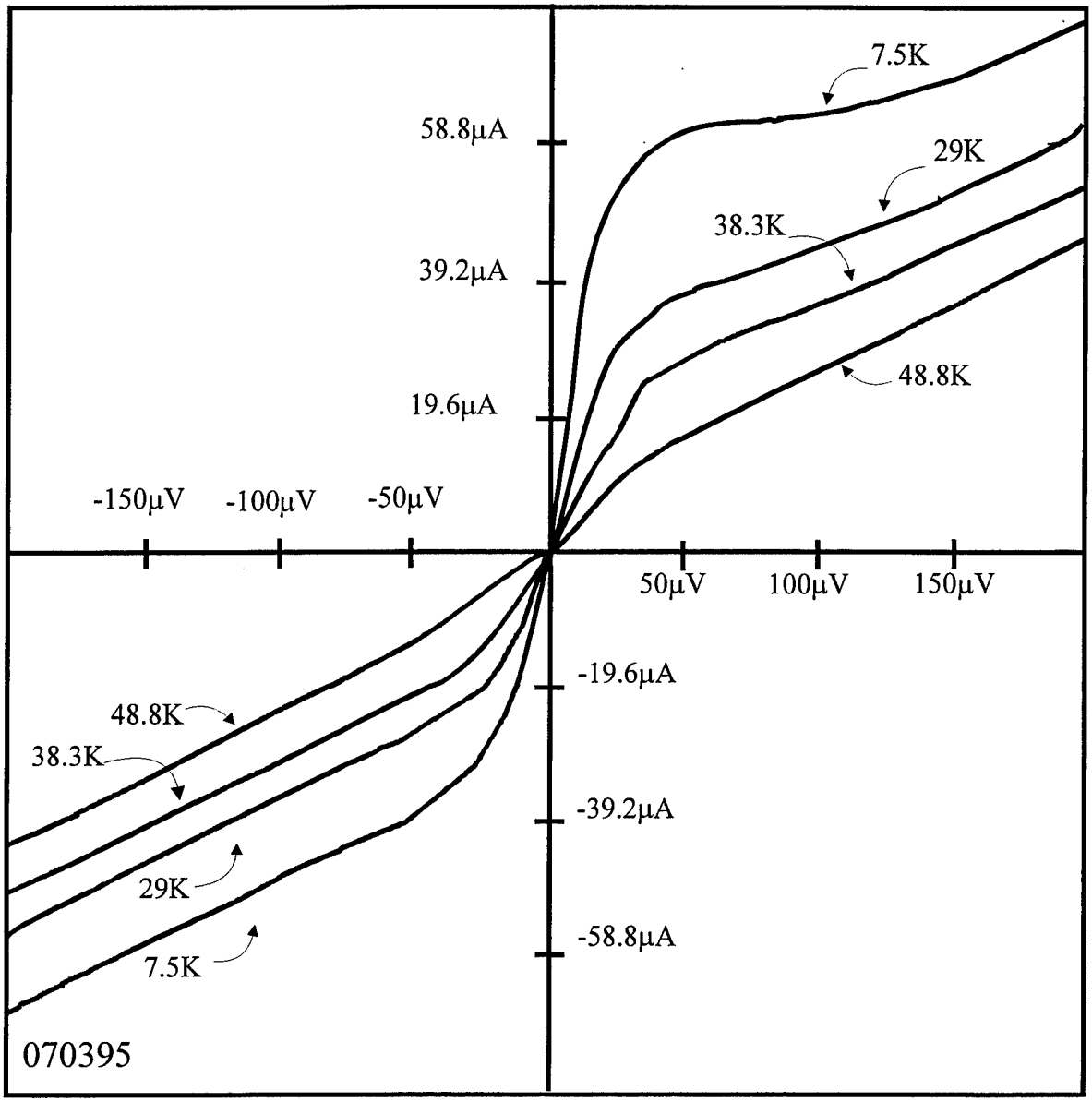

Figure 5.4 YBCO SQUID with grain boundary junctions made on a $SrTiO_3$ bicrystal. The SQUID I-V curves are shown as a function of operating temperature.

The QSKIP YBCO readout SQUID is made on a 24° $SrTiO_3$ bicrystal substrate. The I_CR_N SQUID product is about 40μV at 4.6 K. The SQUID I-V curves were also measured at higher temperatures between 5.5K and 48K, see Figure 5.4. SQUID action is observed at the lower temperatures between 4.5K and 5.5K. The critical current of the SQUID at 5.5K was about 60μA and decreases to zero at 48.8K. These SQUID characteristics are not as good as for a niobium SQUID incorporated with a YBCO detector (see Figure 5.5). The

poor SQUID IV characteristics motivated us to formulate a better detector with better SQUID characteristics.

The multispectral QSKIP was tested for photoresponse at 7.5K. No photoresponse was detected. The lack of a photoresponse is attributed to a reduced lifetime caused by processing the YBCO. The SQUID I_CR_N product at 4.2K is also low, about 40μV. Such a low value further increases the difficulty of seeing a small photoresponse signal since the photodetector output is directly proportional to the SQUID's I_CR_N product. If one assumes an "s" wave superconductor, the SQUID's I_CR_N product is limited to about $2\Delta \approx 3.5kT_C \approx$ 27meV. This theoretical value is almost three orders of magnitude larger than the measured SQUID's I_CR_N product of 40μV. We attribute the lack of a photoresponse to a combination of a degraded YBCO superconducting transition temperature and a SQUID with a low 40μV I_CR_N product. Moving away from SQUIDs based on grain boundary junctions and using instead shallow edge junctions made with PBCO should improve the performance of the readout circuit's. Such changes have been made with the large geometry SQUID detector and are presented next.

Results obtained from measurements on the large geometry SQUID photodetector are reported on next. This detector was fabricated and tested in the second half of this program. The detector is illustrated with a diagram shown in Figure 2.4. The physical layout is shown in Figure 2.6 and a photomicrograph is shown in Figure 2.7.

Several lots of the large SQUID photodetector were fabricated. Each lot included sever one square centimeter substrates. On each substrate nine devices were fabricated, according to the layout shown in Figure 5.6. The nine devices were included to obtain different geometry detectors. The SQUID inductance and detector's optical area were the variable on the mask. After fabrication, these devices were electrically probed at room temperature. The purpose of the electrical room temperature probing was to examine for circuit continuity between the different bonding pads. Clearly, superconductivity and SQUID action cannot be tested with the room temperature tests. However, from the resistance measurements it can be ascertained, with a reasonable degree of confidence which devices are likely to be good.

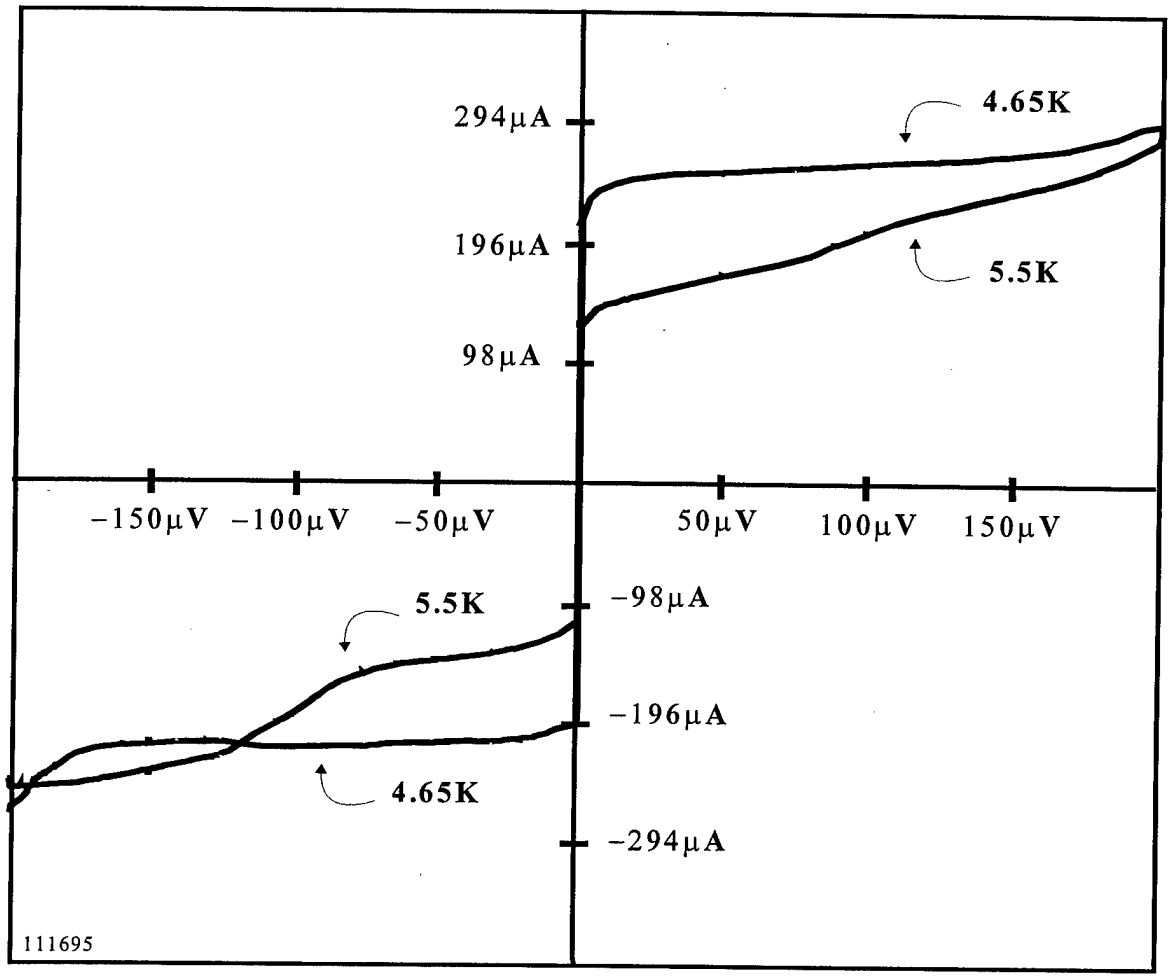

Figure 5.5 Characteristics of a niobium SQUID incorporated with a YBCO detector fabricated on a navy contract.

The room temperature probing reduce the likelihood that a bad device is packaged and loaded into a dewar. The probing is performed with a Tektronix Transistor Curve Tracing Oscilloscope thereby insuring that the current and voltage levels remain small. The results from the room temperature probe tests are illustrated in Figure 5.7 for device L97-135-N1. The probing is repeated after a single device (out of the nine) is packaged. After packaging the one centimeter substrate, one device is bonded and the room temperature tests are repeated to ensure that the device was not damaged in packaging. Good electrical contact between the bonding pads, following packaging, indicates the device is ready for loading into the dewar and for cryogenic tests.

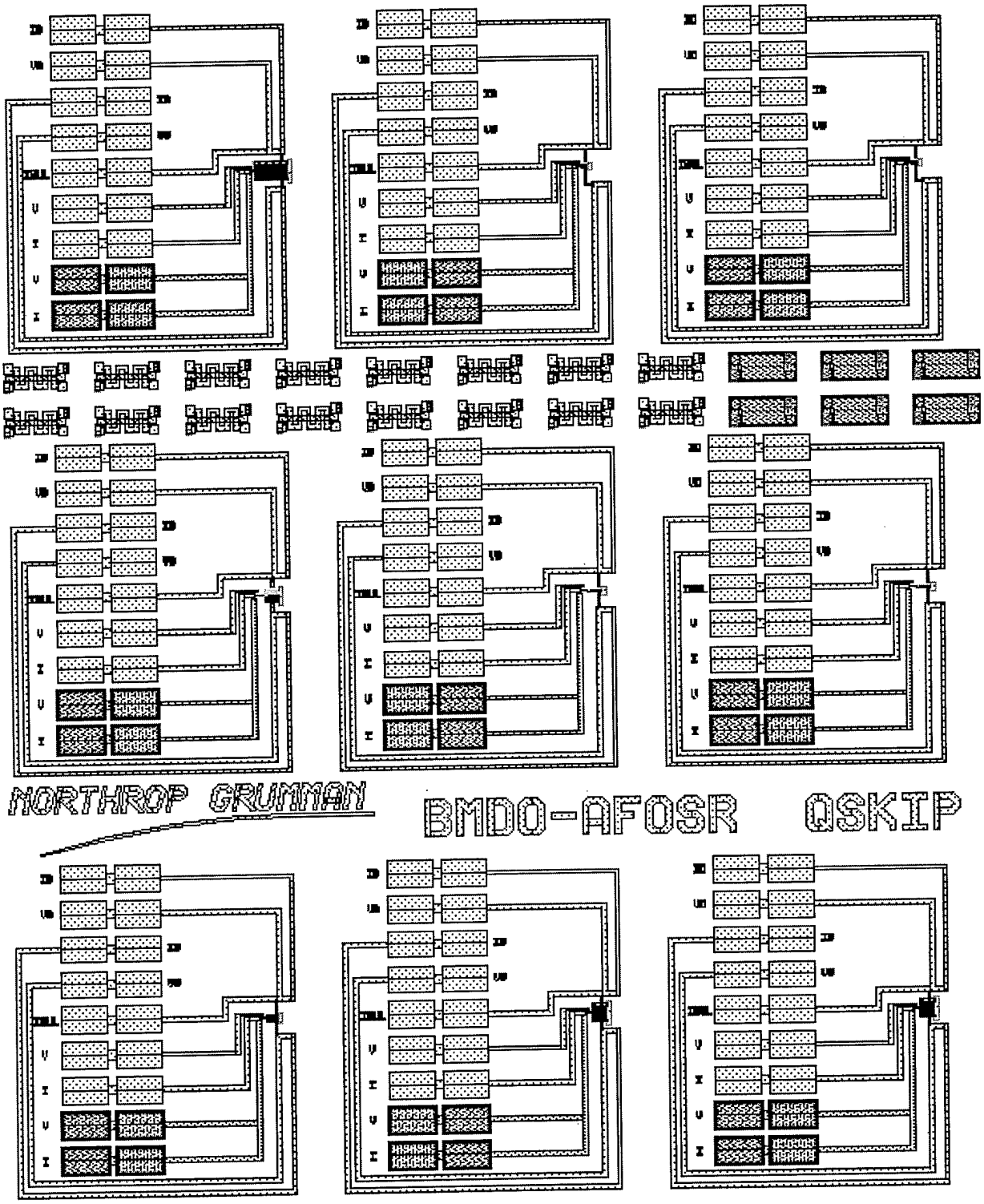

Figure 5.6. QSKIP mask includes 9 devices grouped into three rows, each with three devices. The QSKIPs are distinguished by geometry (number of squares/YBCO line width). Going from left to right, the top row includes:100sq./12μm, 10sq./6μm, and 10sq./6μm; the second row includes: 100sq./6μm, 30sq./6μm, and 30sq./6μm; the third row includes: 10sq./12μm, 40sq./12μm, and 40sq./12μm.

Room Temperature Probe of Device:

	R-top	R-cntr	R-btom	L-top	L-cntr	L-btom
PINS	R(Ω)	R(Ω)	R(Ω)	R(Ω)	R(Ω)	R(Ω)
17->16	1K	1K	1K			
16->14	open	1.2K	1.2K			
14->13	100	200	83			
13->12	20	29	40			
12->11	80	80	80			
11->10	110	250	116			
10->8	170	250	175			
8->7	45	50	50			

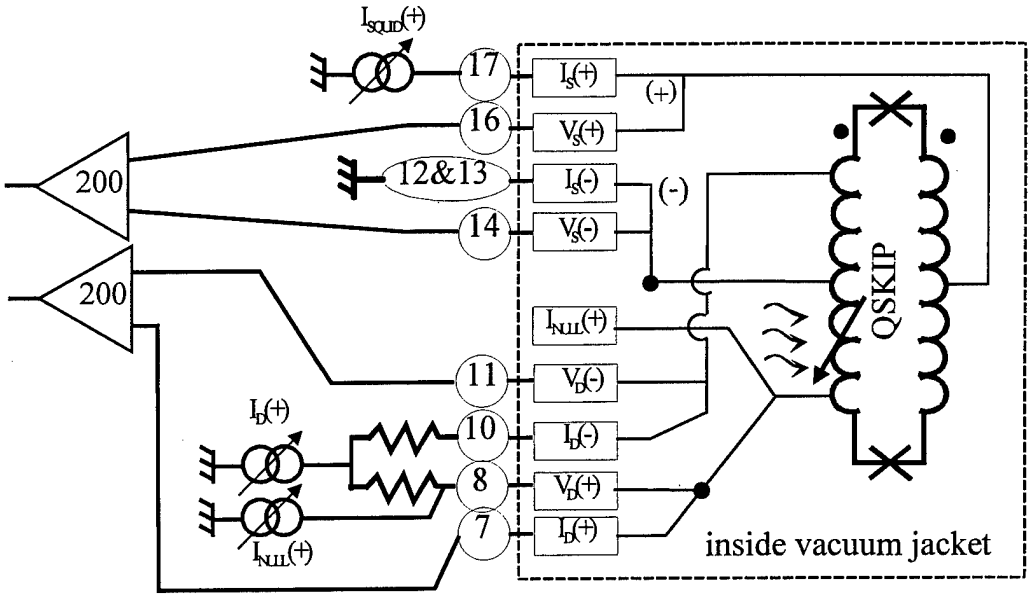

Figure 5.7. Sheet used for recording the electrical probing test at room temperature on QSKIP devices. The tests are repeated at room temperature after the devices are packaged and loaded into the dewar. Test illustrated for device L97-135-N1, with the circuit outline below the table.

For the example following, we selected the smallest device (6μm wide YBCO and with 10 squares) was bonded into a specially designed package for tests described below. After the bonded QSKIP is loaded into the dewar, testing starts with dewar cooling. All tests are performed with computer controlled electronic equipment. During cool down, a simple and necessary test is performed to monitor the change in the YBCO resistance with temperature. This ensures that the YBCO has survived all the steps and remains superconducting after fabrication, probing and packaging. The resistance versus temperature curve is shown in Figure 5.8 for the top center QSKIP L97-135-N1 device.

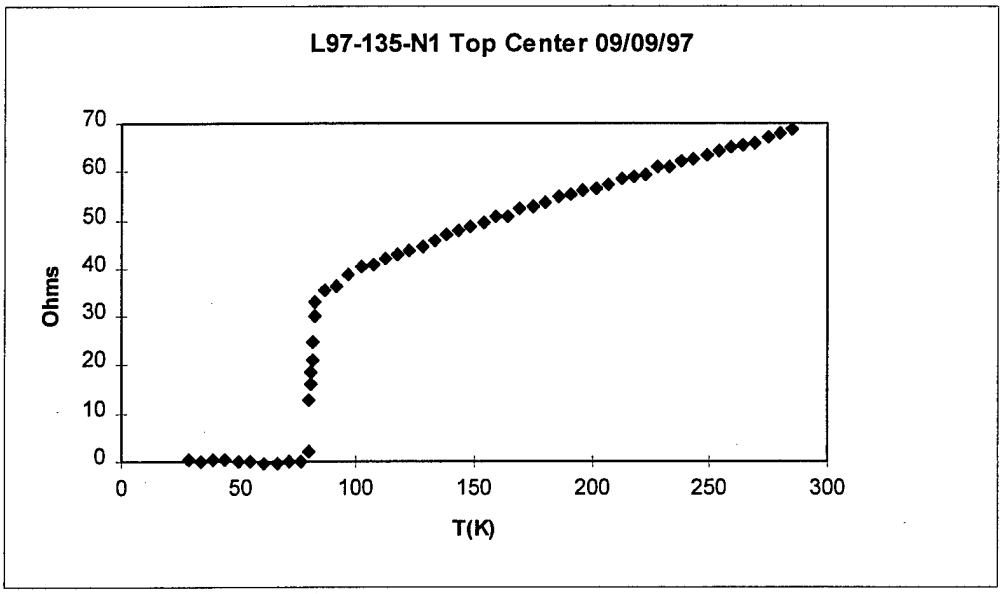

Figure 5.8. Resistance versus temperature of YBCO form top center device on chip L97-135-N1.

After the QSKIP is cooled below the transition temperature, it is stabilized at a selected temperature and the SQUID readout circuit is tested at different detector currents. This test determines the correct SQUID operating conditions for reading out the QSKIP. The operating temperature is selected to ensure that the SQUID critical current is sufficiently small to insure that the $\mathbf{LI}_{SQ}$ product is less than Φ_O. We have selected 13 degrees Kelvin as the SQUID operating temperature and the SQUID's **I-V** curves are

shown in Figure 5.9. The SQUID current is 0.233mA. The SQUID critical current level decreases by increasing the detector bias current from 3mA to 30 mA, and this is shown in Figure 5.10. The readout circuit gain for Figure 5.9, see Equation (2,25), is about 15. Similarly, for the SQUID conditions in Figure 5.10, the readout circuit gain is about 200. The increase readout gain is achieved by increasing the QSKIP bias current from 3mA to 30mA. Also the field generated by the QSKIP bias current reduces the SQUID critical bias current from 0.223mA to 0.151mA and this also contributes to a larger gain.

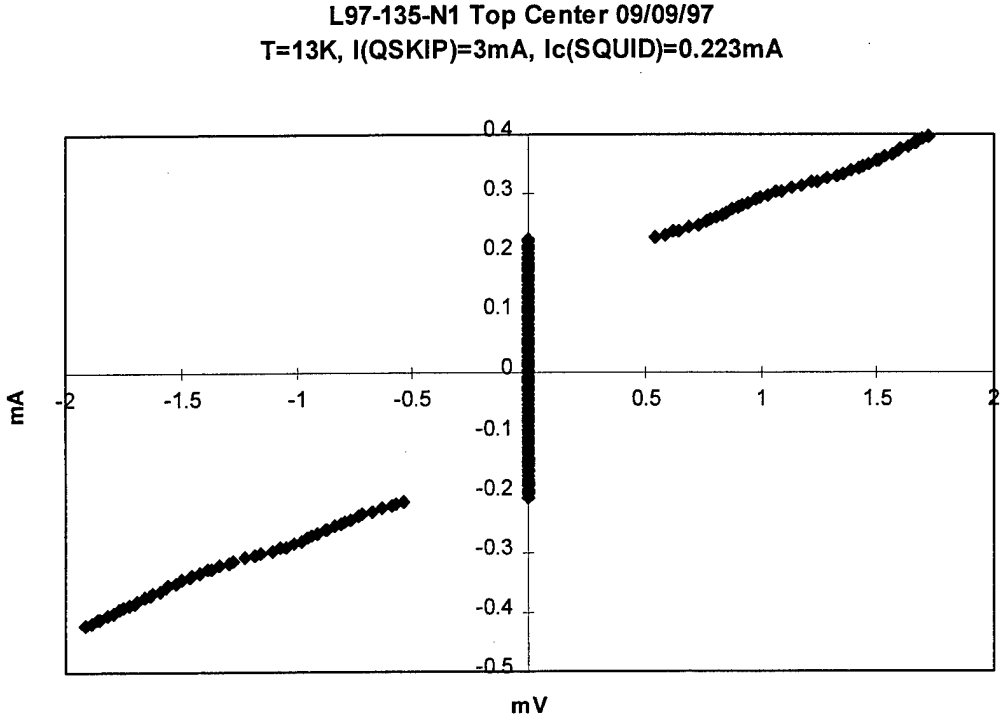

Figure 5.9. SQUID readout for QSKIP device operating at 13K while the detector bias is at 3mA. The SQUID critical current is 0.223mA.

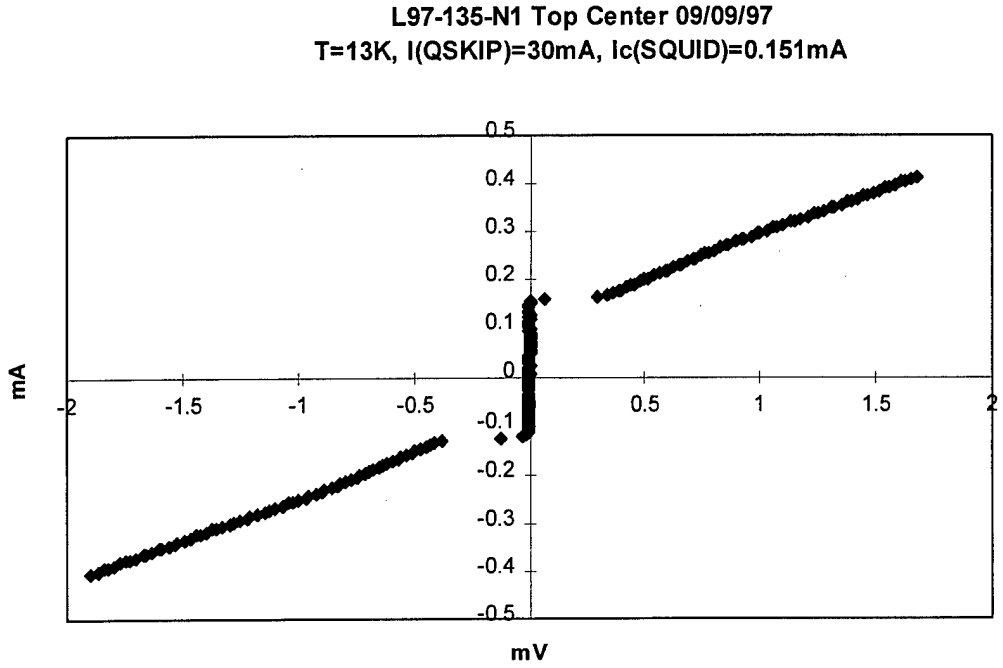

Figure 5.10. SQUID readout for QSKIP device operating at 13K while the detector bias is at 30mA. The SQUID critical current is 0.151mA.

The next step in testing the QSKIP device is to examine the SQUID critical current modulation produced by an imbalance between currents $\mathbf{I_{D1}}$ and $\mathbf{I_{D2}}$, see Figure 2.5. The testing set up has provisions for injecting a dc null current $\mathbf{I_{NULL}}$ (positive or negative) in parallel with $\mathbf{I_{D1}}$, see Figure 3. $\mathbf{I_{NULL}}$ is intended to reintroduce balance into the SQUID circuit corresponding to the conditions established before photoillumination. This condition is also set up to maximize the SQUID's zero voltage $\mathbf{I_{SQ}}$ current capacity. With illumination, the kinetic inductance λ_{LM} on the left side increases thereby causing a larger phase drop across the left side of the SQUID loop. This imbalance is corrected by decreasing the value of $\mathbf{I_{D1}}$ with a negative $\mathbf{I_{NULL}}$ such that the phase drops across the right and left sides of the SQUID are equal; thus again maximizing the zero voltage $\mathbf{I_{SQ}}$ current value. The $\mathbf{I_{NULL}}$ value needed for this maximization corresponds to the imbalance produced by photoillumination. Using this null technique, equilibrium is reestablished and provides a measure of the change in kinetic inductance (see Equation (2,25)) and the quasiparticle lifetimes (see Equations (2,13) and (2,14)).

Before illuminating the QSKIP, the $\mathbf{I_{NULL}}$ current was used to electrically examine the circuit for integrity. This test insures that the SQUID readout continues to operates at the larger current used to bias the detector. Since the SQUID readout and the detector share portions of the YBCO superconducting lines, modulating the SQUID with $\mathbf{I_{NULL}}$, for a given $\mathbf{I_{D1}}$ and $\mathbf{I_{D2}}$, ensures that all elements are operating correctly: all the YBCO lines remain superconducting. Such a test was conducted on a small QSKIP device with 10 squares and 6μm wide YBCO from wafer L97-135-N1, and the result is shown in Figure 5.11.

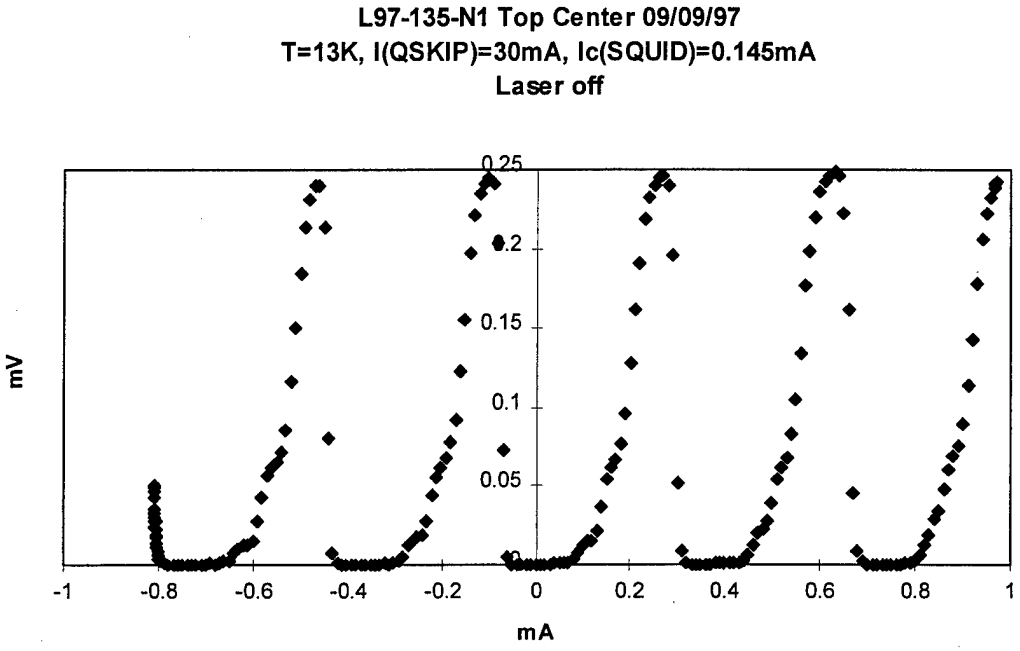

Figure 5.11. The V-Phi curve for a 10 square by 6μm wide YBCO folded geometry QSKIP modulated by I_{NULL}, while $I_{D1}=I_{D2}=15$ma and $I_{SQ}=0.145$mA, see Figure 2.5 for bias circuit view. The periodicity is about 0.35mA.

The periodicity of the SQUID Voltage vs Phi curve with current $\mathbf{I_{NULL}}$ is 0.36mA, where $\mathbf{I_{NULL}}$ is the modulating current injected in parallel with $\mathbf{I_{D1}}$ to ground. From this periodicity, the inferred SQUID inductance is 11pH, which is very near the designed value of 10pH. By exposing the QSKIP to a laser, the SQUID loop inductance should change and this should manifest itself in the periodicity of the Voltage vs Phi curve. In Figure 5.12, the QSKIP is biased as it is in Figure 5.11, while being illuminated by a He-Ne laser with a 53.3 $\mu W/cm^2$ power fluence. Given the data scatter, we could not detect a change in the periodicity of the Voltage vs Phi curves shown in Figure 5.11 and 5.12.

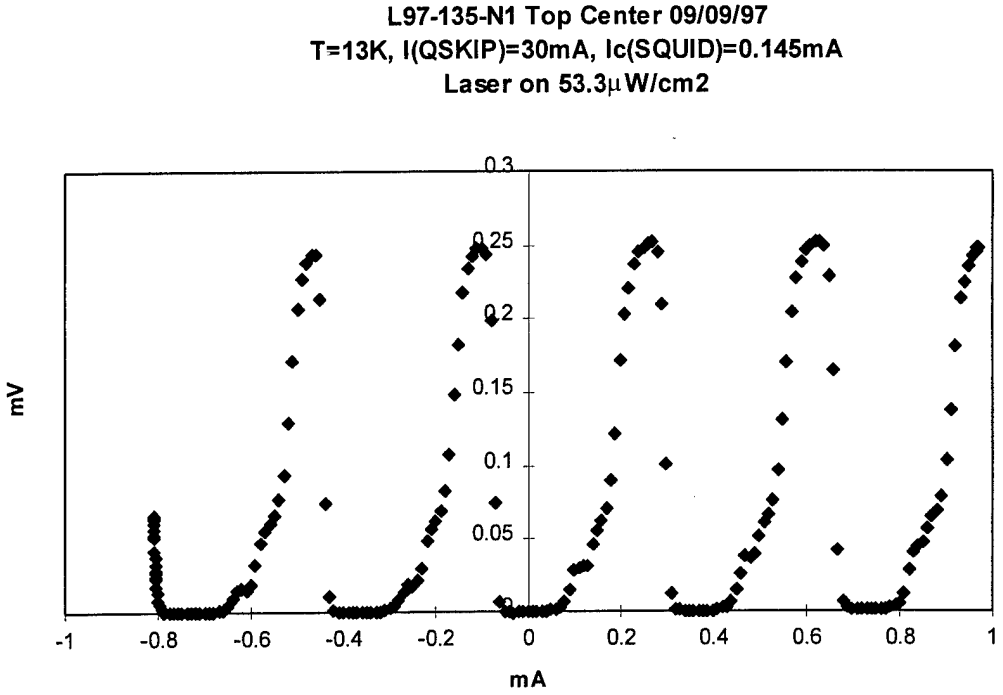

Figure 5.12. A 10 square by 6μm wide YBCO folded geometry QSKIP modulated by I_{NULL}, while $I_{D1}=I_{D2}=15$ma and $I_{SQ}=0.145$mA, see Figure 2.5 for bias circuit view. The periodicity is about 0.35mA.

The sensitivity of the QSKIP can be improved by using a larger detector with more squares and a lock-in amplifier. QSKIP devices with 100 squares are available, however, the SQUID critical current is too high to see modulation by varying $\mathbf{I}_{NULL}$. The 100square QSKIP should have about 100pH inductance and the desired critical current should be about 20μA, corresponding to $\mathbf{I}_{SQ}\ \mathbf{L}_{TOT}\leq\Phi_O$. Instead, the SQUID current $\mathbf{I}_{SQ}$=145μA, a seven fold increase which severely reduces the modulation by varying $\mathbf{I}_{NULL}$. Using a lock-in amplifier for better measurement sensitivity is valid provided the SQUID is not hysteretic. The SQUID hysteresis is determined by the McCumber parameter β_C value: hysteretic for $\beta_C>1$ and non hysteretic for $\beta_C<1$. The value of $\beta_C=(2\pi/\Phi_O)(\mathbf{I}_{SQ}/\mathbf{G})(\mathbf{C}/\mathbf{G})$, where **G** is the SQUID conductance (about 2-3 ohms) and C is the SQUID capacitance. Since we are using a folded loop geometry, the capacitance becomes large, especially for $SrTiO_3$ which has a large dielectric constant $\varepsilon_r\approx1000$. For a 10 square/6μm wide YBCO QSKIP with 100nm of $SrTiO_3$ insulation, the capacitance is

about 32pF. For **C**≈32pF, **G**≈0.5-0.3, $\mathbf{I_{SQ}}$≈145μA, the value computed for β_C is about 58: a hysteretic condition.

The hysteretic condition is due to the large dielectric constant of the $SrTiO_3$ insulation, about 1000. Replacing the $SrTiO_3$ insulation with a material that has a lower dielectric constant, should alleviate this condition. Specifically, Sr_2AlNbO_6 insulator has a lower dielectric, approximately $\varepsilon_r \approx 10$. This should significantly reduce β_C (100 times smaller) to reduce hysteretic behavior. Additionally, lowering the SQUID's critical current also reduced the McCumber parameter β_C value. Ideally, we desire the SQUID's critical current $\mathbf{I_{SQ}}$ to be ≈ 10μA. The detector's sensitivity is maximized with a small critical current. We have fabricated detectors with lower dielectric insulator, and the results are reported next.

Detectors with the lower dielectric insulator Sr_2AlNbO_6 were fabricated. The YBCO film, making up the devices, remained superconducting after all the process steps were completed. The transition temperature at process completion remained high, about 81K. The transition remained sharp and is shown by the Resistance vs Temperature plot shown in Figure 5.13.

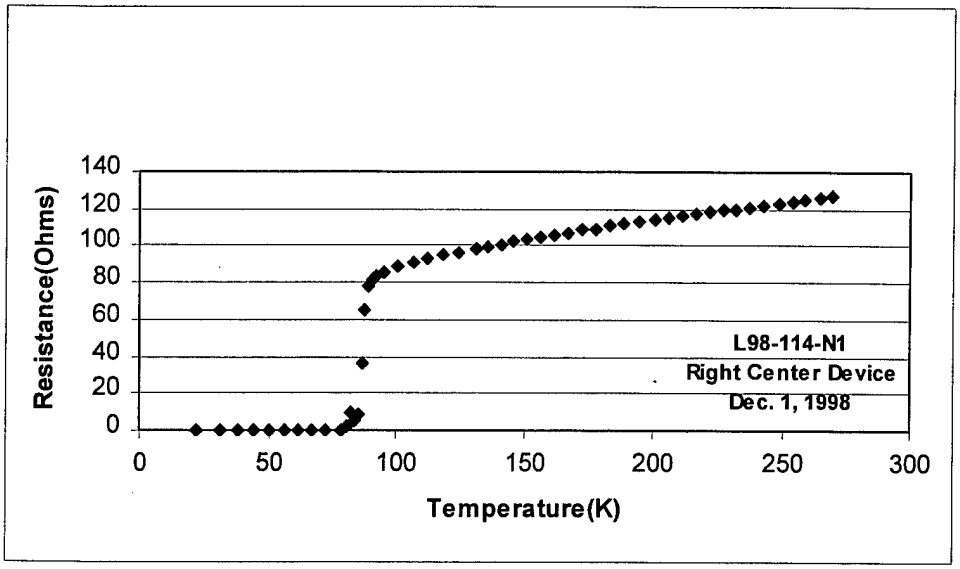

Figure 5.13. YBCO Resistance vs Temperature from lot L98-114-N1. The curve demonstrates that the detector's YBCO film remains superconducting after receiving all the process steps.

The readout SQUIDs for these devices were tested after cool down. The SQUID IV curves remained sharp, revealing good Josephson Junctions. Representative IV curves for the readout SQUIDs are shown in Figures 5.14-5.17. The SQUID's IV curves are sharp without rounding, which would indicate noise in the experimental setup. The SQUID IV curves were measured as a function of detector bias current and these are shown below.

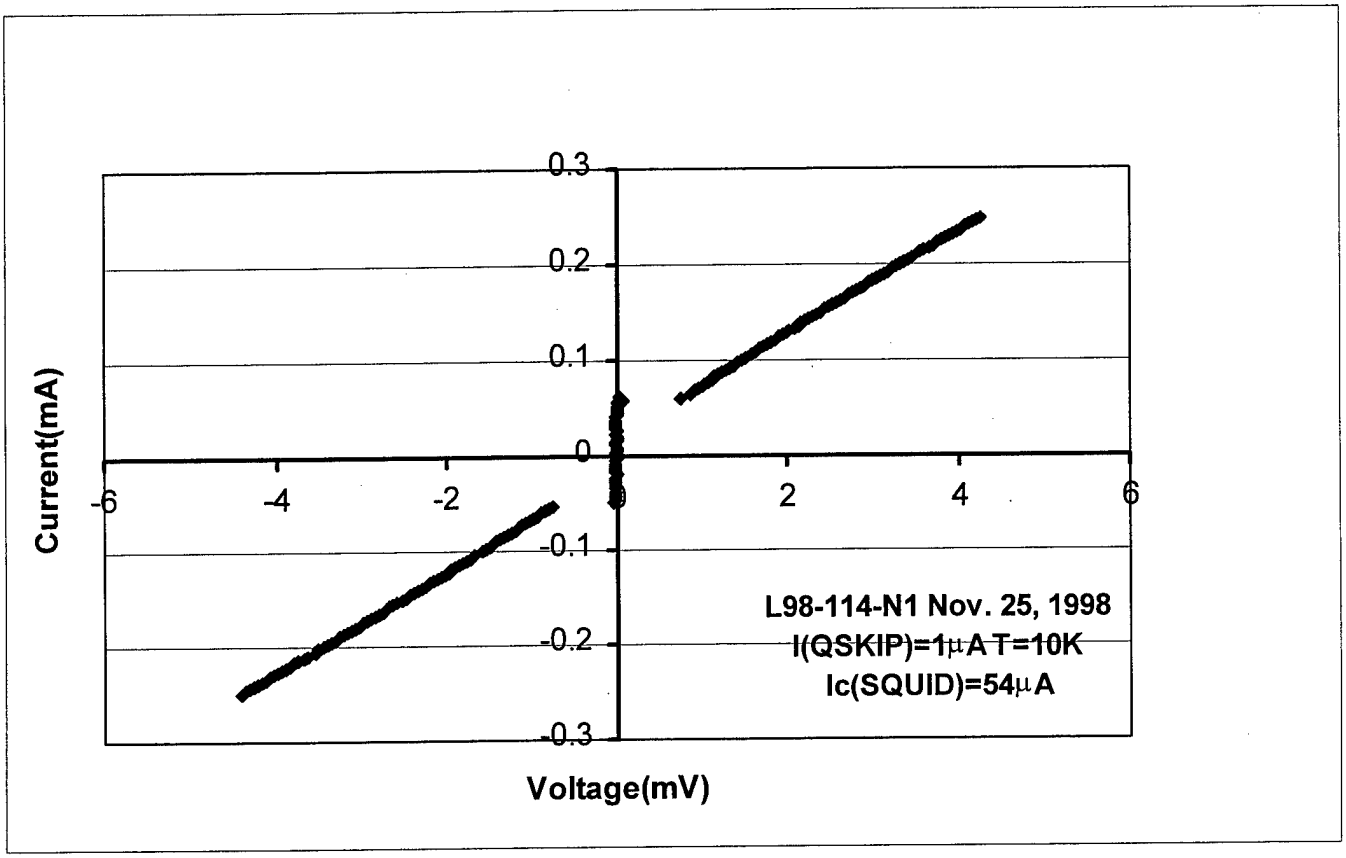

Figure 5.14. SQUID I-V characteristics taken at 10K, with one microampere flowing through the QSKIP, represented by currents I_{D1} and I_{D2} (see Figure 2.5). The SQUID's critical current is 54μA.

As we increase the applied current to the detector, represented by I_{D1} and I_{D2} (see Figure 2.5), the SQUID's IV characteristics change. The SQUID IV curves are not symmetric, and they shift upward. The positive critical current increases from 54μA to

64μA. The small shift is attributed in an asymmetry in the detector bias currents, represented by I_{D1} and I_{D2} (see Figure 2.5). As the detector bias current increase, the asymmetry becomes more apparent.

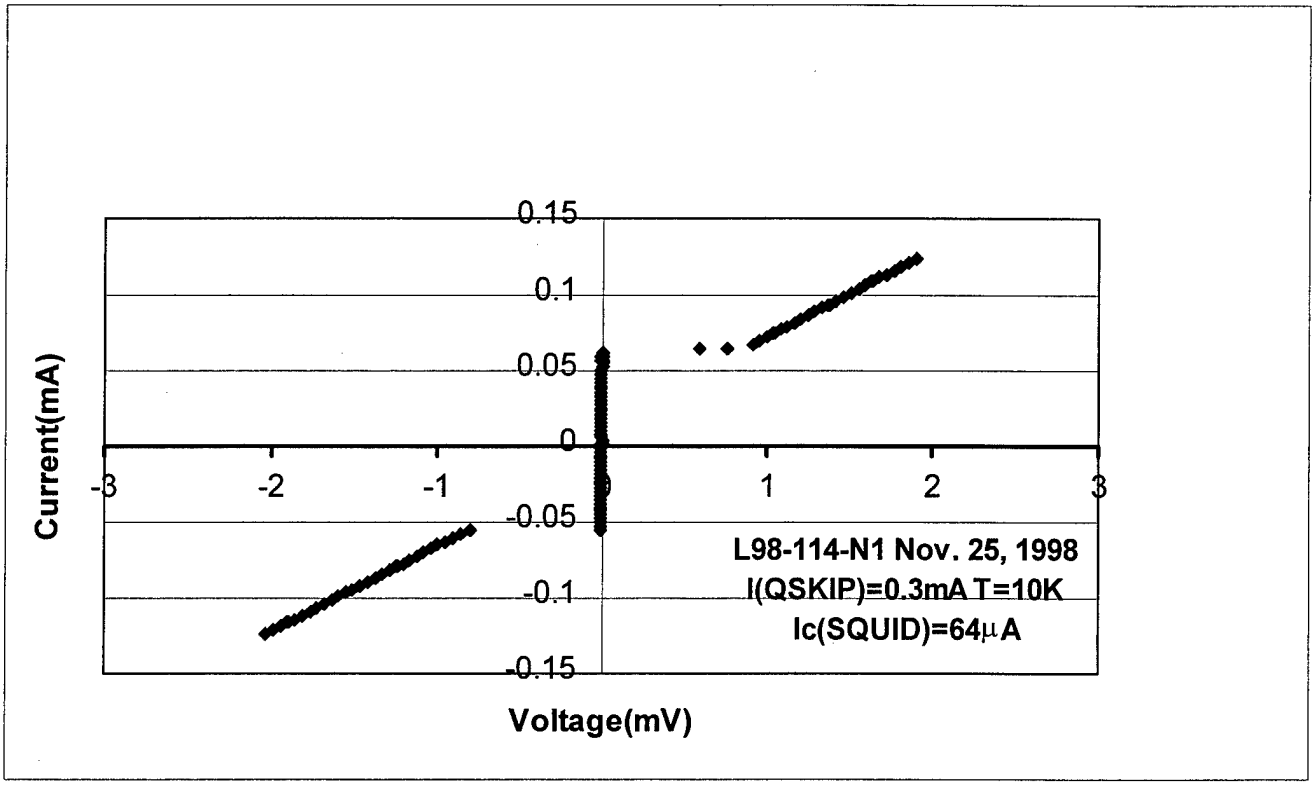

Figure 5.15. SQUID I-V characteristics taken at 10K, with 300 microampere flowing through the QSKIP, represented by currents I_{D1} and I_{D2} (see Figure 2.5). The SQUID's critical current is 64μA.

When the detector current is increased to three miliamperes (see Figure 5.16), the SQUID IV characteristics shift noticeably in the positive direction. The onset of the voltage state remains sharp indicating very little rounding due to noise. The critical current in the positive direction remains at about 54μA and decreases to 40μA in the negative direction. Increasing the QSKIP current further to 30 miliamperes (see Figure 5.17) markedly increases the asymmetry in the SQUID's IV curves. The critical current in the positive direction increases to about 105μA and decreases in the negative direction to almost zero. Resistance of the YBCO lines, carrying the detector currents, remains

superconducting even at thirty miliamperes. This is evident since the SQUID loop remains superconducting as evident from the IV curves. Modulation of the SQUID IV characteristics was also measured and presented next.

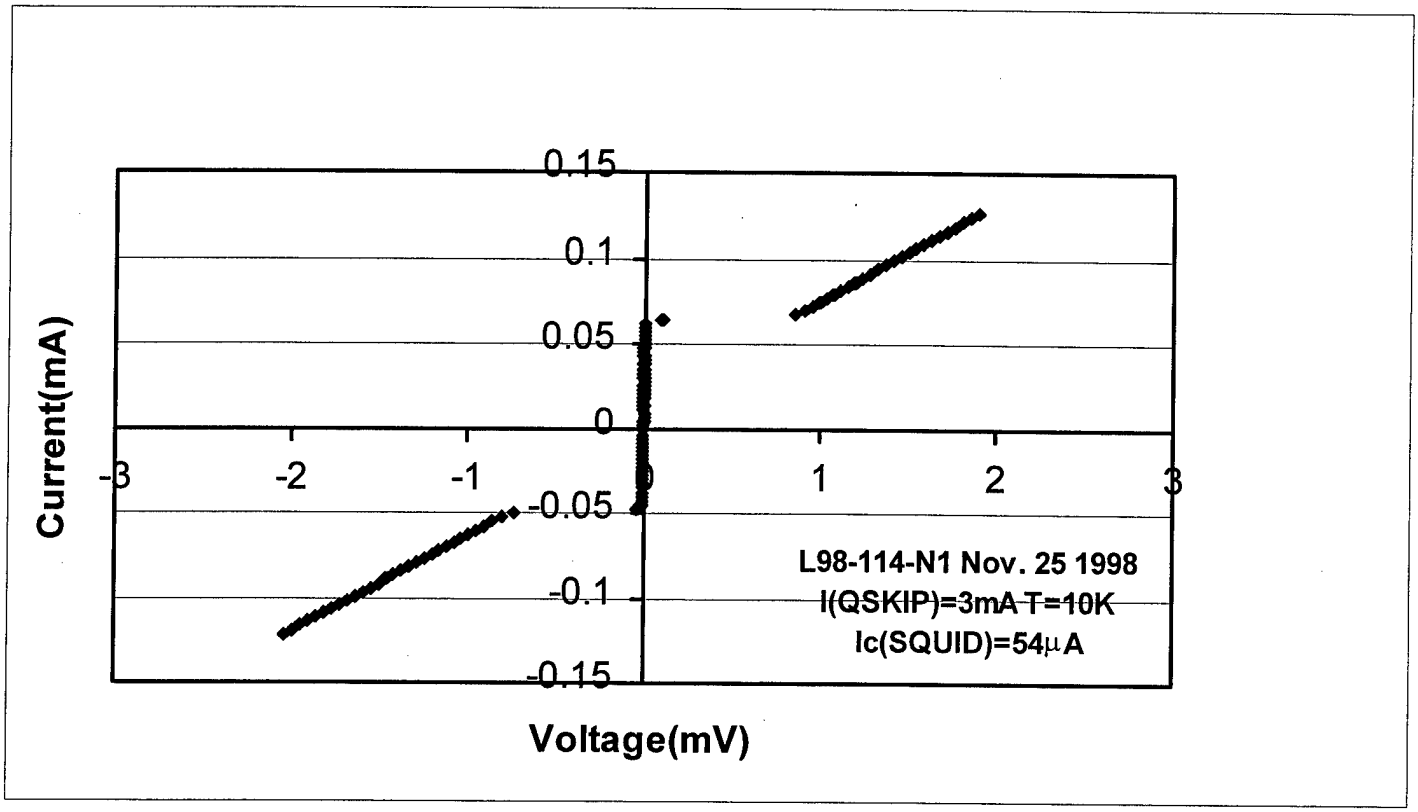

Figure 5.16. SQUID I-V characteristics taken at 10K, with 3 miliamperes flowing through the QSKIP, represented by and I_{D2} (see Figure 2.5). The SQUID's critical current is 54μA for positive currents. The IV curves have taken an asymmetric characteristic.

Modulation of the SQUID's IV curves was examined by varying a small current labeled I_{NULL} (see Figure 3.8). The modulating current I_{NULL} operates in parallel with one of the detector currents (see Figure 2.5). The two currents I_{D1}, and I_{D2} are made equal thereby minimizing the flux to zero, enclosed by the SQUID loop (see Figure 2.5). With minimum flux, the condensate's phase change across each Josephson Junction is the same and about $\pi/2$: thereby resulting in maximum current through the SQUID. Adding a small current to I_{D1}, and not I_{D2}, increases the magnetic flux though the SQUID loop. Since the condensate's phase change around the loop equals to 2π, (see Equaiton 2.23)) the average phase across each Josephson Junctions will change from $\pi/2$ and thereby causing a

modulation of the SQUID's critical current. The critical current modulation will be periodic, since the constraint is that the condensate's phase change around the SQUID's loop be an integer multiple of 2π. This periodic behavior in the SQUID's critical current, with a modulating current I_{NULL} is measured and shown in Figure 5,18.

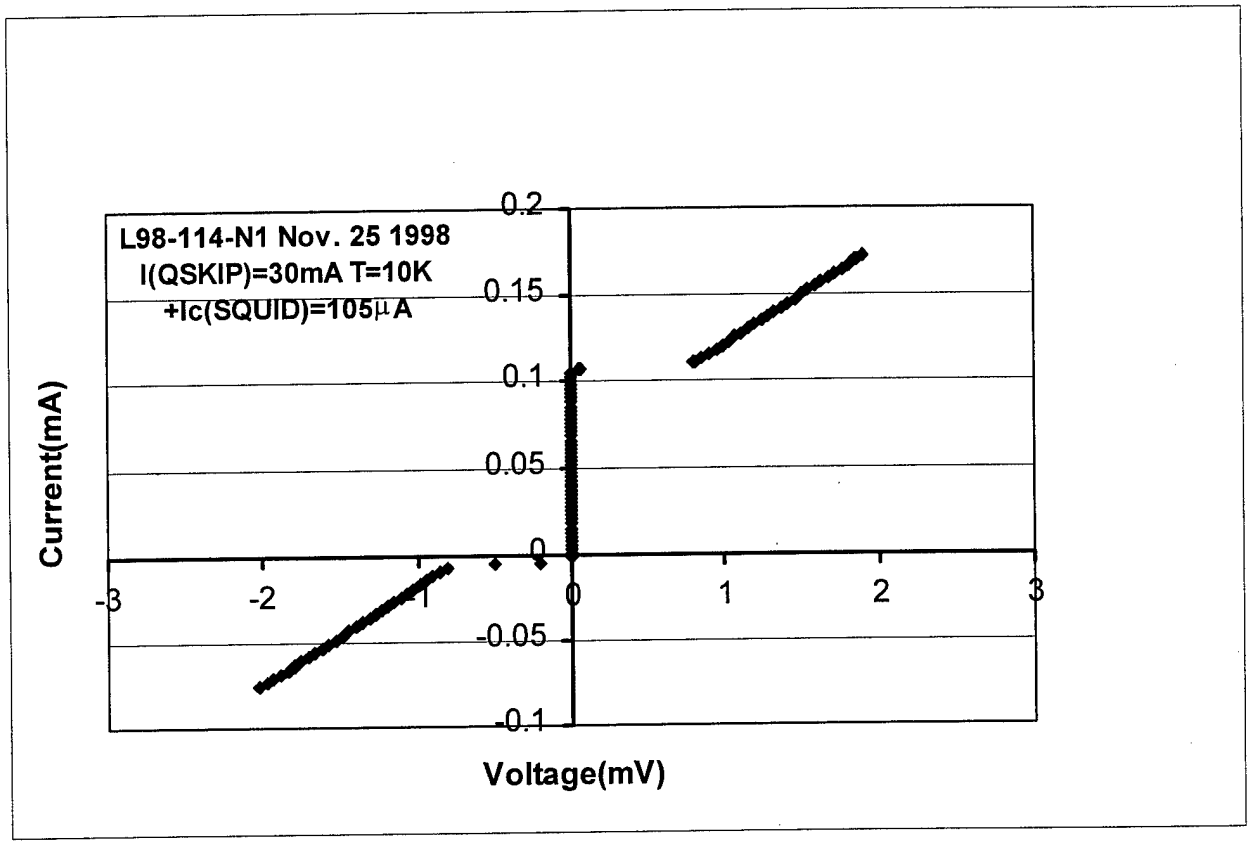

Figure 5.17. SQUID I-V characteristics taken at 10K, with 30 miliampere flowing through the QSKIP, represented by currents I_{D1} and I_{D2} (see Figure 2.5). The SQUID's critical current is 104μA for positive currents. The IV curves have taken an asymmetric characteristic.

In Figure 5.18, by varying I_{NULL} from -0.4 mA to +0.4mA, the SQUID's critical current is periodically modulated. The SQUID's critical current modulation is small and equals to 0.3 mV periodic voltage signal across the SQUID. Six periodic variations are produced by changing I_{NULL} from -0.4 mA to +0.4mA. Accounting for the fact that I_{NULL} only flows through ¼ of the SQUID's loop, the six periods indicate that the SQUID's inductance is about 30pH. The product of the SQUID's loop inductance and critical

current is $L_{SQUID}\ I_{CR} \cong 1.6$ Webers, is about one flux quanta Φ_0. The periodicity of the SQUID loop is dependent on the magnetic inductance and kinetic inductance. The magnetic inductance does not change and the kinetic inductance changes inversely with the number of Cooper pair(see Equation 2.12 and 2.13)). Hence, optical depairing should have an effect on the periodicity, provided the quasiparticle lifetime and the photon flux signals are sufficiently large.

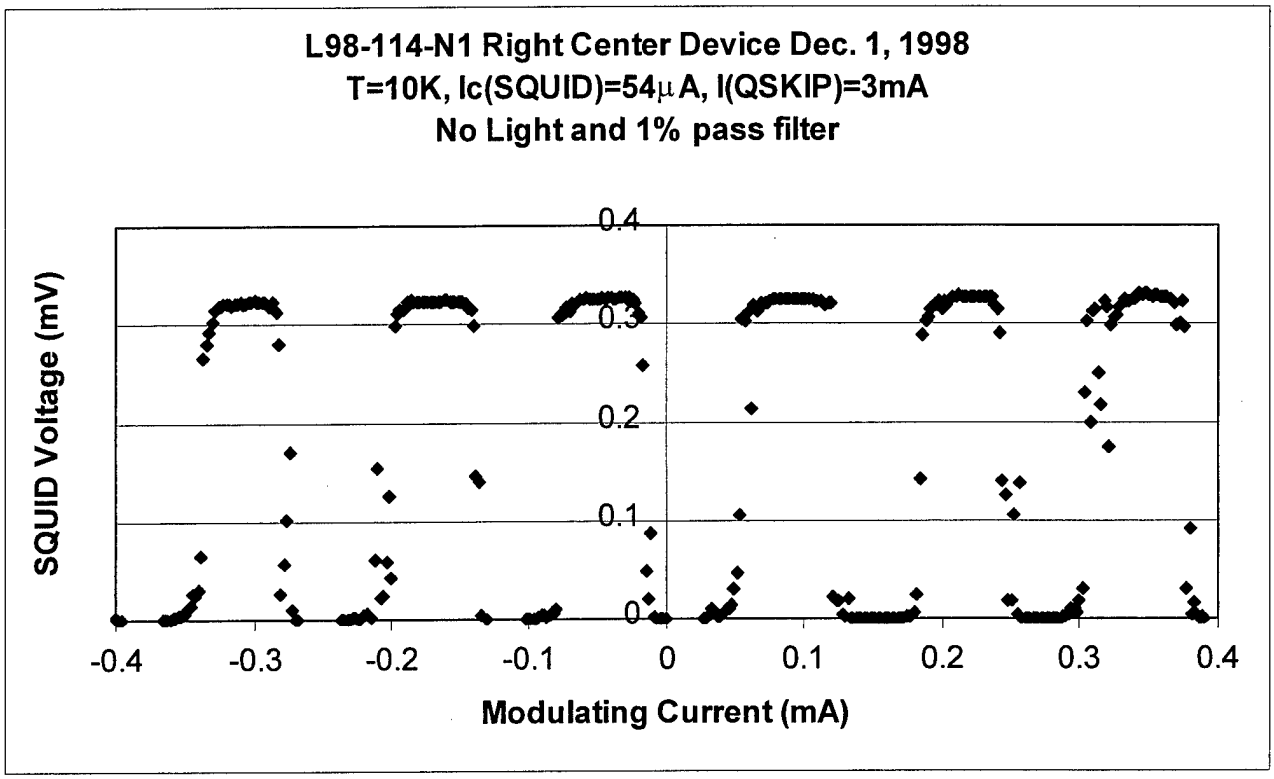

Figure 5.18. Modulation of SQUID critical current with I_{NULL} measured at 10K. The device was not illuminated and a cooled (80K) 1% pass neutral density filter was placed in front of the detector to reduce black body radiation reaching the detector. The SQUID was biased with 54μA and the detector was biased with 1.5MA through each half.

The measurements shown in Figure 5.18 were repeated when the detector was illuminated with a microscope light and the 1% neutral density filter was removed from the beam path. The periodic modulation is shown in Figure 5.19. Changes in the signal amplitude and shape are attributed to small temperature drifts. However, the periodicty of

the modulation has not changed. This indicates the changes in the kinetic inductanceare insufficient to detect from monitoring the SQUID's period of modulation.

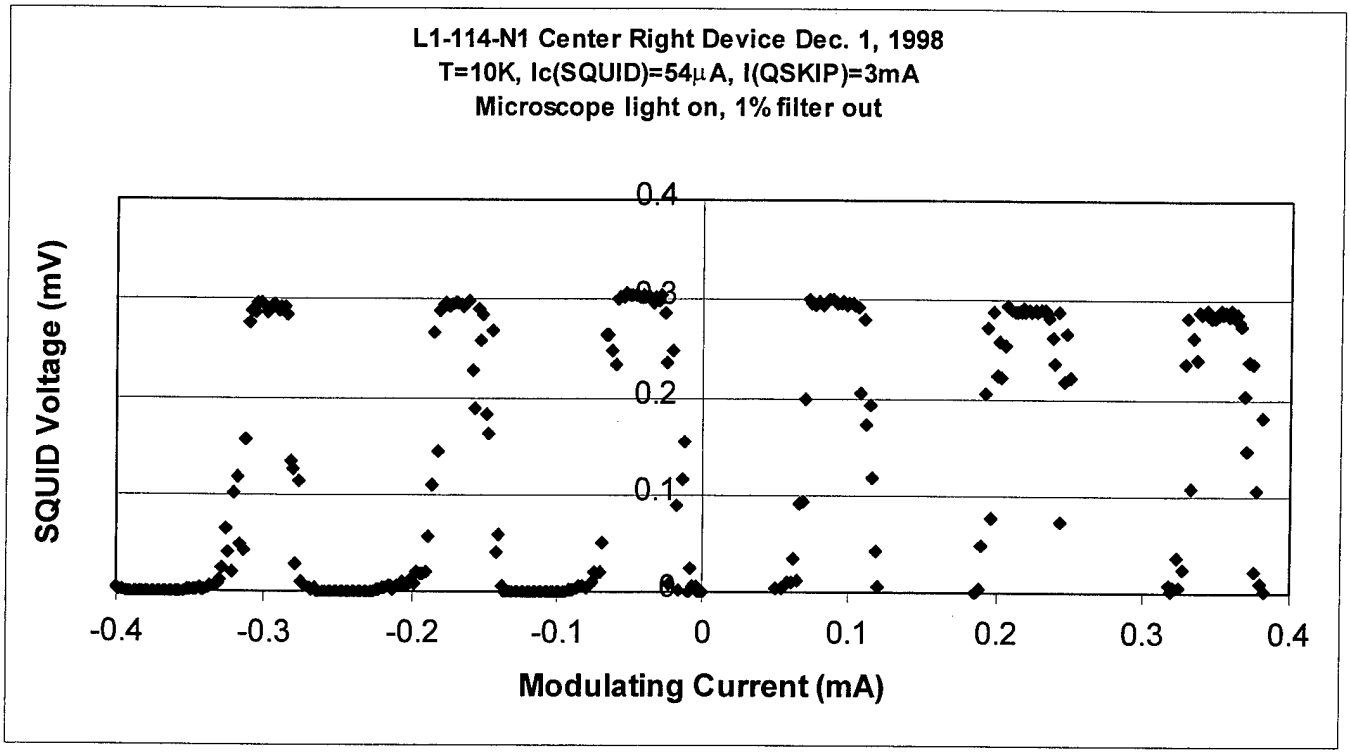

Figure 5.19 Modulation of SQUID critical current with I_{NULL} measured at 10K. The device was illuminated with a microscope lamp and the cooled (80K) 1% pass neutral density filter was removed, allowing much of the microscope light reach the detector. The SQUID was biased with 54μA and the detector was biased with 1.5MA through each half.

In conclusion, the calculation reveal that a BCS based Multispectral QSKIP device should provide excellent performance with an NEP of about 2.5×10^{-15} Watts/√Hz and between a 30-40μm cut-off wavelength. Toward this goal, we have developed performance models and photodetector structures. These should provide the base for future demonstration of superconducting quantum photodetectors. It appears that the quasiparticle excitation lifetime is to short to measure a photoresponse at low frequencies, where these measurements were made. A short quasiparticle lifetime may not be intrinsic to high temperature superconductors, but more a material issue. With better quality high

temperature superconducting films and improved fabrication, perhaps better lifetime can be achieved.

6.0 REFERENCES

1 J.G. Bednorz and K.A. Muller, Z. Phys. B **64**, 189 (1986); Rev. Mod. Phys., **60**, 585 (1988).

2 N. Bluzer, IEEE Trans. Appl. Supercond. **3**, 2869 (1993).

3 J. Bardeen, L.N. Cooper, and J.R. Schriefer, Phys. Rev. **108**, 1175(1957)

4 A.V. Sergeev and M.Yu.Reizer, "Nonequilibrium Superconducting Detectors of Electromagnetic Radiation," submitted to Phys. Rev. B.

5 S.B. Kaplan, C.C. Chi, D.N. Langenberg, J.J. Chang, S. Jafarey, and D. J. Scalapino, Phys. Rev. **B 14**, 4854(1976).

6 J.W. Loram, K.A. Mirza, J.R. Cooper and W.Y. Liang, MOS Satellite Conference to LT-20 July 27-31, 1993. Journal of Superconductivity, Plenum NY.

7 J. A. Levine and S. Y. Hsieh, Phys. Rev. Lett. **20**, 994 (1968).

8 K. E. Gray, A. R. Long and C. J. Adkins, Philos. Mag. **20**, 273 (1969).

9 Michael Nahum, from Harvard, recently inferred the quasiparticle lifetime in aluminum from diffusion lengths measurements made in aluminum NIS tunnel junctions. At temperatures much less than 1K, the measured quasiparticle diffusion lengths are much larger than 300 μm. These very long quasiparticle diffusion length are consistent with quasiparticle lifetimes at least 1μsec long and more likely several orders of magnitude larger (private communications).

10 I. Schuller and K. E. Gray, Phys. Rev. B **14**, 4213 (1976).

11 F. Jaworski, W. H. Parker and S. B. Kaplan, Phys. Rev. B **14**, 4209 (1976).

12 P. Hu, R. C. Dynes and V. Narayanamurti, Phys. Rev. B **10**, 2786 (1974).

13 A. Sai-Halasz, C. C. Chi, A. Denenstein, and D. N. Langenberger, Phys. Rev. Lett. **33**, 215 (1976).

14 W.H. Parker, and W.D. Williams, Phys. Rev. Lett. **29**, 924(1972)

15 A. Rothwarf and B.N. Taylor, Phys. Rev. Lett. **19**, 27 (1967).

16 W.A. Little, Can. J. Phys. **37**,334(1959).

17 A. C. Anderson, in **NON-EQUILIBRIUM SUPERCONDUCTIVITY, PHONONS, AND KAPITZA BOUNDARIES**, edited by Kenneth E. Gray (Plenum, New York, 1980)p. 263.

18 S. B. Kaplan, J. low Temp. Phys. **37**, 343(1979).

19 N. Bluzer, United States Patents 5,179,072 and 5,185,527.

20 H.S. Kwok, J.P. Zheng, and Q.Y. Ying, Appl. Phys. Lett., **54**, 2473(1989)

21 M. Leung, P.R. Broussard, J.H. Claassen, M. Osofsky, S.A. Wolf, and U. Strom, J. Appl. Phys. Lett., **51**, 2046 (1987).

22 W.S. Brockelesby, D. Monroe, A.F.J. Levi, M. Hong, S.H. Liou, J. Kwo, C.E. Rice, P.M. Mankiewich, and R.E. Howard, Appl. Phys. Lett., **54**, 1175 (1989).

23 N. Bluzer and M.G. Forrester, presented at the 1994 Applied Superconductivity Conference, October 16-21, 1994, Boston, Mass., and published in the IEEE Trans. on Applied Superconductivity, **5**(2) , 2583(1995).

24 N. Bluzer and M.G. Forrester, Optical Engineering, **33** No. 3, 697 (1994); N. Bluzer and M.G. Forrester, Journal of Superconductivity, **7**, No. 2, 395 (1994).

25 H. Goldstein, **CLASSICAL MECHANICS** (Addison-Wesley Publishing Co., Inc., Reading, Massachusetts 1950) Chapter 2

26 J.D. Jackson, **CLASSICAL ELECTRODYNAMICS** (John Wiley and Sons, Inc., New York, 1962) Chapter 6, p 181.

27 With the so called London gauge we set $A_{\perp}(X) = -\Lambda J_{\perp}(X)$, where $\perp$ denotes the normal component of the vector potential $\mathbf{A}(X)$ and the current density $\mathbf{J}(X)$ at all boundaries. Thus the canonical momentum $\mathbf{p}=q_{CP}[\Lambda \mathbf{J}_S(X)+\mathbf{A}(X)]$ is equal to zero over the entire boundary and is given in terms of the condensate's phase angle θ as $\mathbf{p}=-i\hbar\nabla\theta=0$. Hence θ is equal to a constant over the entire superconductor. Under these conditions $\Lambda \mathbf{J}_S(X)=-\mathbf{A}(X)$, where $\Lambda=m_{CP}/[\rho_{CP}(X)q_{CP}^2]$.

28 M. Tinkham, **INTRODUCTION TO SUPERCONDUCTIVITY** (Robert E. Krieger Publishing Co., Malabar, FL 1985), Chapter 2.

29 Dale Corson and Paul Lorrain, **INTRODUCTION TO ELECTROMAGNETIC FIELDS AND WAVES** (W.H.Freeman and Co. San Francisco, 1962) Chapter 6, p254.